Study of Dielectric Constant Logging Tools

A Thesis

Presented to

The Faculty of

the Department of Electrical and Computer Engineering

University of Houston

In Partial Fulfillment

of the Requirements for the Degree

Master of Science

in Electrical Engineering

by

Chang-Ming Lin

August 2012

Study of Dielectric Constant Logging Tools

Chang-Ming Lin

Approved:

Chair of the Committee
Richard C. Liu, Professor
Electrical and Computer Engineering

Committee Members:

Donald R. Wilton, Professor
Electrical and Computer Engineering

Heidar A. Malki, Professor and Chair
Engineering Technology

Suresh K. Khator, Associate Dean
Cullen College of Engineering

Dr. Badrinath Roysam, Professor and Chair
Electrical and Computer Engineering

Acknowledgements

This thesis would not have been possible without the support of many people. First of all I would like to express my sincere gratitude to my advisor Dr. C. Richard Liu for his invaluable assistance, support and guidance in the past three years. The experience I acquired in your group and the lessons I learned from you will be invaluable assets in my future. I am also grateful to Dr. Donald R. Wilton and Dr. Heidar A. Malki for being committee members.

I would also like to thank the following individuals for sharing literature and providing invaluable assistance during my study at the University of Houston: Yinan Xing, Jing Wang, Yinxi Zhang, Zhijuan Zhang, Gong Bo, Ziting Liu, Boyuan Yu, Yajuan Kong, Dr. Ning Yuan and Dr. Xiaochun Nie. It was really a pleasure to work with you. Finally I wish to express my love and gratitude to my beloved family for their understanding and endless support, throughout the duration of my studies.

Study of Dielectric Constant Logging Tools

An Abstract of a Thesis

Presented to

The Faculty of

the Department of Electrical and Computer Engineering

University of Houston

In Partial Fulfillment

of the Requirements for the Degree

Master of Science

in Electrical Engineering

by

Chang-Ming Lin

August 2012

Abstract

One of the important issues of well logging is to determine the water saturation from the oil bearing formation. The induction resistivity tool may finish the job if the water is fairly saline. In fresh water, the induction tool is difficult to figure out the exact water saturation and oil/gas contents. Therefore, it is crucial that there be a method to determine water saturation that is less dependent upon the knowledge of water salinity thus making it of great use in fresh water zones. Dielectric constant logging tools offer an attractive new method of formation evaluation, which is relatively independent of water salinity.

In this thesis, a dipole model is developed in that it consists of three infinitesimal dipoles: one for the transmitter and the other two for the receivers. The model, then, is used to simulate the dielectric constant tool responses by measuring the amplitude ratios and phase shifts in both homogeneous and inhomogeneous layered formation. The results show a good agreement with the experimental data and theoretical results published in previous studies. Moreover, the numerical results portray that the dipole model accurately provides a decent estimation of the formation dielectric properties compared to other models.

Table of Contents

List of Figures

List of Tables

Chapter 1 Introduction

Dielectric constant logging tools provide a new electromagnetic propagation logging method to distinguish high resistivity formation fluid from hydrocarbon bearing formation. Traditionally, the measurement of the conductivity or resistivity has remained one of the main surveys performed in a borehole, mainly to determine the water saturation. However, the salinity of formation fluid, which affects the measurement of resistivity logging tools, is usually unknown contained water. The dielectric constant of formation water is relatively high compared with that of hydrocarbons and most minerals. Therefore, by measuring the second electrical characteristic of the formation, the dielectric permittivity, can determine the formation water saturation depending less upon the knowledge of water salinity.

Charter 1 of this thesis gives a brief historical overview of the development of well logging dielectric constant tools by describing the tools as well as the infinitesimal dipole model used in this research. A literature survey including the motivation for this research is given in Charter 2. Chapter 3 derives the field distribution of infinitesimal dipoles by introducing the Hertz potential for electric ($\mathbf{J}$) and magnetic ($\mathbf{M}$) current sources. The solution of inhomogeneous Hertz potential wave equations and simulation models are presented in this chapter. Chapter 4 presents the simulation results of amplitude ratios and phase shifts of a

dielectric constant tool by then drawing up conclusions regarding the usefulness and applicability of the dipole model in Chapter 5.

1.1. Historical Background

Reservoir rocks are mostly sedimentary in nature. They consist of a grain and cement rock matrix with interconnecting void spaces (pores). The pores are filled with formation water, oil, and gas. Resistivity logging is based on the fact that formation rocks can transmit an electric current through the absorbed saline water contained inside their pores, but not through the insulating matrix, oil, and gas. Consequently, water bearing formations tend to have low electric resistivity relative to hydrocarbon bearing formation. However, once the pores reach a high resistance of formation fluid such as fresh water, the resistivity logging tools fail to perform an accurate formation evaluation and provide incorrect formation property measurements.

Dielectric constant logging was developed in the 1970's in order to make a distinction between fresh water and oil, which was difficult to do with resistivity logs alone. Dielectric constant logging tools measure the dielectric permittivity of formation contained water to determine the formation water saturations without knowledge of the water salinity. The basic measurements are the phase shift and attenuation of electromagnetic fields which have been propagated in the formation. Two classes of tools are available for measuring the formation

dielectric constant. The first one is low-frequency dielectric constant logging tools used coils on a mandrel and operate at tens of megahertz. The second type is high-frequency dielectric constant logging tools used for a microwave antenna on a pad contact device.

The interesting factors of using downhole logging techniques in order to determine the dielectric constant of earth formation have been growing. This is because the dielectric constant of water is an order of magnitude higher than the dielectric constant of the petroleum or the formation rock, and therefore, the dielectric constant measurements are fairly sensitive to the formation water content. In Table 1.1 we list some examples of the relative dielectric constants of a number of substances commonly found in earth formations. The laboratory experiments [1] have shown that the relative dielectric constant ε' of formation rock is nearly independent of water salinity in microwave frequencies. This latter fact is of particular importance because of the increased focus on secondary and tertiary recovery projects in the petroleum industry. The water salinity of those recovery projects, which have been unavailable in the past due to limited logging techniques, is often unknown as a result of fresh water, CO_2, or chemical flooding. As a result, dielectric constant logging at microwave frequencies offer this capability as well as having the further potential of providing a quantitatively accurate value for the formation oil saturation.

Table 1.1 Dielectric constants of commonly found in earth formations.

Substance	Relative dielectric constant
Limestone[a]	5.55
Berea sandstone[a]	3.45
Yule marble[a]	8.06
Dolomite[a]	7.92
Pine prairie salt[a]	5.51
Water[b]	76.7
Petroleum oils[b]	1.92 – 2.22

(a) Values reported by Tam [2] at frequency = 1.0 GHz for dry rocks at room temperatures.

(b) Values reported by von Hipple [3] at frequency = 3.0 GHz and T = 25℃.

The dielectric permittivity is one of the major factors that influence electromagnetic wave propagation in a material. The properties of dielectric permittivity in the earth's formation are strongly dependent on the formation water saturations and are relatively independent of the water salinities. Microwave frequency dielectric logging, thus, offers an exceptional efficiency electromagnetic logging method of formation evaluation. The new EM wave dielectric constant logging method deduces the properties of dielectric constants from attenuation and phase shift measurements of electromagnetic fields that propagated in the formation. Calvert [4], Rau [5-7], Clark [8], Freedman [9], and Schlumberger scientists, have proposed several U.S. patents that utilize this method in well logging devices.

Table 1.2 is a list of dielectric constants and propagation times for various materials [10]. Apparently, fresh water has a greater electromagnetic wave travel time and dielectric constant than any other materials found on the list. Therefore,

by measuring the dielectric constant of earth formation, one can determine the water saturation versus hydrocarbon-bearing zones. Unlike the resistivity logs, the dielectric measurement is independent of water distribution and salinity (and dependent on the operation frequency).

Table 1.2 Propagation Times for Various Materials [10]

Material	Dielectric Constant, ε (Farads/m)	Matrix Propagation Time (ns/m)	Fluid Propagation Time, (ns/m)
Sandstone	4.65	7.2	
Limestone	7.50	9.1	
Dolomite	6.80	8.7	
Anhydrite	6.35	8.4	
Halite	5.6 to 6.35	7.9 to 8.4	
Shale	5 to 25	7.5 to 16.6	
Oil	2.2		4.9
Gas	3.3		6.0
Fresh water (at 25℃)	78.3		29.5

ns/m = nanoseconds/meter.

1.2. Dielectric Constant Logging Tools

Table 1.3 lists various dielectric logs run by different service companies [10]. Halliburton (older Gearhart DCL and Welex DT) and Baker Atlas DL (mandrel and pad) tools are considered to be low-frequency dielectric constant logging tools, operating at 20 to 200 MHz. The Halliburton HFDT (Figure 1.1) and Schlumberger (EPT and Dielectric Scanner) (Figure 1.2 and 1.3) are considered high-frequency dielectric constant logging tools, and operate at 1 and 1.1 GHz. The logs measure

the propagation time of the electromagnetic wave by deducing from the phase shift and attenuation measurement of electromagnetic fields passed through the formation.

Table 1.3 List of dielectric logs from different service companies [10]

Company	Tool Name	Frequency	Investigation Depth
Halliburton	HFDT (pad)	1.0 GHz	Flushed zone
Gearhart (now Halliburton)	CL (mandrel)	30 MHz	Invaded zone
Welex (now Halliburton)	DT (mandrel)	20 MHz	Invaded zone
Atlas Wireline (Baker Atlas)	DL (mandrel) DL (pad)	47 MHz ~ 200 MHz	Invaded zone, Flushed zone
Schlumberger	EPT (pad)	1.1 GHz	Flushed zone
Schlumberger	Dielectric scanner	20 MHz ~ 1 GHz	Invaded zone, Flushed zone

MHz = megahertz (million cycles/sec)
GHz = gigahertz (billion cycles/sec)

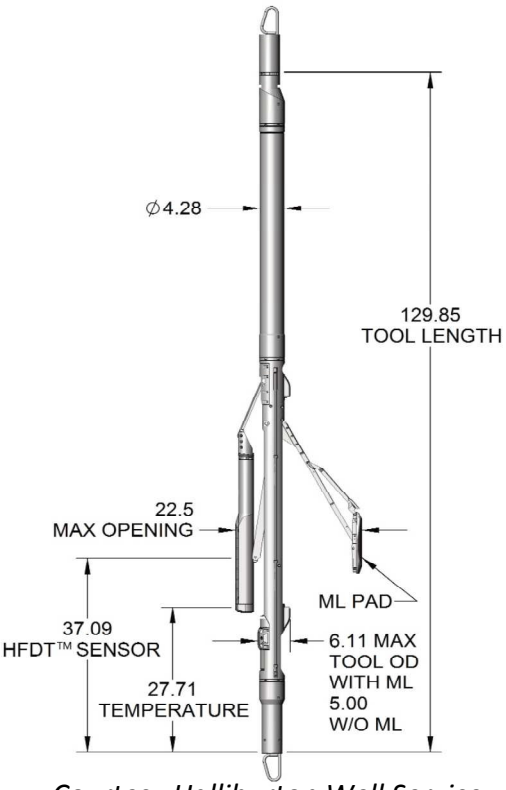

Courtesy Halliburton Well Service

Figure 1. 1 The High Frequency Dielectric Tool (HFDT)

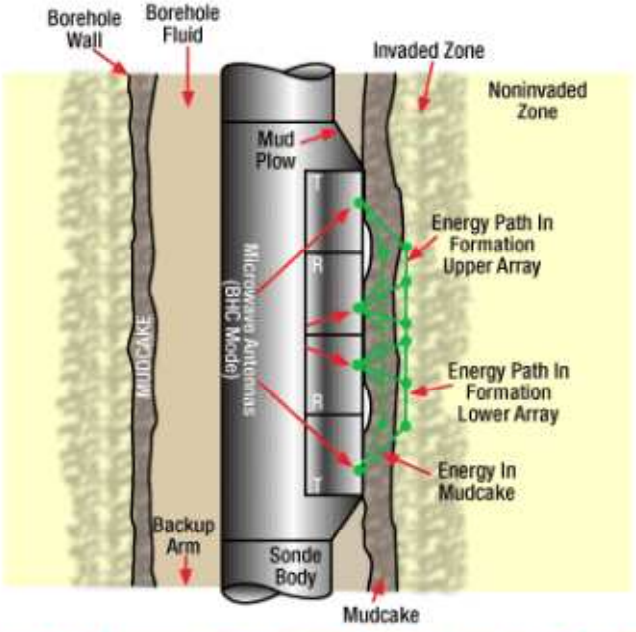

Reprinted by Permission of the SPWLA from Johnson and Evans 1983.

Figure 1. 2 A downhole schematic of the EPT Tool

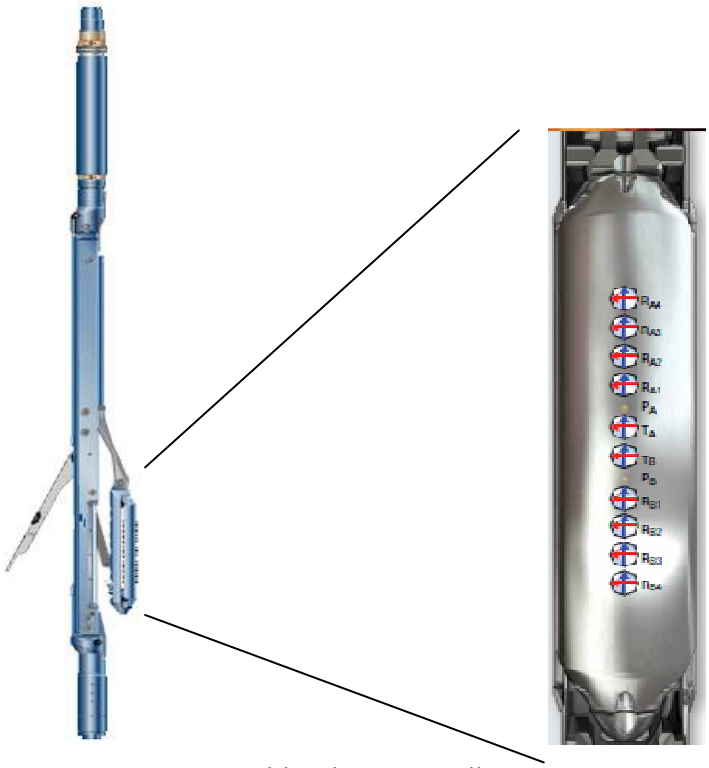

Courtesy Schlumberger Well Service

Figure 1. 3 The Dielectric Scanner

In Figure 1.1 the High Frequency Dielectric Tool (HFDT) is a pad type of dielectric constant tool made by Halliburton that is operated at a microwave frequency of 1 GHz. It consists of two symmetric transmitters and three receivers to compensate the borehole effects. The design of the sensor helps to minimize the effects of rugosity, borehole, and the change in readings due to pad contact. Figure 1.2 shows the Electromagnetic Propagation Tool (EPT) that consists of two transmitting and receiving cavity-backed slot antennas. The EPT measures the speed of propagation and the rate of attenuation of a 1.1 GHz electromagnetic wave to determine the dielectric constant as well as the conductivity of the invaded zone of the formation. Figure 1.3 is the Dielectric Scanner that consists of

two transmitting antennas and eight receiving antennas symmetrically surrounding the transmitting antennas. This tool measures the formation dielectric at 1-4 inch depth of investigation with 4 different frequencies, 20 MHz, 100 MHz, 500 MHz, and 1 GHz. Each antenna is a cross-dipole offering collocated normal magnetic dipoles working in longitudinal and transversal mode. In this thesis, we will perform in detail, an investigation of the Electromagnetic Propagation Tool (EPT) and a preliminary study of the Dielectric Scanner.

1.3. EM Wave Propagation Model of the Dielectric Logging Tool

Various methods for measuring dielectric permittivity in the laboratory [11] can be categorized as reflection, transmission, and resonance techniques. The resonance techniques do not give in to the measurement in a borehole. Of the former two, the transmission method is superior for the measurement of dielectrics with high conductivity losses. Figure 1.4 represents schematically the transmission of an electromagnetic wave at the interface between a medium with lower permittivity and the losses formation. According to the law of refraction (known as Shell's law), the transmitted wave is refracted away from the normal in the lower permittivity formation. If the incident wave is at the critical angle, the reflected wave will travel along the interface. Therefore, we can see that the velocity of propagation along the surface will be determined by the permittivity of the formation. The surface wave continuously sheds energy into the mud layer.

Then, by placing two receivers in the mud column, a differential measurement of the phase shift and attenuation can be made.

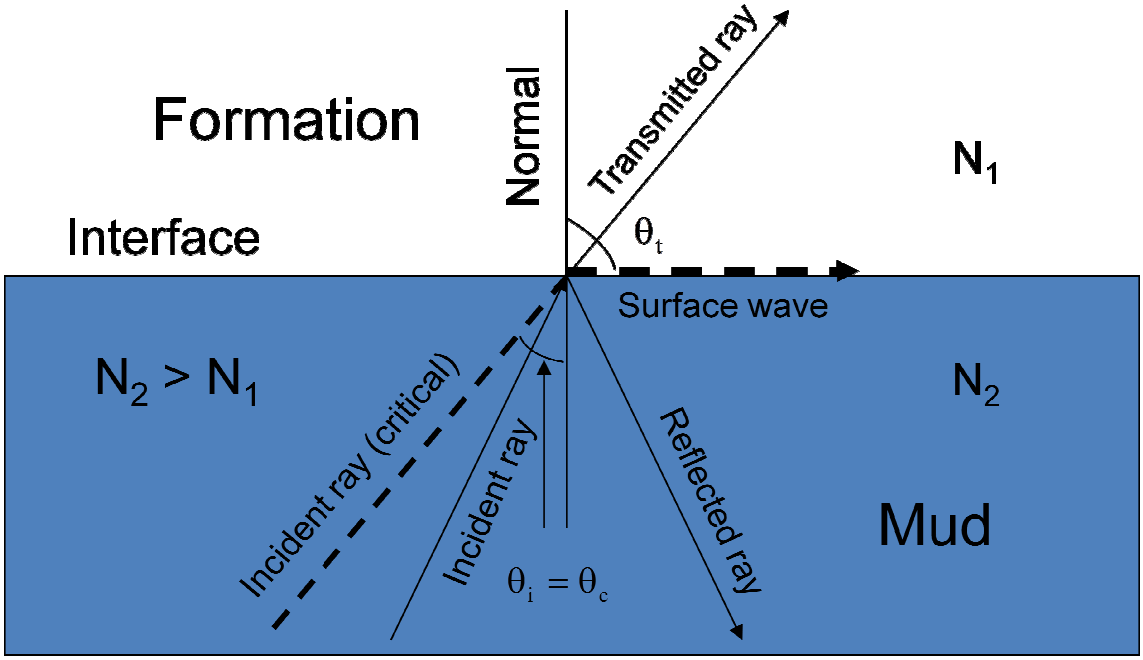

Figure 1. 4 A diagram of EM wave refraction at a mud-borehole interface

Chapter 2 Literature Overview

Formation evaluation is a critical component in maximizing oil well production. Therefore, a considerable amount of research has been devoted to modeling the response of dielectric constant logging tools by using an electromagnetic propagation method at a microwave frequency. At lower frequencies, electrical conduction is dominated by ionic concentration in pore fluid and is thus related to clay particles, as well as the water saturation. The dielectric properties of the measured medium are a complex function and are related to the relative permittivity plus the imaginary portion of the conductivity of the medium.

$$\varepsilon^* = \varepsilon_r + i\frac{\sigma}{\omega\varepsilon_0}. \tag{1}$$

As frequency increases, dielectric effects start to appear as they then become predominant as seen from equation (1). This increase in sensitivity allows the evaluation of conductivity and permittivity simultaneously. The propagation constant characteristic shown in equation (2) of a dielectric medium clearly illustrates the change in sensitivity with frequency. Once the frequency of operation is high, the depth of investigation of such measurement is relatively shallow.

$$k = \frac{\omega}{c}\sqrt{\mu_r}\sqrt{\varepsilon_r + i\frac{\sigma}{\omega\varepsilon_0}}. \tag{2}$$

Various approaches have been developed for modeling and investigating the dielectric constant logging tools, Chew [12] has thoroughly investigated the electromagnetic wave propagation tool (EPT) theoretically in 1981. He used an asymptotic analysis to derive close approximations of the EM wave received in receivers and decomposed the wave into a guided wave and a lateral wave, which propagate with a wave number close to the wave number of the invaded zone. The travel times are also computed, using both asymptotic approximations and a plane-wave assumption. Chew [13-14] also proposed both a theory and applications and results of a theoretical model for high-frequency dielectric logging tools in 1988. The model consists of the measurement tool in front of a two-dimensional inhomogeneity, which has been divided into two regions. The solution in each region is treated analytically in two dimensions, and numerically in one dimension that is solved using the finite element method. The results of the theoretical model were used to study the behavior of such tools across geological sedimentary beds. The standoff and mud cake effects that reflect on the depth of investigation of such a tool have been evaluated in two different polarizations TE and TM modes.

Long [15] presented an experimental study of the impedance of cavity-backed slot antennas, which were utilized in the EPT tool. The impedance of cavity-backed slot antennas were found both as a function of frequency and of the

various parameters of the cavity, namely, the cross-sectional size of the cavity, the medium filling the cavity, and the type of termination of the cavity. Also a mathematical model has been derived by Long [16] that relates the impedance of a cavity-backed slot antenna to that of an identical slot which is free to radiate on both sides of a large ground plane.

The latest dielectric constant logging tools overcome the limitation of previous dielectric tools such as borehole rugosity, high salinity, and a simple response algorithm. The new tool measures formation dielectric at 1-4 inches depth of investigation with 4 frequencies, 2 polarizations, 4 transmitter receiver spacing's, and 2 shallow probes to determine the mud cake and mud properties [17]. The different frequencies provide a measurement of dielectric dispersion to quantify textural information, which has significantly affected the tools responses when measured at low frequency. By designing a multi-transmitter-receiver spacing that is symmetrically arranged, the capability of interpreting the dielectric dispersion in a formation matrix was finally available.

Chapter 3 Field Distribution and Modeling

In the past, the stationary charge with respect to an observer measuring the properties of the charge is considered to be an electric field, as the charge then moves with respect to the observer having then been considered a magnetic field. With time, people began to realize that the electric and magnetic fields were better thought of as two parts of a greater whole – the electromagnetic field, which affected the behavior of the charged objects in the vicinity of the field. Moreover, the Maxwell's equation and the Lorentz force law described the way that charges and currents interact with the electromagnetic field.

In the analysis of radiation problems, the common procedure is to specify the sources and then to require the fields radiated by the sources. In contrast to the synthesis problem, the radiated fields are specified, as we are then enabled to determine the sources. It is very common in the analysis procedure to introduce auxiliary functions, known as *Hertz potentials*, which will aid in solving the problem. The introduction of the potentials often simplifies the solution even though it may require determination of additional functions. Although it is possible to determine the $\mathbf{E}$ and $\mathbf{H}$ fields directly from the source-current densities $\mathbf{J}$ and $\mathbf{M}$, it is usually easier to find the auxiliary potential functions first and then determine the $\mathbf{E}$ and $\mathbf{H}$. This two-step procedure is shown in Figure 3.1 [18].

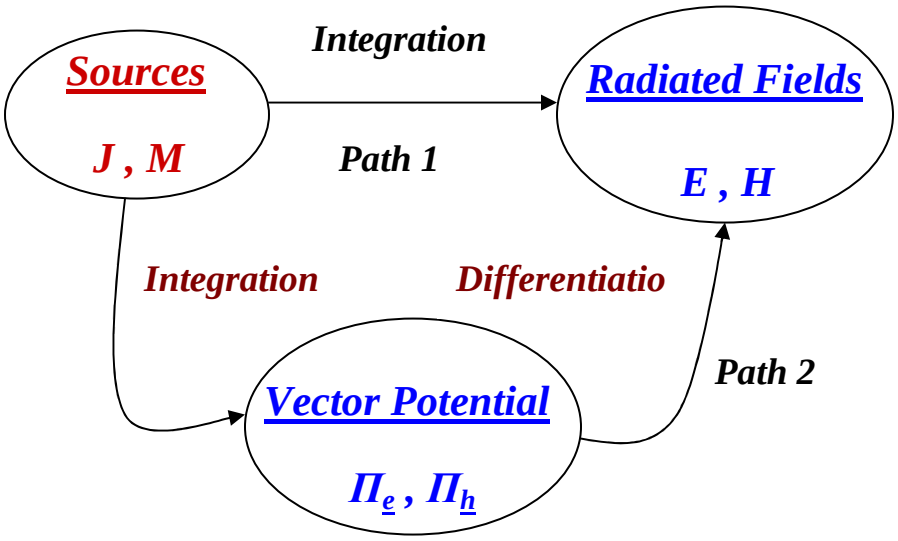

Figure 3. 1 Block diagram for the two-step procedure

The one-step procedure, through path 1, relates the **E** and **H** fields to **J** and **M** by integral relations. The two-step procedure, through path 2, relates the $\mathbf{\Pi}_e$ and $\mathbf{\Pi}_h$ potentials to **J** and **M** by integral relations. The **E** and **H** are then determined simply by differentiating $\mathbf{\Pi}_e$ and $\mathbf{\Pi}_h$. Although the two-step procedure requires both integration and differentiation, where path 1 requires only integration, the integrands in the two-step procedure are much simpler. The most difficult operation in the two-step procedure is the integration to determine $\mathbf{\Pi}_e$ and $\mathbf{\Pi}_h$. Once the Hertz potentials are known, the **E** and **H** can always be determined through any well-behaved function, no matter how complex.

3.1. Infinitesimal Dipole Radiation and Model

3.1.1. Infinitesimal Dipole

The simplest radiating element is the infinitesimal dipole that can easily be implemented in any electromagnetic code. An infinitesimal linear wire ($l << \lambda$) is positioned symmetrically at the origin of the coordinate system and oriented along the z axis, as shown in Figure 3.2. We can model it as a solid rectangle and compute its current density **J** shown in Figure 3.3.

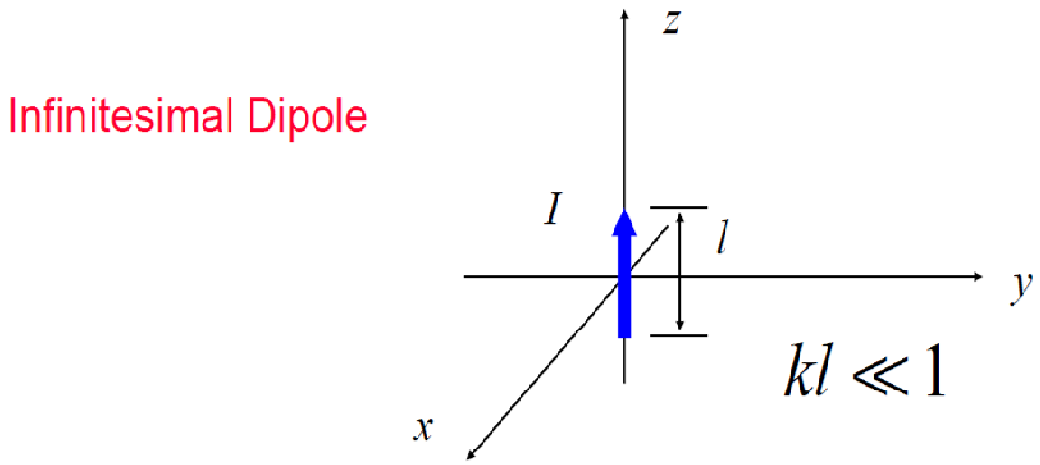

Figure 3. 2 An infinitesimal dipole in origin

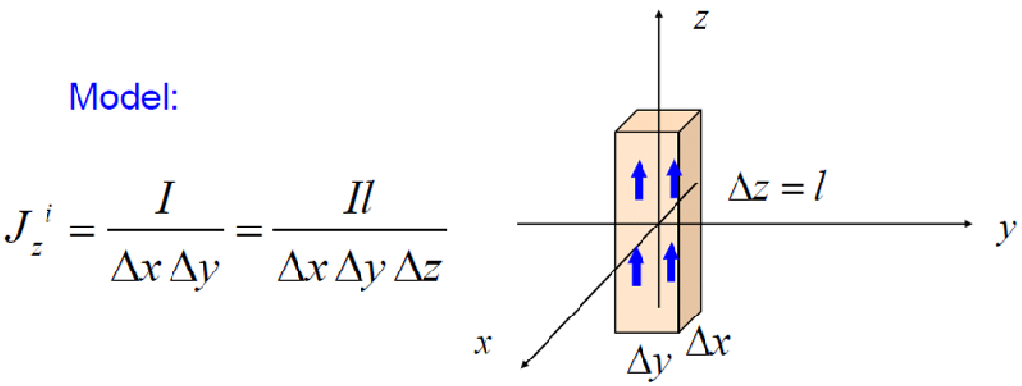

Figure 3. 3 A solid rectangular model of infinitesimal dipole

For current density **J** in z direction can be seen as

$$\mathrm{J}_z^i = \frac{\mathrm{I}}{\Delta\,\mathrm{x}\,\Delta\,\mathrm{y}} = \frac{\mathrm{Il}}{\Delta\,\mathrm{x}\,\Delta\,\mathrm{y}\Delta\,\mathrm{z}}\,. \tag{3}$$

Define

$$P(x) = \begin{cases} \dfrac{1}{\Delta x} & x \in \left(-\dfrac{\Delta x}{2}, +\dfrac{\Delta x}{2}\right) \\ 0 & \text{otherwise} \end{cases}, \tag{4}$$

$$P(y) = \begin{cases} \dfrac{1}{\Delta y} & y \in \left(-\dfrac{\Delta y}{2}, +\dfrac{\Delta y}{2}\right) \\ 0 & \text{otherwise} \end{cases}, \tag{5}$$

$$P(z) = \begin{cases} \dfrac{1}{\Delta z} & z \in \left(-\dfrac{\Delta z}{2}, +\dfrac{\Delta z}{2}\right) \\ 0 & \text{otherwise} \end{cases}. \tag{6}$$

Substitute equation (4), (5), and (6) into current densities (3), we obtained

$$J_{\mathrm{z}}^{\mathrm{i}} = (Il)\,P(x)P(y)P(z)\,. \tag{7}$$

Intuitively, to be an infinitesimal size, as $\Delta x \to 0$, $P(x) \to \delta(x)$, therefore, letting $\Delta x, \Delta y, \Delta z \to 0$, the equation (3) can be rewritten as

$$J_{\mathrm{z}}^{\mathrm{i}} = (Il)\,\delta(x)\delta(y)\delta(z), \tag{8}$$

or

$$J_{\mathrm{z}}^{\mathrm{i}} = (Il)\,\delta(r)\,. \tag{9}$$

Equation (9) can be viewed as infinitesimal dipole current densities in z direction.

3.1.2. Hertz Potential $\mathbf{\Pi}_e$ for an Electric Current Source $\mathbf{J}$

As mentioned before, the two-step procedure provides a simple path in solving the electromagnetic field from the current density source. So the Hertz potential $\mathbf{\Pi}_e$ is useful in solving for the EM field generated by a given harmonic electric current $\mathbf{J}$. The magnetic flux $\mathbf{B}$ is always solenoidal; that is $\nabla \cdot \mathbf{B} = 0$. Therefore, it can be represented as the curl of another vector because it obeys the vector identity $\nabla \cdot \nabla \times \mathbf{\Pi}_e = 0$, where $\mathbf{\Pi}_e$ is an arbitrary vector. Thus we define

$$\mathbf{B}_e = \nabla \times \mathbf{\Pi}_e \Rightarrow \mathbf{H}_e = \frac{1}{\mu} \nabla \times \mathbf{\Pi}_e, \tag{10}$$

where subscript *e* indicates the field due to the $\mathbf{\Pi}_e$ potential. Then, substituting (10) into Maxwell's curl equation

$$\nabla \times \mathbf{E}_e = -j\omega u \mathbf{H}_e = -j\omega \nabla \times \mathbf{\Pi}_e, \tag{11}$$

which can also be written as

$$\nabla \times \left[\mathbf{E}_e + j\omega \mathbf{\Pi}_e\right] = 0. \tag{12}$$

From the vector identity $\nabla \times \left(-\nabla \phi_e\right) = 0$ and (12) it follows that

$$\mathbf{E}_e + j\omega \mathbf{\Pi}_e = -\nabla \phi_e, \tag{13}$$

or

$$\mathbf{E}_e = -\nabla \phi_e - j\omega \mathbf{\Pi}_e. \tag{14}$$

The scalar function ϕ_e represents an arbitrary electric scalar potential which is a function of position. Now we take the curl of both sides of (10) and use the vector identity $\nabla\times\nabla\times\mathbf{\Pi}_e = \nabla(\nabla\cdot\mathbf{\Pi}_e) - \nabla^2\mathbf{\Pi}_e$ which reduces it to

$$\nabla\times(u\,\mathbf{H}_e) = \nabla(\nabla\cdot\mathbf{\Pi}_e) - \nabla^2\mathbf{\Pi}_e . \tag{15}$$

From Maxwell's equation $\nabla\times\mathbf{H} = \mathbf{J} + j\omega\varepsilon_c\mathbf{E}$ where ε_c accounts for conductivity. Here we will simply use ε for the derivation, the equation to (15) leads to

$$\nabla^2\mathbf{\Pi}_e + k^2\mathbf{\Pi}_e = -u\,\mathbf{J} + [\nabla(\nabla\cdot\mathbf{\Pi}_e) + j\omega u\,\varepsilon\nabla\phi_e], \tag{16}$$

where $k^2 = \omega^2\mu\,\varepsilon$.

In (10), the curl of $\mathbf{\Pi}_e$ has been defined. Now, we are at liberty to define the divergence of $\mathbf{\Pi}_e$, which is independent of its curl. In order to simplify (16), let $\nabla\cdot\mathbf{\Pi}_e + j\omega u\,\varepsilon\,\phi_e = 0$ ➔ $\nabla\cdot\mathbf{\Pi}_e = -j\omega u\,\varepsilon\,\phi_e$, which is known as the Lorentz condition. Substituting it into (16) leads to

$$\nabla^2\mathbf{\Pi}_e + k^2\mathbf{\Pi}_e = -u\,\mathbf{J} . \tag{17}$$

Then take the z component lead (17) to

$$\nabla^2\Pi_{ez} + k^2\Pi_{ez} = -u\,\mathrm{J}_z . \tag{18}$$

In addition, (14) can reduce to

$$\mathbf{E}_e = -\nabla\phi_e - j\omega\mathbf{\Pi}_e = -j\omega\mathbf{\Pi}_e - j\frac{1}{\omega u\,\varepsilon}\nabla(\nabla\cdot\mathbf{\Pi}_e) . \tag{19}$$

Once $\mathbf{\Pi}_e$ is known, $\mathbf{H}_e$ can be found from (10) and $\mathbf{E}_e$ from (19). $\mathbf{E}_e$ can just as easily be found from Maxwell's equation $\nabla\times\mathbf{H}=\mathbf{J}+j\omega\varepsilon\mathbf{E}$ with $\mathbf{J}$ = 0. This will be shown in a later section on how to find $\mathbf{\Pi}_e$ in terms of the current density $\mathbf{J}$. It will be a solution to the inhomogeneous Helmholtz equation of (17).

3.1.3. Hertz Potential $\mathbf{\Pi}_h$ for a Magnetic Current Source $\mathbf{M}$

Although magnetic currents appear to be physically unrealizable, equivalent magnetic currents arise when we use the volume or the surface equivalence theorems. The fields generated by a harmonic magnetic current in a homogeneous region, with $\mathbf{J}=0$ but $\mathbf{M}\neq 0$, must satisfy $\nabla\cdot\mathbf{D}=0$. Therefore, $\mathbf{E}_h$ can be expressed as the curl of the Hertz potential $\mathbf{\Pi}_h$ by

$$\mathbf{E}_h=-\frac{1}{\varepsilon}\nabla\times\mathbf{\Pi}_h. \tag{20}$$

Substituting (20) into Maxwell's curl equation $\nabla\times\mathbf{H}_h=j\omega\varepsilon\mathbf{E}_h$, reduces it to

$$\nabla\times(\mathbf{H}_h+j\omega\mathbf{\Pi}_h)=0. \tag{21}$$

From the vector identity $\nabla\times(-\nabla\phi_e)=0$, it follows that

$$\mathbf{H}_h=-\nabla\phi_m-j\omega\mathbf{\Pi}_h, \tag{22}$$

where ϕ_m represents an arbitrary magnetic scalar potential that is a function of position. Taking the curl of (20)

$$\nabla\times\mathbf{E}_h=-\frac{1}{\varepsilon}\nabla\times\nabla\times\mathbf{\Pi}_h=-\frac{1}{\varepsilon}\left[\nabla\nabla\cdot\mathbf{\Pi}_h-\nabla^2\mathbf{\Pi}_h\right]. \tag{23}$$

And transforming it in to Maxwell's equation $\nabla \times \mathbf{E} = -\mathbf{M} - j\,\omega\,\mu\,\mathbf{H}$ leads to

$$\nabla^2 \mathbf{\Pi}_h + j\,\omega\,\mu\,\varepsilon\,\mathbf{H}_h = \nabla\nabla\cdot\mathbf{\Pi}_h - \varepsilon\,\mathbf{M}\,. \tag{24}$$

Substituting (22) into (24) reduces it to

$$\nabla^2 \mathbf{\Pi}_h + k^2\,\mathbf{\Pi}_h = -\varepsilon\,\mathbf{M} + \left[\nabla(\nabla\cdot\mathbf{\Pi}_h) + \nabla(j\omega\,\mu\,\varepsilon\,\phi_m)\right]. \tag{25}$$

By Lorentz condition, (25) reduces to

$$\nabla^2 \mathbf{\Pi}_h + k^2 \mathbf{\Pi}_h = -\varepsilon\,\mathbf{M}\,, \tag{26}$$

and (26) reduces to

$$\mathbf{H}_h = -j\,\omega\,\mathbf{\Pi}_h - j\frac{1}{\omega\,\mu\,\varepsilon}\nabla(\nabla\cdot\mathbf{\Pi}_h)\,. \tag{27}$$

Once $\mathbf{\Pi}_h$ is known, $\mathbf{E}_h$ can be found from (27) and $\mathbf{H}_h$ from (27) or (22) with $\mathbf{M}$ = 0. This will be shown in a later section on how to find $\mathbf{\Pi}_h$ in terms of the current density $\mathbf{M}$. $\mathbf{\Pi}_h$ will be a solution to the inhomogeneous Helmholtz equation of (26).

3.1.4. E- and M- Fields for Electric (J) and Magnetic (M) Current Sources

In previous sections we have developed equations that can be used to find the electric and magnetic fields generated by an electric current source $\mathbf{J}$ and a magnetic current source $\mathbf{M}$. This procedure requires that the auxiliary potential function $\mathbf{\Pi}_e$ and $\mathbf{\Pi}_h$ generated respectively, by $\mathbf{J}$ and $\mathbf{M}$ are found first. In turn,

the corresponding electric and magnetic fields are then determined ($\mathbf{E}_e$, $\mathbf{H}_e$ due to $\mathbf{\Pi}_e$ and $\mathbf{E}_h$, $\mathbf{H}_h$ due to $\mathbf{H}_h$). The total fields are then obtained by the superposition of the individual fields due to $\mathbf{H}_e$ and $\mathbf{H}_h$ ($\mathbf{J}$ and $\mathbf{M}$). Here is a summary that can be used to find the fields:

1. Specify $\mathbf{J}$ and $\mathbf{M}$ (electric and magnetic current density sources).

2. a. Find the $\mathbf{H}_e$ (due to $\mathbf{J}$) using

$$\mathbf{\Pi}_e = \frac{u}{4\pi}\iiint_V \mathbf{J}\frac{e^{-jk\mathbf{R}}}{\mathbf{R}}dv', \tag{28}$$

which is a solution of the inhomogeneous vector wave equation of (17) [19].

b. Find the $\mathbf{H}_h$ (due to $\mathbf{M}$) using

$$\mathbf{\Pi}_h = \frac{\varepsilon}{4\pi}\iiint_V \mathbf{M}\frac{e^{-jk\mathbf{R}}}{\mathbf{R}}dv', \tag{29}$$

which is a solution of the inhomogeneous vector wave equation of (26) [19].

3. a. Find the $\mathbf{H}_e$ using (10) and $\mathbf{E}_e$ using (19). $\mathbf{E}_e$ can also be found using Maxwell's equation $\nabla\times\mathbf{H} = \mathbf{J} + j\omega\varepsilon\mathbf{E}$ with $\mathbf{J}$ = 0.

b. Find $\mathbf{E}_h$ using (20) and $\mathbf{H}_h$ using (27). $\mathbf{H}_h$ which may also be found using Maxwell's equation of $\nabla\times\mathbf{E} = -\mathbf{M} - j\omega\mu\mathbf{H}$ with $\mathbf{M}$ = 0.

4. The total fields are then determined by

$$\mathbf{E} = \mathbf{E}_e + \mathbf{E}_h = -j\omega\mathbf{\Pi}_e - j\frac{1}{\omega\mu\varepsilon}\nabla(\nabla\cdot\mathbf{\Pi}_e) - \frac{1}{\varepsilon}\nabla\times\mathbf{\Pi}_h, \tag{30}$$

or

$$\mathbf{E} = \mathbf{E}_e + \mathbf{E}_h = \frac{1}{j\,\omega\,\varepsilon}\nabla\times\mathbf{H}_e - \frac{1}{\varepsilon}\nabla\times\mathbf{\Pi}_h\,, \tag{31}$$

and

$$\mathbf{H} = \mathbf{H}_e + \mathbf{H}_h = \frac{1}{\mu}\nabla\times\mathbf{\Pi}_e - j\,\omega\,\mathbf{\Pi}_h - j\frac{1}{\omega\,\mu\,\varepsilon}\nabla(\nabla\cdot\mathbf{\Pi}_h)\,, \tag{32}$$

or

$$\mathbf{H} = \mathbf{H}_e + \mathbf{H}_h = \frac{1}{\mu}\nabla\times\mathbf{\Pi}_e - \frac{1}{j\,\omega\mu}\nabla\times\mathbf{E}_h\,. \tag{33}$$

3.1.5. Solution of an Inhomogeneous Hertz Potential Wave Equation

In the previous section, we indicated that the solution of the inhomogeneous vector wave equation of (17) is (28). In equation (18), current density is directed along the z-axis (J_z), only a Π_{ez} component will exist and $\Pi_{ex} = 0$ and $\Pi_{ey} = 0$.

$$\nabla^2\,\Pi_{ez} + k^2\Pi_{ez} = -\mu\,J_z\,. \tag{34}$$

Hence we have

$$\nabla^2\Pi_{\mathrm{ez}} + k^2\Pi_{\mathrm{ez}} = -\mu\,(Il)\,\delta(r)\,. \tag{35}$$

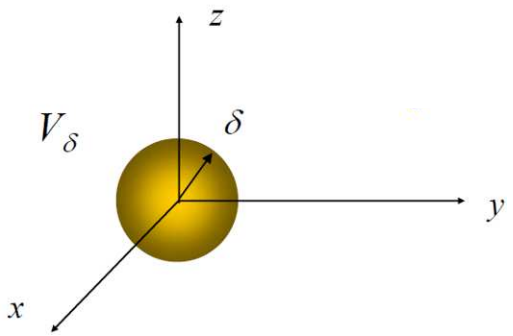

Figure 3. 4 Physical model of 3D delta function

The Π_{ez} field should be symmetric since the source is and "*r*" is the radial distance which

$$\delta(r)=\begin{cases}\lim\dfrac{1}{\frac{4}{3}\pi\delta^3}, & r\in V_\delta.\\ 0, \quad \text{otherwise.}\end{cases} \tag{36}$$

First, we assume $\Pi_{ez}(r)=R(r)$, for $r\neq 0$, we have

$$\nabla^2\Pi_{ez}+\mathrm{k}^2\Pi_{ez}=0\,. \tag{37}$$

Since in the limit the source is a point, it requires Π_{ez} is not a function of direction $(\theta \text{ and } \phi)$, thus (37) can be written as

$$\frac{1}{r^2}\frac{d}{dr}\left(r^2\frac{dR}{dr}\right)+k^2R=0\,. \tag{38}$$

The partial derivative has been replaced by the ordinary derivative since Π_{ez} is only a function of the radial coordinate. Next, let $R(r)=\dfrac{1}{r}h(r)$, as we expand the equation (38), which

$$r^2 \frac{dR(r)}{dr} = r^2 \left[\frac{1}{r} h'(r) - \frac{1}{r^2} h(r) \right] = r\, h'(r) - h(r), \tag{39}$$

so (38) can be rewritten as

$$\frac{1}{r^2} \frac{d}{dr} \left(r\, h'(r) - h(r) \right) + k^2 \frac{h(r)}{r} = 0, \tag{40}$$

$$\frac{1}{r^2} \left(h'(r) + r\, h''(r) - h'(r) \right) + k^2 \frac{h(r)}{r} = 0, \tag{41}$$

therefore (38) can finally be reduced to

$$h''(r) + k^2\, h(r) = 0. \tag{42}$$

Solution of (42) is

$$h(r) = A e^{-jkr} + B e^{+jkr}. \tag{43}$$

In the differential equation of (43), $A e^{-jkr}$ represents an outwardly (in the radial direction) traveling wave and $B e^{+jkr}$ describes an inwardly traveling wave (assuming an e^{jkr} time variation). For this problem, the source is placed at the origin with the radiated fields traveling in the outward radial direction. B = 0 is chosen to satisfy the radiation condition at infinity, hence the solution of (43) is

$$\Pi_{ez} = \frac{A}{r}\, e^{-jkr}. \tag{44}$$

To find the constant A, integrate the wave equation throughout a small spherical volume V_ε shown in Figure A.2:

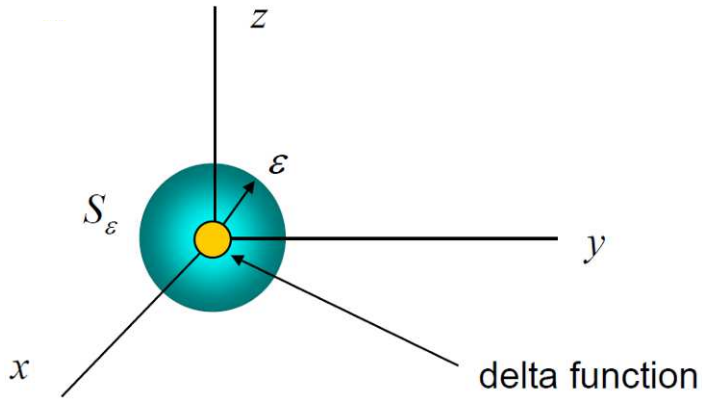

Figure 3. 5 Small spherical volume V_ε

First, we integrate (35) on both sides, leading to

$$\int_{V_\varepsilon} \nabla^2 \Pi_{ez}\, dV + k^2 \int_{V_\varepsilon} \Pi_{ez}\, dV = -\mu (Il)(1). \tag{45}$$

The first term of (45), which is

$$\int_{V_\varepsilon} \nabla^2 \Pi_{ez}\, dV = \int_{V_\varepsilon} \nabla \cdot (\nabla A_z)\, dV = \oint_{S_\varepsilon} \nabla A \cdot \hat{\underline{r}}\, dS\,, \tag{46}$$

and

$$\nabla A_z = \hat{\underline{r}} \frac{dA_z}{dr} = \hat{\underline{r}} \frac{d}{dr}\left(A \frac{e^{-jkr}}{r} \right) = \hat{\underline{r}} \left(-jk \frac{e^{-jkr}}{r} - \frac{1}{r^2} e^{-jkr} \right) A. \tag{47}$$

Hence

$$\begin{aligned} \int_{V_\varepsilon} \nabla^2 \Pi_{ez}\, dV &= \int_{S_\varepsilon} A \left(-jk \frac{e^{-jkr}}{r} - \frac{1}{r^2} e^{-jkr} \right) dS \\ &= 4\pi\varepsilon^2 \left[-jk \frac{e^{-jk\varepsilon}}{\varepsilon} - \frac{1}{\varepsilon^2} e^{-jk\varepsilon} \right] A \\ &= \left(-jk 4\pi\varepsilon\, e^{-jk\varepsilon} - 4\pi\, e^{-jk\varepsilon} \right) A. \end{aligned} \tag{48}$$

As $\varepsilon \to 0$:

$$\int_{V_\varepsilon} \nabla^2 \Pi_{ez}\, \mathrm{dV} = -4\pi \mathrm{A}. \tag{49}$$

For the second term of (45), we have

$$\begin{aligned}
\int_{V_\varepsilon} \Pi_{ez}\, dV &= \int_0^{2\pi}\int_0^{\pi}\int_0^{\varepsilon} \Pi_{ez}\, r^2 \sin\theta\, dr\, d\theta\, d\phi \\
&= (2\pi)(2)\int_0^{\varepsilon} \Pi_{ez}\, r^2\, dr \\
&= (4\pi)\left(\int_{\delta}^{\varepsilon} \Pi_{ez}\, r^2\, dr + \int_0^{\delta} \Pi_{ez}\, r^2\, dr\right) \\
&= (4\pi)\left[\int_{\delta}^{\varepsilon}\left(\frac{\Pi_{ez}\, e^{-jkr}}{r}\right) r^2\, dr + \int_0^{\delta} \Pi_{ez}\, r^2\, dr\right]. \\
&\to 0 \quad (as\ \varepsilon, \delta \to 0).
\end{aligned} \tag{50}$$

Equation (45) can be reduced to

$$\begin{aligned}
-4\pi A &= -\mu(Il). \\
\Rightarrow\ A &= \frac{\mu}{4\pi}(Il).
\end{aligned} \tag{51}$$

Once we derived the unknown constant A, the Hertz potential Π_{ez} in (44) can be written as

$$\Pi_{ez} = \frac{\mu}{4\pi}(Il)\frac{e^{-jkr}}{r}. \tag{52}$$

Finally, the Hertz potential of infinitesimal dipole equation (44) can be written as

$$\mathbf{\Pi}_{\mathbf{e}} = \hat{\mathbf{z}}\frac{\mu}{4\pi}(Il)\frac{e^{-\mathrm{j}\,\mathrm{k}\,\mathrm{r}}}{\mathrm{r}} = \left(\hat{\boldsymbol{r}}\cos\theta - \hat{\boldsymbol{\theta}}\sin\theta\right)\frac{\mu}{4\pi}(Il)\frac{e^{-jkr}}{r}. \tag{53}$$

The result in (53) is the Hertz potential for the infinitesimal dipole, which is located in the origin. For most cases, the dipole is not located at the origin and is not in the *z* position shown in Figure 3.6. Equation (53) for Figure 3.6 (a) can be written as

$$\mathbf{\Pi}_{\mathbf{e}} = \hat{\mathbf{z}}\frac{\mu}{4\pi}(Il)\frac{e^{-\mathrm{j}\,\mathrm{k}|\mathbf{r}-\mathbf{r}'|}}{|\boldsymbol{r}-\boldsymbol{r}'|}, \tag{54}$$

and for the arbitrary position $\hat{\mathbf{p}}$ other than $\hat{\mathbf{z}}$ direction, the (53) can be written as

$$\mathbf{\Pi}_{\mathbf{e}} = \hat{\mathbf{p}}\frac{\mu}{4\pi}(Il)\frac{e^{-\mathrm{j}\,\mathrm{k}|\mathbf{r}-\mathbf{r}'|}}{|\boldsymbol{r}-\boldsymbol{r}'|}. \tag{55}$$

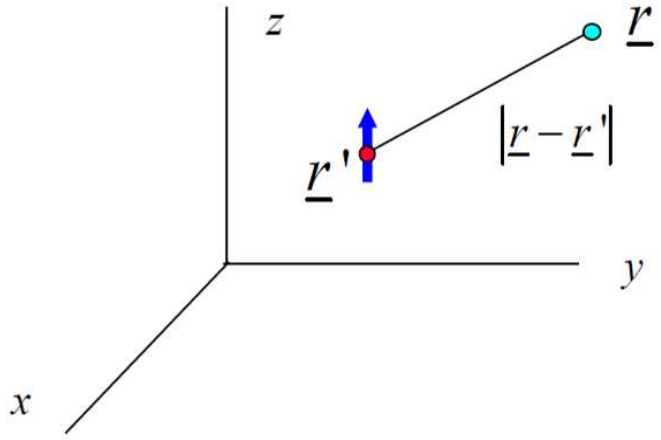

Figure 3. 6 Dipole removes from origin

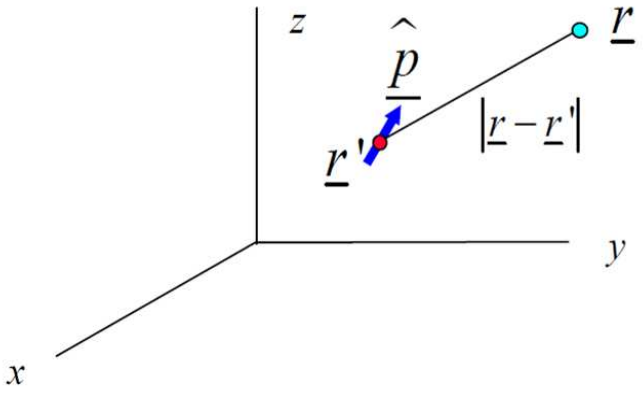

Figure 3. 7 Dipole removes from origin in arbitrary position

If the source is a volume current in an arbitrary position shown in Figure 3.8, then equation (53) can be written as

$$\mathbf{\Pi}_{\mathbf{e}} = \frac{\mu}{4\pi} \int_{\mathrm{V}} \boldsymbol{J}^{\boldsymbol{i}} \left(\mathrm{r}'\right) \frac{e^{-\mathrm{j}\,\mathrm{k}\left|\mathbf{r}-\mathbf{r}'\right|}}{\left|\boldsymbol{r}-\boldsymbol{r}'\right|} dV' \quad . \tag{55}$$

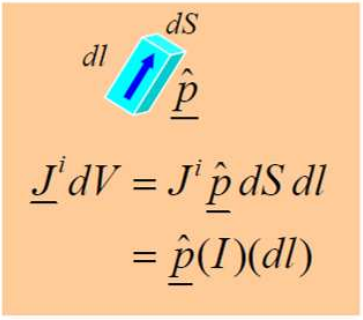

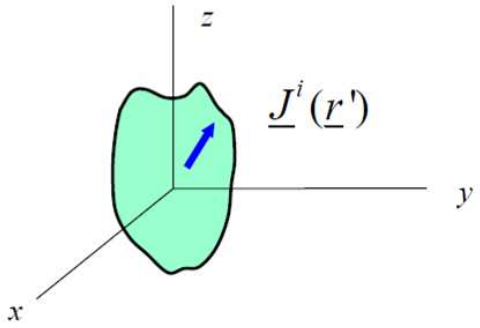

Figure 3. 8 Volume current sources

For filamental, surface, and volume currents, which were shown in Figure 3.8, the current densities for those cases can be written as

$$\boldsymbol{J}^{\boldsymbol{i}}\, dV \rightarrow \begin{cases} \boldsymbol{J}^{\boldsymbol{i}}\, dV & (volume current\, density) \\ \boldsymbol{J}^{\boldsymbol{i}}\, dS & (surface current\, density) \\ \boldsymbol{I}l\ dl & (filament current) \end{cases}. \tag{56}$$

The Hertz potential due to current sources from equation (56) can be written as

$$\boldsymbol{\Pi}_{\mathbf{e}}(\mathrm{r}) = \begin{cases} \dfrac{\mu}{4\pi}\displaystyle\int_{\mathrm{V}} \boldsymbol{J}_{V}^{i}(\boldsymbol{r}')\dfrac{\mathrm{e}^{-\mathrm{j}\mathrm{k}|\mathbf{r}-\mathbf{r}'|}}{|\boldsymbol{r}-\boldsymbol{r}'|}\mathrm{dV}' & (\mathrm{volume current density}) \\ \dfrac{\mu}{4\pi}\displaystyle\int_{\mathrm{S}} \boldsymbol{J}_{S}^{i}(\boldsymbol{r}')\dfrac{\mathrm{e}^{-\mathrm{j}\mathrm{k}|\mathbf{r}-\mathbf{r}'|}}{|\boldsymbol{r}-\boldsymbol{r}'|}\mathrm{dS} & (\mathrm{surface current density}) \\ \dfrac{\mu}{4\pi}\displaystyle\int_{\mathrm{C}} \hat{\boldsymbol{l}}(\boldsymbol{r}')\,\boldsymbol{I}_{e}^{i}(\boldsymbol{r}')\dfrac{\mathrm{e}^{-\mathrm{j}\mathrm{k}|\mathbf{r}-\mathbf{r}'|}}{|\boldsymbol{r}-\boldsymbol{r}'|}\mathrm{dl} & (\mathrm{filament current}) \end{cases}. \tag{57}$$

Using duality theorem, which describes the two different variables can be written as identical, the Hertz potential due to the electric current densities sources can be represented as Hertz potential due to magnetic current densities sources.

$$\boldsymbol{\Pi}_{\mathbf{h}}(\mathrm{r}) = \begin{cases} \dfrac{\varepsilon}{4\pi}\displaystyle\int_{\mathrm{V}} \boldsymbol{M}_{V}^{i}(\boldsymbol{r}')\dfrac{\mathrm{e}^{-\mathrm{j}\mathrm{k}|\mathbf{r}-\mathbf{r}'|}}{|\boldsymbol{r}-\boldsymbol{r}'|}\mathrm{dV}' & (\mathrm{volume current density}) \\ \dfrac{\varepsilon}{4\pi}\displaystyle\int_{\mathrm{S}} \boldsymbol{M}_{S}^{i}(\boldsymbol{r}')\dfrac{\mathrm{e}^{-\mathrm{j}\mathrm{k}|\mathbf{r}-\mathbf{r}'|}}{|\boldsymbol{r}-\boldsymbol{r}'|}\mathrm{dS} & (\mathrm{surface current density}) \\ \dfrac{\varepsilon}{4\pi}\displaystyle\int_{\mathrm{C}} \hat{\boldsymbol{l}}(\boldsymbol{r}')\,\boldsymbol{I}_{m}^{i}(\boldsymbol{r}')\dfrac{\mathrm{e}^{-\mathrm{j}\mathrm{k}|\mathbf{r}-\mathbf{r}'|}}{|\boldsymbol{r}-\boldsymbol{r}'|}\mathrm{dl} & (\mathrm{filament current}) \end{cases}. \tag{58}$$

3.1.6. Field Distribution

To find the fields radiated by the current element, the two-step procedure will be utilized as seen in Figure 3.1. The derived Hertz potential $\mathbf{\Pi_e}$ and $\mathbf{\Pi_h}$ will be used to find the $\mathbf{E}$ and $\mathbf{H}$ fields. Since the source only carries an electric current $\mathbf{I_e}$, the Hertz potential function $\mathbf{\Pi_h}$ and $\mathbf{I_h}$ are zero. To find the Hertz potential $\mathbf{\Pi_e}$ we may rewrite (56) to be

$$\mathbf{\Pi_e}(x,y,z) = \frac{\mu}{4\pi}\int_C \mathbf{I_e}\,(x',y',z')\frac{e^{-\mathrm{j}k\mathbf{R}}}{\mathbf{R}}dl' \ , \tag{59}$$

where (x,y,z) represent the observation point coordinate, (x',y',z') represent the coordinates of the source, $\mathbf{R}$ is the distance from any point on the source to the observation point, and path C is along the length of the source. In Figure 3.9, it shows the geometrical arrangement of an infinitesimal dipole and its associated electric-filed component on a spherical surface. For the infinitesimal dipole, $x' = y' = z' = 0$,

$$R = \sqrt{(x-x')^2 + (y-y')^2 + (z+z')^2} = r \quad \text{(constant)}, \tag{60}$$

$$\mathbf{I_e}\,(x',y',z') = \hat{\mathbf{a}}_\mathbf{z}\, I_0 \,, \tag{61}$$

$$dl' = d\,z' \,. \tag{62}$$

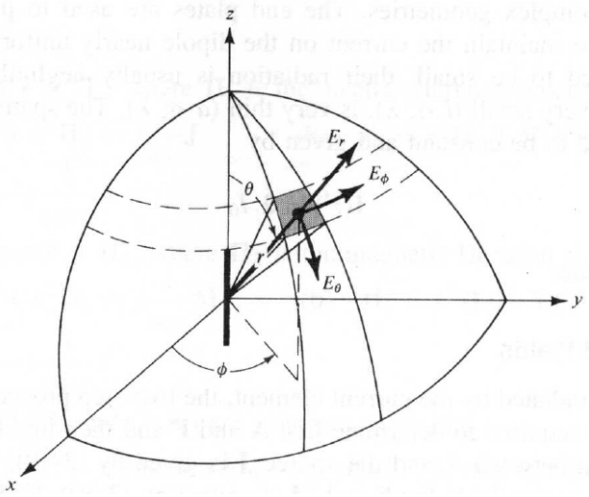

Figure 3. 9 The electric field components on a spherical surface.

Therefore, we can rewrite (59) as

$$\mathbf{\Pi_e}(x,y,z) = \hat{\mathbf{a}}_\mathbf{z}\frac{\mu I_0}{4\pi r}e^{-jkr}\int_{-l/2}^{+l/2} d\,z' = \hat{\mathbf{a}}_\mathbf{z}\frac{\mu I_0 l}{4\pi r}e^{-jkr}. \tag{63}$$

Next step is to find $\mathbf{H_e}$ using (10) and then $\mathbf{E_e}$ using (19) or Maxwell' equation (63) from once rectangular to spherical components using transformation function (64), by then using (10) and (19) in spherical coordinates to find $\mathbf{H}$ and $\mathbf{E}$.

$$\begin{bmatrix}\Pi_{er}\\ \Pi_{e\theta}\\ \Pi_{e\phi}\end{bmatrix} = \begin{bmatrix}\sin\theta\cos\phi & \sin\theta\sin\phi & \cos\theta\\ \cos\theta\cos\phi & \cos\theta\sin\phi & -\sin\theta\\ -\sin\phi & \cos\phi & 0\end{bmatrix}\begin{bmatrix}\Pi_{ex}\\ \Pi_{ey}\\ \Pi_{ez}\end{bmatrix}. \tag{64}$$

For this problem, $\Pi_{ex} = \Pi_{ey} = 0$, so (64) from (63) reduces to

$$\Pi_{er} = \Pi_{ez}\cos\theta = \frac{\mu I_0 l\, e^{-jkr}}{4\pi r}\cos\theta, \tag{65}$$

$$\Pi_{e\theta} = -\Pi_{ez} \sin\theta = \frac{\mu I_0 l e^{-jkr}}{4\pi r} \sin\theta, \tag{66}$$

$$\Pi_{e\phi} = 0. \tag{67}$$

Using the symmetry of the problem (no ϕ variations), (10) can be expanded into spherical coordinates and written in a simplified form as

$$\mathbf{H} = \hat{\mathbf{a}}_{\varphi} \frac{1}{\mu r}\left[\frac{\partial}{\partial r}\left(r \Pi_{e\theta}\right) - \frac{\partial \Pi_{er}}{\partial \theta}\right]. \tag{68}$$

Substituting (65) - (67) into (68) reduces it to

$$H_r = H_\theta = 0, \tag{69}$$

$$H_\phi = j \frac{k I_0 l \sin\theta}{4\pi r}\left[1 + \frac{1}{jkr}\right] e^{-jkr}. \tag{70}$$

The electric field **E** can now be found using (19) with **J** = 0. That is,

$$\mathbf{E} = \mathbf{E}_e = -j\omega \mathbf{\Pi}_e - j\frac{1}{\omega u \varepsilon_c} \nabla(\nabla \cdot \mathbf{\Pi}_e) = \frac{1}{j\omega\varepsilon_c} \nabla \times \mathbf{H}. \tag{71}$$

Substituting (65) - (67) or (69) - (70) into (71) reduces it to

$$E_r = \eta \frac{I_0 l \cos\theta}{2\pi r^2}\left[1 + \frac{1}{jkr}\right] e^{-jkr}, \tag{72}$$

$$E_\theta = j\eta \frac{k I_0 l \sin\theta}{4\pi r}\left[1 + \frac{1}{jkr} - \frac{1}{(kr)^2}\right] e^{-jkr}, \tag{73}$$

$$E_\phi = 0. \tag{74}$$

The E- and H-field components are valid everywhere, except on the source itself shown in Figure 3.9. At a distance $r = \lambda / 2\pi$ (or $k\,r = 1$), which is referred to as the radian distance. By determining the radian distance, we can derive the near-field ($k\,r << 1$) region, intermediate-field ($k\,r < 1$) region, and far-field ($k\,r >> 1$) region.

The condition of $k\,r << 1$ can be satisfied at moderate distances away from the antenna provided that the frequency of operation is very low. Equation (75) and (76) are similar to those of a static electric dipole and (78) to that of a static current element.

Near-Field ($k\,r << 1$) Region:

$$E_r \cong -j\eta \frac{I_0\, l\, e^{-jkr}}{2\pi\, k\, r^3} \cos\theta \tag{75}$$

$$E_\theta \cong -j\eta \frac{I_0\, l\, e^{-jkr}}{4\pi\, k\, r^3} \sin\theta \tag{76}$$

$$E_\phi = H_r = H_\theta = 0 \tag{77}$$

$$H_\phi \cong \frac{I_0\, l\, e^{-jkr}}{4\pi\, r^2} \sin\theta \tag{78}$$

$k\,r << 1.$

Intermediate-Field ($k\,r > 1$) Region:

$$E_r \cong \eta \frac{I_0\, l\, e^{-jkr}}{2\pi\, k\, r^2} \cos\theta \tag{79}$$

$$E_\theta \cong j\eta \frac{k\, I_0\, l\, e^{-jkr}}{4\pi\, r} \sin\theta \tag{80}$$

$$E_\phi = H_r = H_\theta = 0 \tag{81}$$

$$H_\phi \cong j \frac{k\, I_0\, l\, e^{-jkr}}{4\pi\, r} \sin\theta \tag{82}$$

$k\,r > 1.$

The total electric field is give by

$$\mathbf{E} = \hat{\mathbf{a}}_r\, E_r + \hat{\mathbf{a}}_\theta\, E_\theta, \tag{83}$$

whose magnitude can be written as

$$|\mathbf{E}| = \sqrt{|E_r|^2 + |E_\theta|^2}\ . \tag{84}$$

Far-Field ($k\,r >> 1$) Region:

$$E_\theta \cong j\eta \frac{k\, I_0\, l\, e^{-jkr}}{4\pi\, r} \sin\theta \tag{85}$$

$$E_r \cong E_\phi = H_r = H_\theta = 0 \tag{86}$$

$$H_\phi \cong j \frac{k\, I_0\, l\, e^{-jkr}}{4\pi\, r} \sin\theta \tag{87}$$

$k\,r >> 1.$

The ratio of E_θ and H_ϕ is equal to

$$Z_{\omega} = \frac{E_{\theta}}{H_{\phi}} \cong \eta \,, \tag{88}$$

where Z_{ω} is a wave impedance and η is a intrinsic impedance. The E- and H-field components are perpendicular to each other, and are transverse to the radial direction of propagation, while the *r* variations are separable from those of θ and ϕ.

3.1.7. Infinitesimal Dipole Model

In this section, the infinitesimal dipole model of the dielectric constant tool is shown in Figure 3.10, consisting of a perfectly conducted half-space $z \le 0$, which is separated from the formation by a layer of mud cake. In our model, three infinitesimal dipoles represent the transmitting and receiving antenna of the dielectric constant tool. The EM property of each layer is described by ε_1, μ_1 (formation) and ε_2, μ_2 (mud cake). On the interface between the mud cake and the perfectly conducting half-space, there is a transmitting antenna T at the origin and two receiving antennas R_1 and R_2 at x_1 and x_2 respectively. Using this model, we calculate the electric field detected by each of the two receivers using the equations derived above. Since the receivers are located at z = 0, the electric fields detected at R_1 and R_2 have only a $\boldsymbol{z}$ - component. This comes from the

boundary condition that the tangential component of the electric field must vanish on the surface of a perfect conductor.

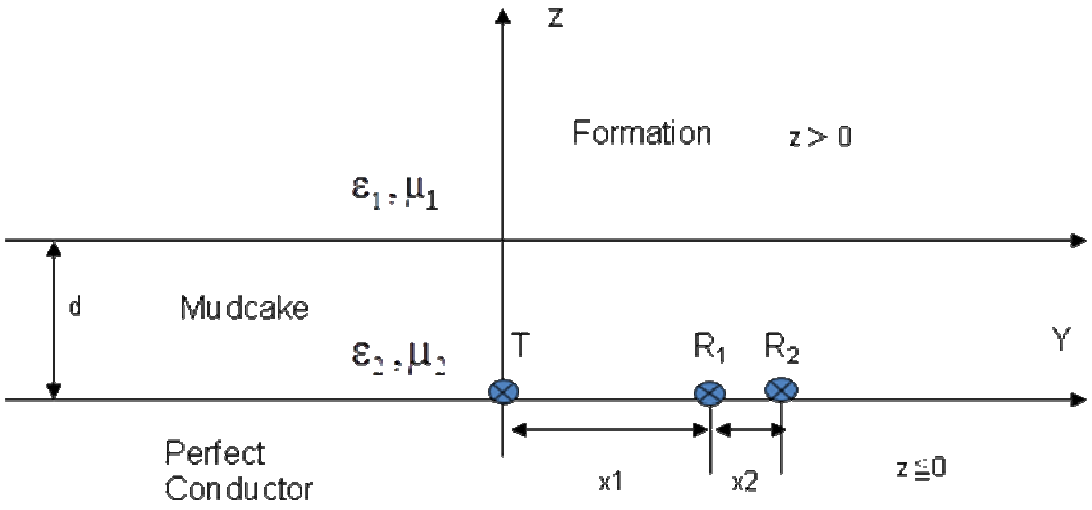

Figure 3.10 An infinitesimal dipole model

3.2. Duality Theorem

When two equations that describe the behavior of two different variables are of the same mathematical form, their solutions will also be identical. The variables in two equations that occupy identical positions are known as *dual* quantities and a solution of one can be formed by a systematic interchange of symbols to the other. This concept is known as the *duality theorem*.

The real practices of duality theorem can be seen in previous derived equations. Comparing equations (10), (17), and (19) to (20), (26), and (27) respectively shows that they are dual equations to each other and their variables

are dual quantities. Thus, knowing the solutions to one set $(\text{i.e., } \mathbf{J} \neq 0, \mathbf{M} = 0)$, the solution to the other set $(\mathbf{J} = 0, \mathbf{M} \neq 0)$ can be formed by a proper interchange of quantities. Table 3.1 shows the substitutions of Maxwell's equations which are unaffected. Duality only serves as a guide in forming mathematical solutions. However, it must be emphasized that this is purely mathematical in nature since it is known, as of today, that there are no magnetic charges or currents in nature.

Table 3.1 Substitutions of Maxwell's Equation for Duality

$\boldsymbol{E}$	$\Rightarrow$	$\boldsymbol{H}$	$\boldsymbol{J}^i$	$\Rightarrow$	$\boldsymbol{M}^i$
$\boldsymbol{H}$	$\Rightarrow$	$-\boldsymbol{E}$	$\boldsymbol{M}^i$	$\Rightarrow$	$-\boldsymbol{J}^i$
$\varepsilon, \varepsilon_c$	$\Rightarrow$	μ, μ_c	ρ_v	$\Rightarrow$	ρ_v^m
μ, μ_c	$\Rightarrow$	$\varepsilon, \varepsilon_c$	ρ_v^m	$\Rightarrow$	$-\rho_v$

Example:

$$\nabla \times \boldsymbol{E} = -\boldsymbol{M}^i - j\omega\mu\,\boldsymbol{H}$$
$$\Downarrow$$
$$\nabla \times \boldsymbol{H} = -\left(-\boldsymbol{J}^i\right) - j\omega\varepsilon_c\,(-\boldsymbol{E})$$
$$\Downarrow$$
$$\nabla \times \boldsymbol{H} = \boldsymbol{J}^i + j\omega\varepsilon_c\,\boldsymbol{E}$$

Example:

$$\nabla \times \boldsymbol{H} = \boldsymbol{J}^i + j\omega\varepsilon_c\,\boldsymbol{E}$$
$$\Downarrow$$
$$\nabla \times (-\boldsymbol{E}) = \boldsymbol{M}^i + j\omega\mu_c\,\boldsymbol{H}$$
$$\Downarrow$$
$$\nabla \times \boldsymbol{E} = -\boldsymbol{M}^i - j\omega\mu_c\,\boldsymbol{H}$$

3.3. Equivalence Principle

The basic idea of the equivalence principle is that we can replace the actual sources in a region by equivalent sources at the boundary of a closed surface.

The fictitious sources are said to be equivalent within a region because they produce the same fields within that region. By the equivalence principle, the fields outside an imaginary closed surface are obtained by placing over the closed surface suitable electric and magnetic current densities which then satisfies the boundary conditions. In Figure 3.11, we keep the original field $\mathbf{E}$ and $\mathbf{H}$ outside of the surface, and then put the zero field inside the surface concluding that there is no source. The ($\mathbf{E}^a$, $\mathbf{H}^a$) and ($\mathbf{E}^b$, $\mathbf{H}^b$) both satisfy the Maxwell's equation.

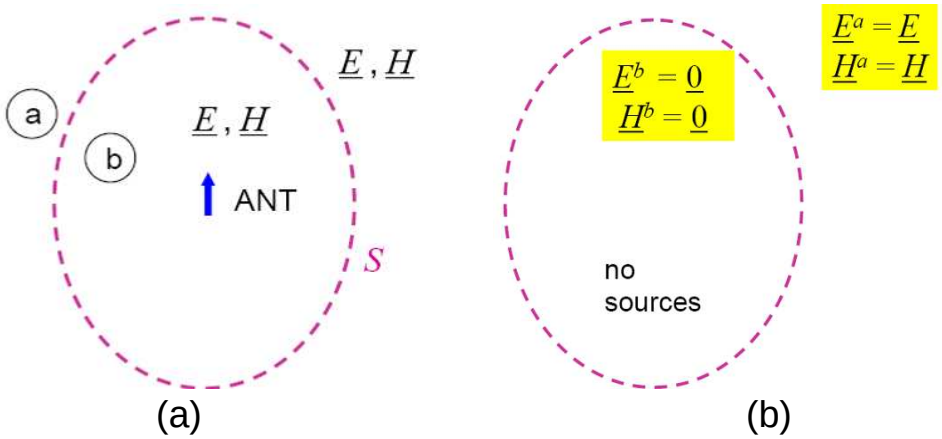

Figure 3.11 Actual source (a) and zero field inside surface (b)

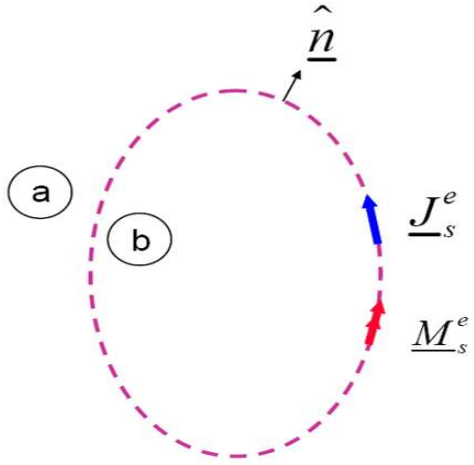

Figure 3.12 Equivalent source $\boldsymbol{J}_S^e$ and $\boldsymbol{M}_S^e$ on the surface

In the Figure 3.12, the imaginary surface S, the equivalent sources (89) and (90) radiate into an unbounded space (which is considered the same medium everywhere). The current density of equations (89) and (90) are said to be equivalent only within the outside surface S, because they produce the original fields ($\mathbf{E}^a$, $\mathbf{H}^a$) only outside S. Since the current of (89) and (90) radiate in an unbounded space, the fields can be determined using equations (28) – (33).

$$\boldsymbol{J}_S^e = \hat{\mathrm{n}} \times (H^a - \cancel{H^b}^{0}), \tag{89}$$

$$\boldsymbol{M}_S^e = -\hat{\mathrm{n}} \times (E^a - \cancel{E^b}^{0}). \tag{90}$$

3.4. Aperture Antenna

In this section, we will discuss the cavity-backed slot antenna for both the field distribution equations and simulation model.

3.4.1. Radiation

The field radiated by sources $\boldsymbol{J}_S$ and $\boldsymbol{M}_S$, which are equivalent sources on the imaginary surface S, in an unbounded medium can be computed by using (28) - (33) where the integration must be performed over the entire surface occupied by $\boldsymbol{J}_S$ and $\boldsymbol{M}_S$ shown in Figure 3.12. These equations yield valid solutions for all observation points. For most problems, the main difficulty is the inability to

perform the integrations in (28) and (29). However for far-field observations, the complexity of the formulation can be reduced.

For the far-field observations $\boldsymbol{R}$ can most commonly be approximated by

$$\boldsymbol{R} \cong r - r' \cos\psi, \qquad \text{for phase variation,} \tag{91}$$

$$\boldsymbol{R} \cong r, \qquad \text{for amplitude variation,} \tag{92}$$

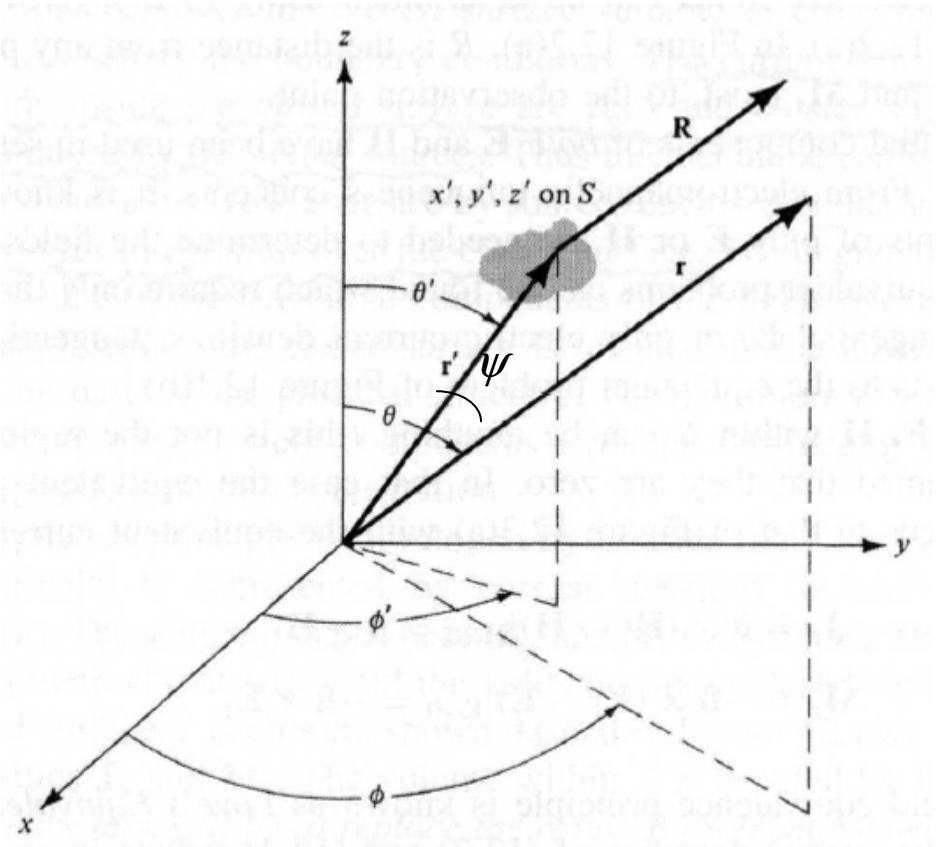

Figure 3.13 Coordinate system for aperture antenna analysis [20]

where ψ is the angle between the vector r and r', as show in Figure 3.13. The primed coordinates $(x', y', z', \text{or } r', \theta', \phi')$ indicate the space occupied by the sources $\boldsymbol{J}_s$ and $\boldsymbol{M}_s$, over which integration must be performed. The unprimed

coordinates $(x, y, z, \text{or } r, \theta, \phi)$ represent the observation point. Geometrically the approximation of (91) assumes that the vectors **R** and **r** are parallel, as shown in Figure 3.13.

Using (91) and (92), (28) and (29) cab be written as

$$\mathbf{\Pi_e} = \frac{\mu}{4\pi}\iint_S \mathbf{J_s}\frac{e^{-jkR}}{\boldsymbol{R}}ds' \cong \frac{u\,e^{-jkr}}{4\,\pi\,r}\mathbf{\Lambda}\,, \tag{93}$$

$$\mathbf{\Lambda} = \iint_S \mathbf{J_s}\, e^{jkr'\,\cos\psi}\, ds'\,, \tag{94}$$

$$\mathbf{\Pi}_h = \frac{\varepsilon}{4\pi}\iint_S \mathbf{M_s}\frac{e^{-jkR}}{\boldsymbol{R}}ds' \cong \frac{u\,e^{-jkr}}{4\,\pi\,r}\mathbf{\Psi}\,, \tag{95}$$

$$\mathbf{\Psi} = \iint_S \mathbf{M_s}\, e^{jkr'\,\cos\psi}\, ds'\,, \tag{96}$$

In the far field only the θ and ψ components of the **E-** and **H-**field are dominant, which are

$$\mathbf{E}_e \cong -\mathrm{j}\,\omega\mathbf{\Pi}_e \;\Rightarrow\; \begin{cases} \mathrm{E}_r \cong 0 \\ \mathrm{E}_\theta \cong -\mathrm{j}\,\omega\,\mathbf{\Pi}_{e\theta} \\ \mathrm{E}_\phi \cong -\mathrm{j}\,\omega\,\mathbf{\Pi}_{e\phi} \end{cases}, \tag{97}$$

$$\mathbf{H}_e \cong -\mathrm{j}\frac{\omega}{\eta}\hat{\mathbf{a}}_\mathrm{r}\times\mathbf{\Pi}_e \;\Rightarrow\; \begin{cases} \mathrm{H}_r \cong 0 \\ \mathrm{H}_\theta \cong -\dfrac{\mathrm{E}_\phi}{\eta} \\ \mathrm{H}_\phi \cong +\dfrac{\mathrm{E}_\theta}{\eta} \end{cases}, \tag{98}$$

due to an electric source **J.** Similarly, the far-zone field due to a magnetic source **M** can be written as

$$\mathbf{H}_h \cong -\mathrm{j}\,\omega\,\mathbf{\Pi}_h \;\Rightarrow\; \begin{cases} \mathrm{H}_r \cong 0 \\ \mathrm{H}_\theta \cong -\mathrm{j}\,\omega\,\mathbf{\Pi}_{h\theta} \\ \mathrm{H}_\phi \cong -\mathrm{j}\,\omega\,\mathbf{\Pi}_{h\phi} \end{cases}, \tag{99}$$

$$\mathbf{E}_\mathrm{h} \cong j\,\omega\,\eta\,\hat{\mathbf{a}}_r \times \mathbf{\Pi}_\mathrm{h} \;\Rightarrow\; \begin{cases} E_\mathrm{r} \cong 0 \\ E_\theta \cong \eta\,H_\phi \\ E_\phi \cong -\eta\,H_\theta \end{cases}. \tag{100}$$

Using (97) ~ (100), the $\mathbf{E}_\mathrm{e}$ of (30) and $\mathbf{H}_\mathrm{h}$ of the (32) can be rewritten as

$$\left(\mathbf{E}_\mathrm{e}\right)_\theta \cong -j\,\omega\,\mathbf{\Pi}_{\mathrm{e}\theta}, \tag{101}$$

$$\left(\mathbf{E}_\mathrm{e}\right)_\phi \cong -j\,\omega\,\mathbf{\Pi}_{\mathrm{e}\phi}, \tag{102}$$

$$\left(\mathbf{H}_\mathrm{h}\right)_\theta \cong -j\,\omega\,\mathbf{\Pi}_{\mathrm{h}\theta}, \tag{103}$$

$$\left(\mathbf{H}_\mathrm{h}\right)_\phi \cong -j\,\omega\,\mathbf{\Pi}_{\mathrm{h}\phi}, \tag{104}$$

and $\boldsymbol{E}_h$ of (30) and $\boldsymbol{H}_e$ of (32), with aid of (101) ~ (104) can be rewritten as

$$\left(\mathbf{E}_\mathrm{h}\right)_\theta \cong +\eta\left(\mathbf{H}_\mathrm{h}\right)_\phi = -j\,\omega\,\eta\,\mathbf{\Pi}_{\mathrm{h}\phi}, \tag{105}$$

$$\left(\mathbf{E}_\mathrm{h}\right)_\phi \cong -\eta\left(\mathbf{H}_\mathrm{h}\right)_\theta = +j\,\omega\,\eta\,\mathbf{\Pi}_{\mathrm{h}\theta}, \tag{106}$$

$$\left(\mathbf{H}_\mathrm{e}\right)_\theta \cong -\frac{\left(\mathbf{E}_\mathrm{e}\right)_\phi}{\eta} = +j\,\omega\,\frac{\mathbf{\Pi}_{\mathrm{e}\phi}}{\eta}, \tag{107}$$

$$\left(\mathbf{H}_\mathrm{e}\right)_\phi \cong +\frac{\left(\mathbf{E}_\mathrm{e}\right)_\theta}{\eta} = -j\,\omega\,\frac{\mathbf{\Pi}_{\mathrm{e}\theta}}{\eta}. \tag{108}$$

Combining (101) ~ (104) with (105) ~ (108), the total **E**- and **H**-fields can be written as

$$\mathrm{E}_{\mathrm{r}} \cong 0\,, \tag{109}$$

$$\mathrm{E}_{\theta} \cong -\frac{j\,k\,e^{-j\,k\,r}}{4\pi\,r}(\Psi_{\phi} + \eta\Lambda_{\theta})\,, \tag{110}$$

$$\mathrm{E}_{\phi} \cong +\frac{j\,k\,e^{-j\,k\,r}}{4\pi\,r}(\Psi_{\phi} - \eta\Lambda_{\theta})\,, \tag{111}$$

$$\mathrm{H}_{\mathrm{r}} \cong 0\,, \tag{112}$$

$$\mathrm{H}_{\theta} \cong \frac{j\,k\,e^{-j\,k\,r}}{4\pi\,r}(\Lambda_{\theta} - \frac{\Psi_{\phi}}{\eta})\,, \tag{113}$$

$$\mathrm{H}_{\phi} \cong -\frac{j\,k\,e^{-j\,k\,r}}{4\pi\,r}(\Lambda_{\theta} + \frac{\Psi_{\phi}}{\eta})\,. \tag{114}$$

The Λ_{θ}, Λ_{ϕ}, Ψ_{θ}, and Ψ_{φ} can be obtained from (94) and (96). That is,

$$\mathbf{\Lambda} = \iint_{S} \mathbf{J}_{\mathrm{s}}\, e^{\,j\,k\,r'\,\cos\psi}\, ds' = \iint_{S} (\hat{\mathbf{a}}_{x} J_{x} + \hat{\mathbf{a}}_{y} J_{y} + \hat{\mathbf{a}}_{z} J_{z})\, e^{+\,j\,k\,r'\,\cos\psi}\, ds'\,, \tag{115}$$

$$\mathbf{\Psi} = \iint_{S} \mathbf{M}_{\mathrm{s}}\, e^{\,j\,k\,r'\,\cos\psi}\, ds' = \iint_{S} (\hat{\mathbf{a}}_{x} M_{x} + \hat{\mathbf{a}}_{y} M_{y} + \hat{\mathbf{a}}_{z} M_{z})\, e^{+\,j\,k\,r'\,\cos\psi}\, ds'\,. \tag{116}$$

Using the rectangular to spherical component transformation, obtained by taking the inverse (in this case also the transposing) of (64), (115) and (116) which reduces the θ and ψ components to

$$\Lambda_{\theta} = \iint_{\mathrm{S}} (J_{\mathrm{x}}\, cos\,\theta\, cos\,\phi + J_{\mathrm{y}}\, cos\,\theta\, sin\,\phi - J_{\mathrm{z}}\, sin\,\theta)\, e^{+\,j\,k\,r'\,cos\,\psi}\, \mathrm{ds}'\,, \tag{117}$$

$$\Lambda_{\phi} = \iint_{S} (-\mathrm{J}_x \sin\phi + \mathrm{J}_y \cos\phi) \mathrm{e}^{+\mathrm{j}\,k\,r'\cos\psi} ds' , \quad (118)$$

$$\Psi_{\theta} = \iint_{S} (\mathrm{M}_x \cos\theta \cos\phi + \mathrm{M}_y \cos\theta \sin\phi + \mathrm{M}_z \sin\theta) e^{+j\,k\,r'\cos\psi} \mathrm{d}s' , \quad (119)$$

$$\Psi_{\phi} = \iint_{S} (-M_x \sin\phi + M_y \cos\phi) \mathrm{e}^{+\mathrm{j}\,k\,r'\cos\psi} ds' . \quad (120)$$

3.4.2. Rectangular Apertures

Figure 3.14 shows the rectangular aperture on an infinite electric ground plan with the coordinate geometry indicated. In practice, the rectangular aperture is probably the most common microwave antenna. Because of its configuration, the rectangular coordinate system is the most convenient system to express the fields at the aperture and to perform the integration. The components of the equivalent current densities are

$$\boldsymbol{J}_x, \boldsymbol{J}_y, \boldsymbol{M}_x, \boldsymbol{M}_y. \quad (121)$$

The difference in paths from the source to the observation point ($r' \cos\psi$) which is

$$r' \cos\psi = \mathbf{r}' \cdot \hat{\mathbf{a}}_{\mathrm{r}} = \left(\hat{\mathbf{a}}_{\mathrm{x}} x' + \hat{\mathbf{a}}_{\mathrm{y}} y'\right) \cdot \left(\hat{\mathbf{a}}_{\mathrm{x}} \sin\theta \cos\varphi + \hat{\mathbf{a}}_{\mathrm{y}} \sin\theta \sin\varphi + \hat{\mathbf{a}}_{\mathrm{z}} \cos\theta\right) = x' \sin\theta \cos\varphi + y' \sin\theta \sin\varphi . \quad (122)$$

And the differential areas are represented by

$$ds' = dx'\, dy' . \quad (123)$$

To reduce the mathematical complexities, the field over the opening is assumed to be constant and given by

$$\mathbf{E}_{\mathrm{a}} = \hat{\mathbf{a}}_y E_0, \qquad -a/2 \leqq x' \leqq a/2,\ -b/2 \leqq y' \leqq b/2, \tag{124}$$

$$\mathbf{H}_{\mathrm{a}} = \hat{\mathbf{a}}_{\mathrm{x}} \frac{E_0}{\eta}, \qquad -a/2 \leqq x' \leqq a/2,\ -b/2 \leqq y' \leqq b/2, \tag{125}$$

where E_0 is a constant. In order to form the equivalent, according to the equivalence principle in section 3.3, a closed surface is chosen that extends from one end of the x-y plane to the other end. The equivalent source is

$$\left.\begin{aligned} \mathbf{M}_S &= -\hat{\mathbf{n}} \times \mathbf{E}_a = -\hat{\mathbf{a}}_{\mathbf{z}} \times \hat{\mathbf{a}}_{\mathbf{y}} E_0 = \hat{\mathbf{a}}_{\mathbf{x}} E_0 \\ \mathbf{J}_S &= \hat{\mathbf{n}} \times \mathbf{H}_a = \hat{\mathbf{a}}_{\mathbf{z}} \times (-\hat{\mathbf{a}}_{\mathbf{x}}) \frac{E_0}{\eta} = -\hat{\mathbf{a}}_{\mathbf{y}} \frac{E_0}{\eta} \end{aligned}\right\} -\mathrm{a}/2 \le \mathrm{x}' \le \mathrm{a}/2\,,\ -\mathrm{b}/2 \le \mathrm{y}' \le \mathrm{b}/2\,, \tag{126}$$

$$\mathbf{M}_{\mathrm{S}} \cong \mathbf{J}_{\mathrm{S}} \cong 0, \qquad \textit{elsewhere}.$$

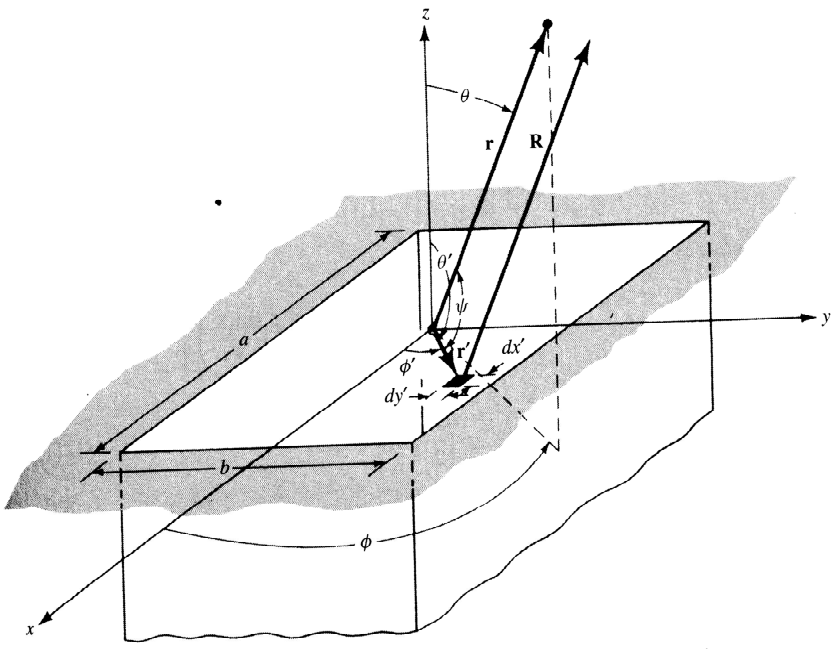

Figure 3.14 Rectangular aperture on finite electric ground plan

The far zone fields radiated by the aperture of Figure 3.14 can be found by using (109) ~ (114), (117) ~ (120), (121) ~ (123), and (126) which are

$$\Lambda_\theta = \iint_S \mathbf{J}_y \cos\theta \sin\phi \, e^{+jk\,(x'\sin\theta\cos\varphi + y'\sin\theta\sin\varphi)} dx'\,dy'$$

$$= \cos\theta \sin\phi \left[\int_{-b/2}^{b/2} \int_{-a/2}^{a/2} -\frac{E_0}{\eta} \; e^{+jk\,(x'\sin\theta\cos\varphi + y'\sin\theta\sin\varphi)} dx'\,dy' \right]. \quad (127)$$

In (127), the integral represented within the brackets represents the space factor for a two-dimensional distribution. For the Λ_θ component of the Hertz potential $\mathbf{\Pi}_h$, the element factor is equal to the factor outside the brackets in (127). The total field is equal to the product of the element and space factors.

Using the integral

$$\int_{-c/2}^{c/2} e^{j\alpha z} dz = c \left[\frac{\sin\left(\frac{\alpha}{2} c\right)}{\frac{\alpha}{2} c} \right], \quad (128)$$

(127) reduces to

$$\Lambda_\theta = -\frac{ab\,E_0}{\eta} \left[\cos\theta \sin\phi \, \frac{\sin X}{X} \frac{\sin Y}{Y} \right], \quad (129)$$

where

$$X = \frac{ka}{2} \sin\theta \cos\phi, \quad (130)$$

$$Y = \frac{kb}{2} \sin\theta \sin\phi. \quad (131)$$

Similarly, it can be shown Λ_ϕ, Ψ_θ, and Ψ_ϕ as

$$\Lambda_{\phi} = -\frac{ab\,\mathrm{E}_0}{\eta}\left[\cos\phi\,\frac{sinX}{X}\,\frac{sinY}{Y}\right], \tag{132}$$

$$\Psi_{\theta} = ab\,\mathrm{E}_0\left[\cos\theta\,\cos\phi\,\frac{sinX}{X}\,\frac{sinY}{Y}\right], \tag{133}$$

$$\Psi_{\phi} = -ab\,\mathrm{E}_0\left[\sin\phi\,\frac{sinX}{X}\,\frac{sinY}{Y}\right]. \tag{134}$$

Substituting (129) and (132) ~ (134) into (109) ~ (115), the fields radiated by the aperture can be written as

$$E_r = 0, \tag{135}$$

$$E_\theta = \frac{\mathrm{C}}{2}(1+\cos\theta)\left[\sin\phi\,\frac{\mathrm{sinX}}{\mathrm{X}}\,\frac{\mathrm{sinY}}{\mathrm{Y}}\right], \tag{136}$$

$$E_\phi = \frac{\mathrm{C}}{2}(1+\cos\theta)\left[\cos\phi\,\frac{\mathrm{sinX}}{\mathrm{X}}\,\frac{\mathrm{sinY}}{\mathrm{Y}}\right], \tag{137}$$

$$H_r = 0, \tag{138}$$

$$H_\theta = -\frac{E_\phi}{\eta}, \tag{139}$$

$$H_\phi = +\frac{E_\theta}{\eta}, \tag{140}$$

where

$$\mathrm{C} = \frac{j\,a\,b\,\mathrm{E}_0\,k\,e^{-jkr}}{2\pi r}. \tag{141}$$

Equations (135) ~ (140) represent the three-dimensional distributions of the far-zone fields radiated by the aperture. Experimentally, only two-dimensional plots can be measured. In many applications, only a pair of two-dimensional plots are usually sufficient, which are E- and H-plane patterns. For the problem in Figure 3.14, the E-plane pattern is on the y-z plane ($\phi = \pi/2$) and the H-plane is on the x-z plane ($\phi = 0$). Thus

E-Plane ($\phi = \pi/2$)

$$E_r = E_\phi = 0, \tag{142}$$

$$E_\theta \cong \frac{\mathrm{C}}{2}(1+\cos\theta)\left[\frac{\sin\left(\frac{k\,b}{2}\sin\theta\right)}{\frac{k\,b}{2}\sin\theta}\right]. \tag{143}$$

H-Plane ($\phi = 0$)

$$E_r = E_\theta = 0, \tag{144}$$

$$E_\theta \cong \frac{\mathrm{C}}{2}(1+\cos\theta)\left[\cos\theta\,\frac{\sin\left(\frac{k\,a}{2}\sin\theta\right)}{\frac{k\,a}{2}\sin\theta}\right]. \tag{145}$$

3.4.3. HFSS model

The EPT tool consists of two transmitting (T) and two receiving (R) antennas arranged in a vertical symmetric configuration T1 - R1 - R2 - T2 on a brass pad, which is pressed against the borehole shown in Figure 3.15. The antennas used

in EPT are cavity-backed slot antennas which are tuned to transmit and receive microwave radiation at a frequency of 1 GHz. The distance from each receiver to the nearest transmitter is 8 cm, and the receivers are 4 cm apart shown in Figure 3.16. The slot of the antennas designs is estimated to be a half wavelength long, which is the length of a resonant dipole antenna. Because its radiation resistance is 73 ohms, which is very close to 50-ohm and 75-ohm characteristic impedances of some transmission lines.

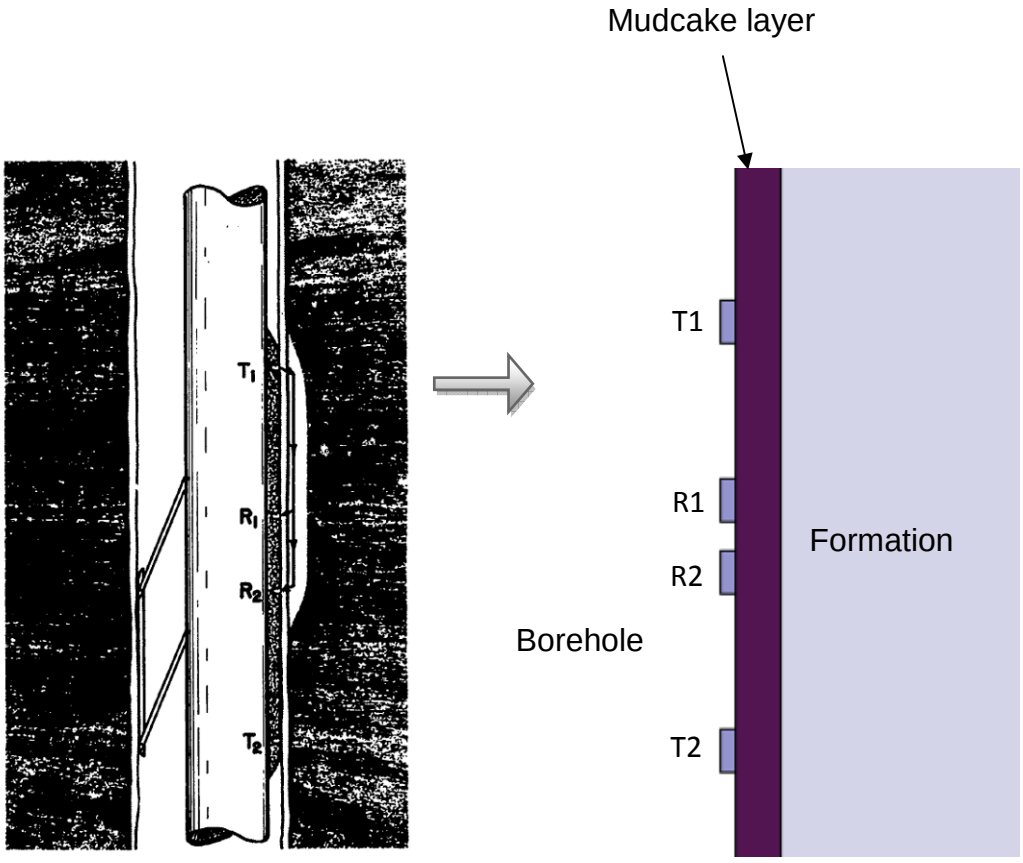

Figure 3.15 A schematic diagram of the EPT tool in a borehole side view

Due to the short transmitter-to-receiver spacing and the attenuation of the signal, the depth of investigation of the EPT is limited to the invaded or flushed zone of the formation. Figure 3.15 shows that a hydraulically powered backup arm helps the antenna pad maintain contact with the borehole wall and also provides a caliper reading of the borehole. The transmitting antennas are placed above and below the receiver pair, and are pulsed alternately. Simple geometric considerations show that if these two transmission modes are averaged, the first-order effects of the pad tilt will be eliminated [21].

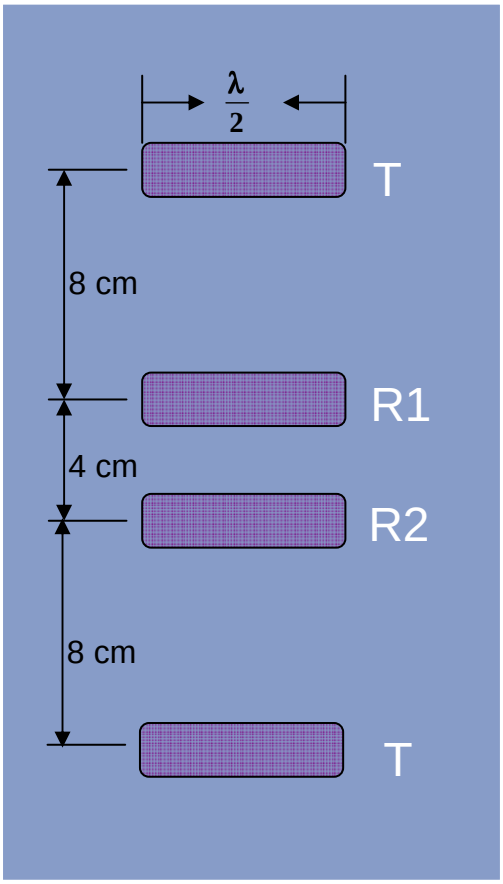

Figure 3.16 A schematic of antenna pad of EPT front view

A geometric model that takes into account the slot nature of the EPT antennas is the aperture model shown in Figure 3.17. This model represents the EPT antenna as a rectangular waveguide and rigorously models the interactions between the receivers and the transmitters. This aperture model also ignores the curvature and the finite extent of the EPT pad, thus neglecting the reflection and depolarization of the wave at the pad edges. Moreover, the model takes into account the dominant geometric effects of the EPT structure, combined with the effects of multiple scattering between the transmitters and receivers.

This model divides the problem into three parts: the region inside the transmitting antenna, the regions inside the receiving antennas, and the medium outside the antennas. The electromagnetic fields inside the antennas are represented as sums of the waveguide modes. Similarly, the fields inside the receivers are expressed as sums of waveguide modes, accounting for coupling effects from the transmitter to the other antennas. The transmitter's waveguide modes are coupled to the receivers' waveguide modes through the external fields.

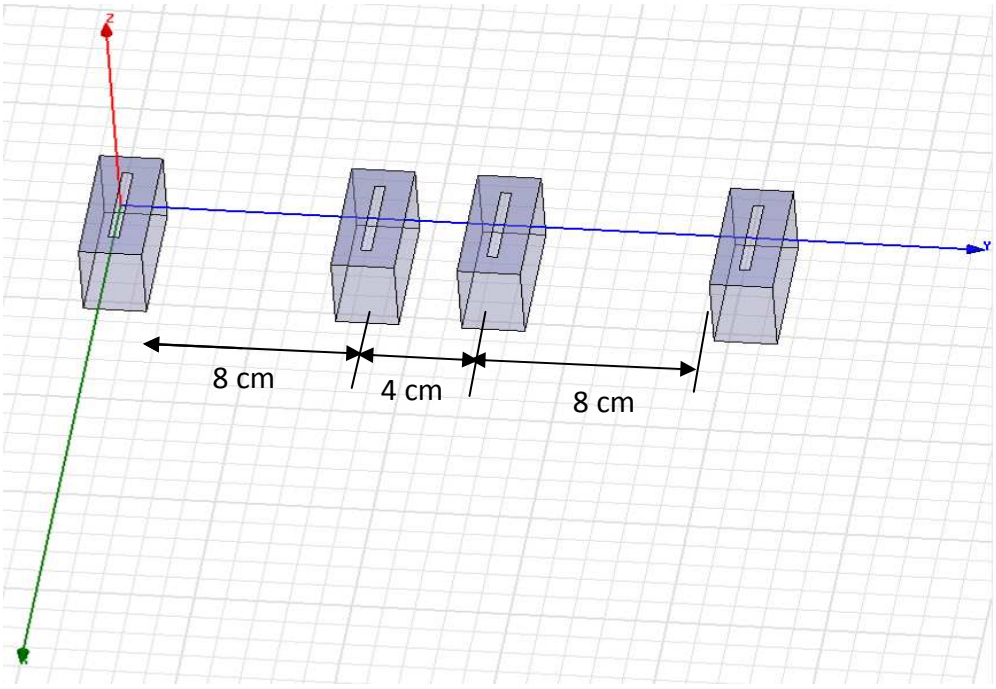

Figure 3.17 A schematic of slot antenna configurations of EPT

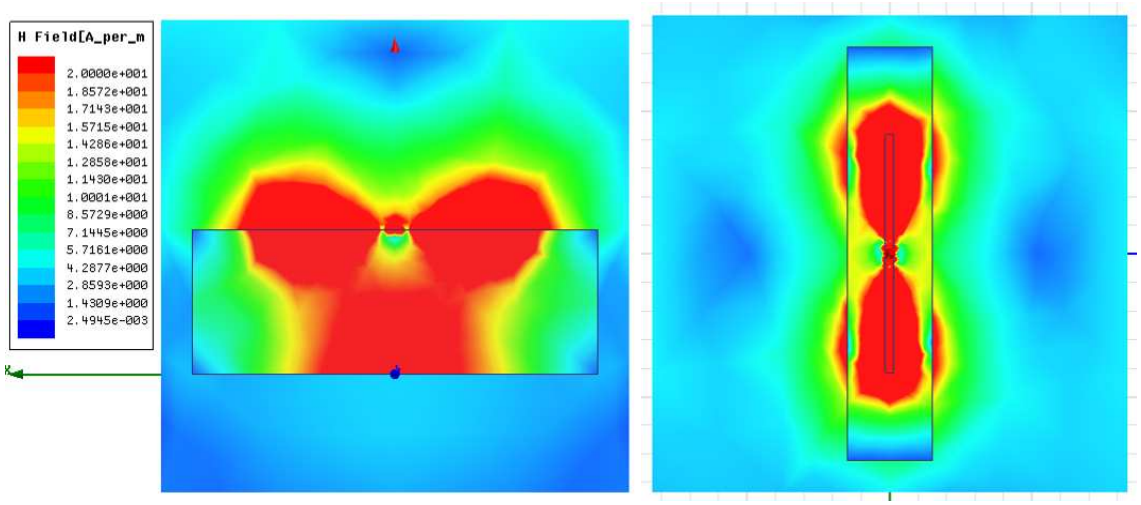

Figure 3.18 Electromagnetic field distribution of slot antenna

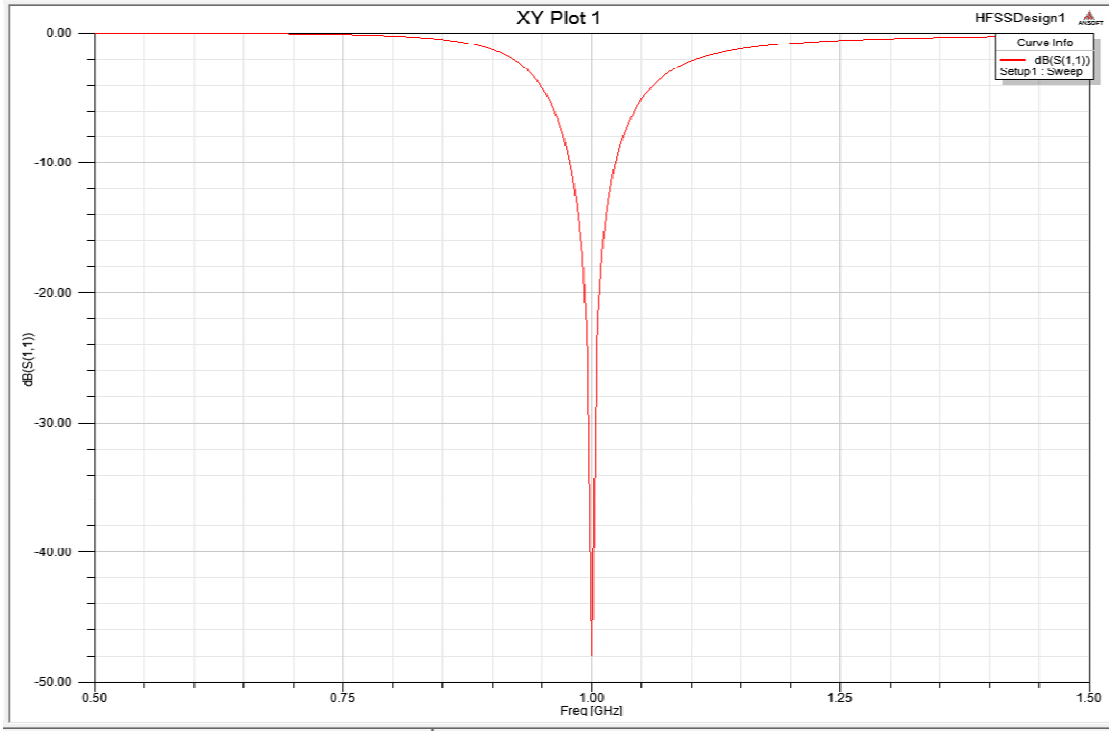

Figure 3.19 S11 of the cavity-backed slot antenna.

The HFSS cavity-backed slot antenna model has a resonance frequency at 1 GHz, which is expected to design for this tool. S11 parameter bellows -40 dB at this frequency, indicating that most of the energy radiated away from the antenna slot shown in Figure 3.19. The electromagnetic field distribution is presented in Figure 3.20.

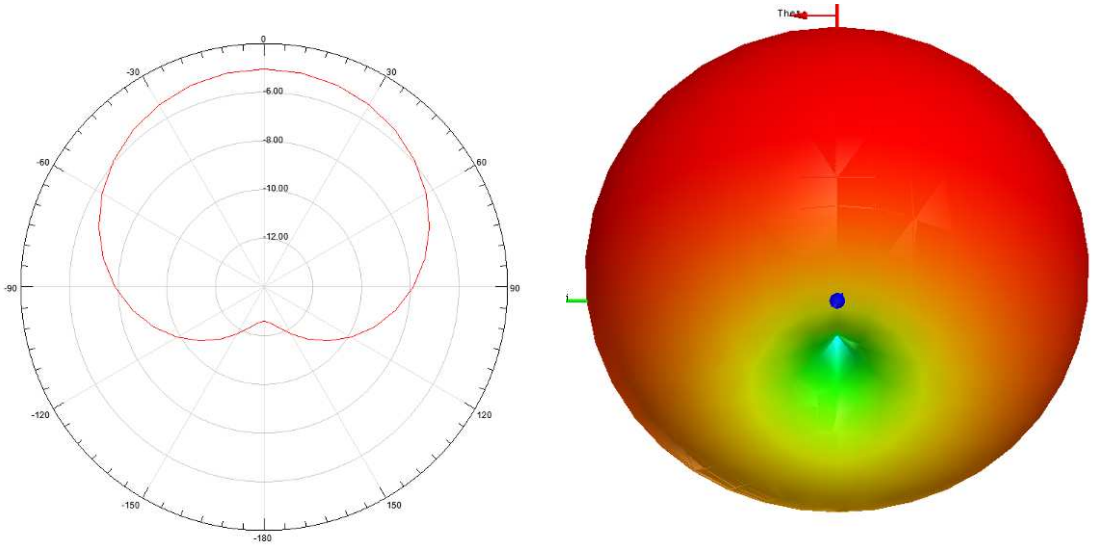

(a) (b)

Figure 3.20 HFSS model results for field distribution (a) and 3D view (b)

3.4.4. Mathematical Model

Long has developed a mathematical model [16] that is used to predict the impedance of the cavity-backed slot antenna as well as its function of frequencies. Certain constants were derived empirically from the experimental data so that the model is not a theory in itself. A mathematical model displays the cavity by a short-circuited transmission line of electrical length $\beta_g Z_0$ in parallel with the open slot. This will be a purely susceptive addition in admittance and will also undoubtedly not remain as the only modification caused by the addition of this cavity. It should be noted that all impedances and admittances are those of an imaged slot antenna and that the actual values for the complete slot will differ by a factor of two, which $Z_{S/2} = Z_S / 2$ and $Y_{S/2} = 2\, Y_S$. For $Y_{S/2} = 1/Z_{S/2}$ and $Y_2 = 1/Z_2$, let

$$Y_{S/2} - Y_2 / 2 = Y_D = Y_{DR} + jY_{DI}, \tag{146}$$

where Y_D is the difference between the two admittances and is a function of the cavity depth Z_0, the width a and height b of the cavity, and the frequency in MHz, f_{MHz}. Let

$$Y_{DI} = -Y_{IO}\, cot\, \beta_g Z_0 + Y_{IF}, \tag{147}$$

$$Y_D = Y_{DR} + j\left(Y_{IF} - Y_{IO}\, cot\, \beta_g Z_0\right), \tag{148}$$

and

$$Y_{IF} = 0.00133\, f_{MHz} - 0.84, \tag{149}$$

$$Y_{IO} = 0.007\, f_{MHz} - 0.205, \tag{150}$$

where f_{MHz} is the frequency in MHz and the normalized admittances are unitless.

The experimental admittance of slot antenna Y_2 is a function of frequency, which is of great use in that a computer, could then plot continuous curves for the impedances as a function of cavity depth or frequency. The HFSS model then again is used to compare the impedance predicted by the mathematical model. The imaginary part of impedance is relatively linear, as the real part seems to be an exponential function of frequency, which

$$Y_{2I} = 0.00401\, f_{MHz} - 2.273, \tag{151}$$

$$Y_{2R} = 0.00913 \exp(0.00554\, f_{MHz}). \tag{152}$$

These approximate functions for Y_{2I} and Y_{2R} fit well over the frequency range of interest. These continuous functions are then inverted to give smooth curves for the real and imaginary parts of the impedances Z_{2R} and Z_{2I}. The agreement is quite good.

3.4.5. Babinet's Principle

To gain an intuition about slot antennas, we first have to know Babinet's principle, which states that when the field behind a screen with an opening is added to the field of a complementary structure, the sum is equal to the field when there is no screen.

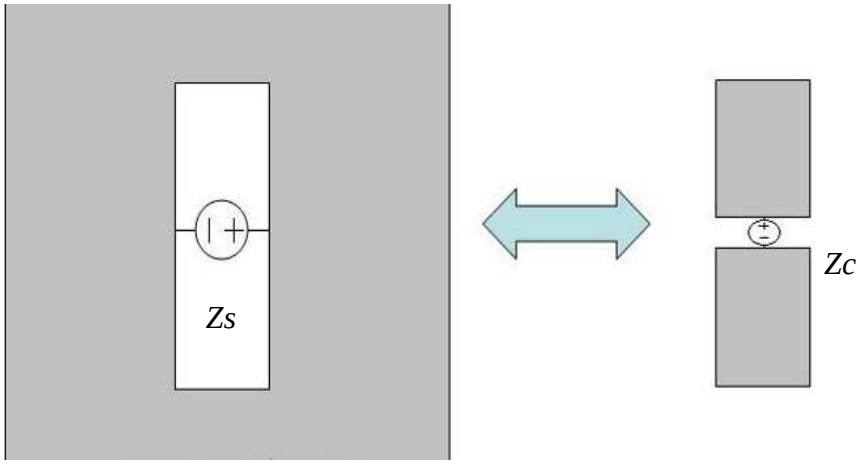

Figure 3.21 Opening on a screen and its complementary dipole

The electric screen with the opening in Figure 3.21 (left) and the electric conductor (right) are dual. They are usually referred to as complementary structures, because when combined they form a single solid screen with no overlaps. Note that a voltage source is applied across the short end of the slot antenna. This induces an E-field distribution within the slot, and currents that

travel around the slot perimeter, both contributed to radiation. The dual antenna is similar to a dipole antenna. The impedance of the slot antenna (*Zs*) is related to the impedance of its dual antenna (*Zc*) by the relation,

$$Z_S \, Z_C = \frac{\eta^2}{4}, \tag{153}$$

where η is the intrinsic impedance of free space.

In addition, the far-zone fields radiated by the opening on the screen $\left(E_{\theta S}, E_{\phi S}, H_{\theta S}, H_{\phi S}\right)$ are related to the far-zone fields of the complement $\left(E_{\theta C}, E_{\phi \mathrm{C}}, H_{\theta C}, H_{\phi \mathrm{C}}\right)$ by

$$E_{\theta S} = H_{\theta C}, \qquad E_{\phi S} = H_{\phi \mathrm{C}}, \qquad H_{\theta S} = -\frac{E_{\phi \mathrm{C}}}{\eta_0^2}, \qquad H_{\phi S} = -\frac{E_{\theta C}}{\eta_0^2}. \tag{154}$$

The impedance properties of the slot may not be affected as much by the finite dimensions of the plane as would be its pattern. Unidirectional radiation can be obtained by placing a backing (box or cavity) behind the slot, forming a so-called cavity-backed slot whose radiation properties (impedance and pattern) are determined by the dimensions of the cavity.

Chapter 4 Results and Data Interpretation

In this chapter, the simulation results of dielectric constant tool responses in the infinitesimal dipole model and HFSS model are presented. First, the impedances of cavity-backed slot antenna are measured and compared with Long's experimental data. The amplitude ratios and phase shifts of EPT in homogeneous formation are measured by using our dipole model and are then verified by the HFSS model and Wellog LWD code, which has been rigorously tested for measuring logging tools responses. Then, the numerical results of EPT in inhomogeneous isotropic layered formation are shown and studied in 28 different cases with a combination of formation and mud cake parameters. Finally, the preliminary study of the dielectric scanner in four different polarizations LT - LR, LT - TR, TT - LR, and TT - TR are presented as follows.

4.1. Impedance of Cavity-Backed Slot Antenna

In the experimental study of the impedance of the cavity-backed slot antenna [15], an investigation was made of the impedance of the cavity-backed slot antenna. The data was taken as a function of cavity depth and frequency for several different cavity backings of the same slot antenna. The principal area of interest was near the depth corresponding to resonance in the cavity; this should be in the vicinity of a quarter guide wavelength ($z_0 = \lambda_g / 4$). The cutoff and guide

wavelengths of the TE_{nm} and TM_{nm} modes for rectangular waveguide of width a and height b are [22]

$$\lambda_{\mathrm{cnm}} = \frac{2\,a\,b}{\sqrt{(\mathrm{n}^2 b^2 + \mathrm{m}^2 a^2)}}, \tag{155}$$

$$\lambda_{\mathrm{gnm}} = \frac{\lambda}{\sqrt{(1-[(\mathrm{n}\lambda/2a)^2 + (\mathrm{m}\lambda/2b)^2])}}, \tag{156}$$

where λ is the free space wavelength, a is the cavity length, and b is the cavity width shown in Figure 4.1. For the dominant TE_{10} mode, the cutoff wavelength is $\lambda_{c10} = 2\,a$. In the particular case of this cavity, a = 15 cm and b = 6 cm. For the desired center frequency of 1 GHz, the free space wavelength $\lambda_0 = 30cm$ and the waveguide is exactly at the point of cutoff, $\lambda_0 = \lambda_{c10} = 30cm$. It is desirable to have the dominant mode and no other capabilities of propagation. Since the length of the slot is to remain at 15 cm ($\lambda/2$ in free space), and the cavity is to have the same physical cross section, it is necessary to change the electrical wavelength inside the cavity by introducing a suitable dielectric material. For the introduction of a dielectric with a relative dielectric constant ε_r, this results in a new guide wavelength for the dominant TE_{10} mode,

$$\lambda_{\mathrm{g10}} = \frac{2\,a\,\lambda_0}{\sqrt{(4\,a^2\varepsilon_r - {\lambda_0}^2)}}. \tag{157}$$

In order to increase dimension a, both a cutoff frequency and guide wavelength should be decreased, yet must still remain small enough to cover the range of frequencies allowing the cavity depth to vary over nearly a half guide

wavelength. In order to compare the impedance of the slot antenna of the HFSS model with experimental results [15], the size of HFSS model was adjusted to a = 35 cm with a guide wavelength at 600 MHz of $\lambda_g = 71.44\,\mathrm{cm}$ and the height of b = 10 cm. This makes the height of the cavity 10 times the width of the slot that corresponds to the range of ratios of many practical cavity-backed slots.

The impedance of slot antenna was plotted with $\lambda_g/16$ increments (λ_g calculated at 600 MHz, which is used in Long's experimental study). The impedance as a function of frequency was then measured for each cavity depth and is shown in Figure 4.2 and 4.3. The position of the resonance and the peak resistance vary quite smoothly as a function of the parameter Z_0, the cavity depth.

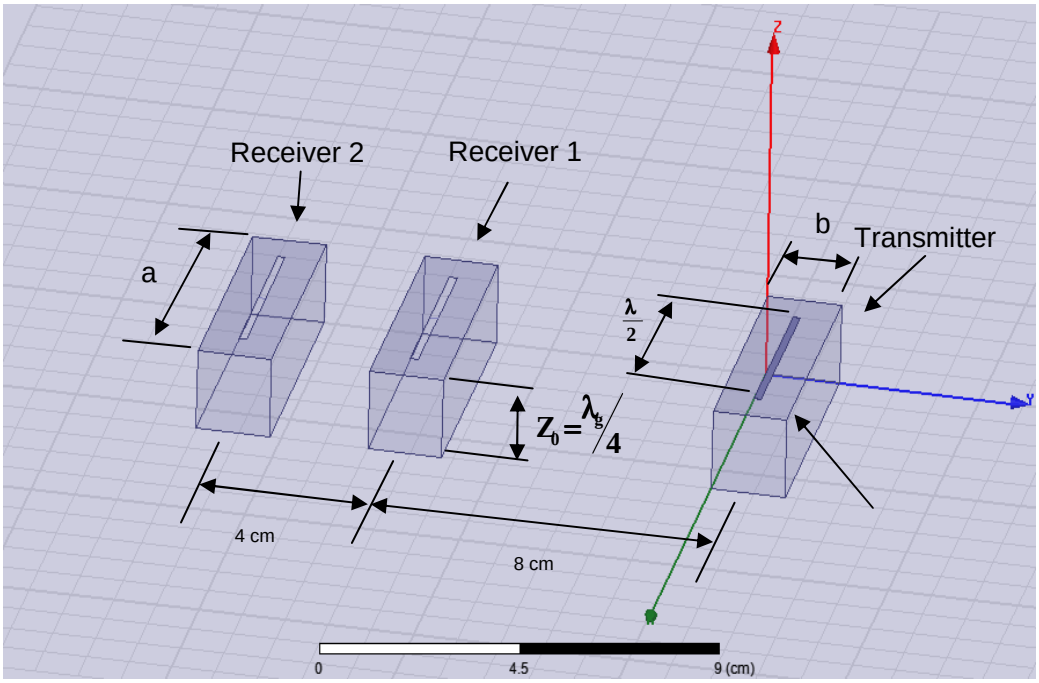

Figure 4.1 HFSS model of cavity-backed slot antenna

Figure 4.2 and 4.3 illustrate resistance and reactance measured in a cavity-backed slot antenna where each curve has $\lambda_g/16$ increments respectively. The peak values of experimental results are half of the HFSS model results; this is because the experimental cavity was designed using imaging techniques where a slot of one-half the desired width is cut in the edge of a ground plane where this edge is then butted up against a highly conducting imaging plane. The image plane thus bisects the slot lengthwise and is perpendicular to the plane of the slot. The HFSS model results have a good agreement compared to the experimental results. The peak values of the HFSS model have, then, been divided by two in comparison with the experimental results.

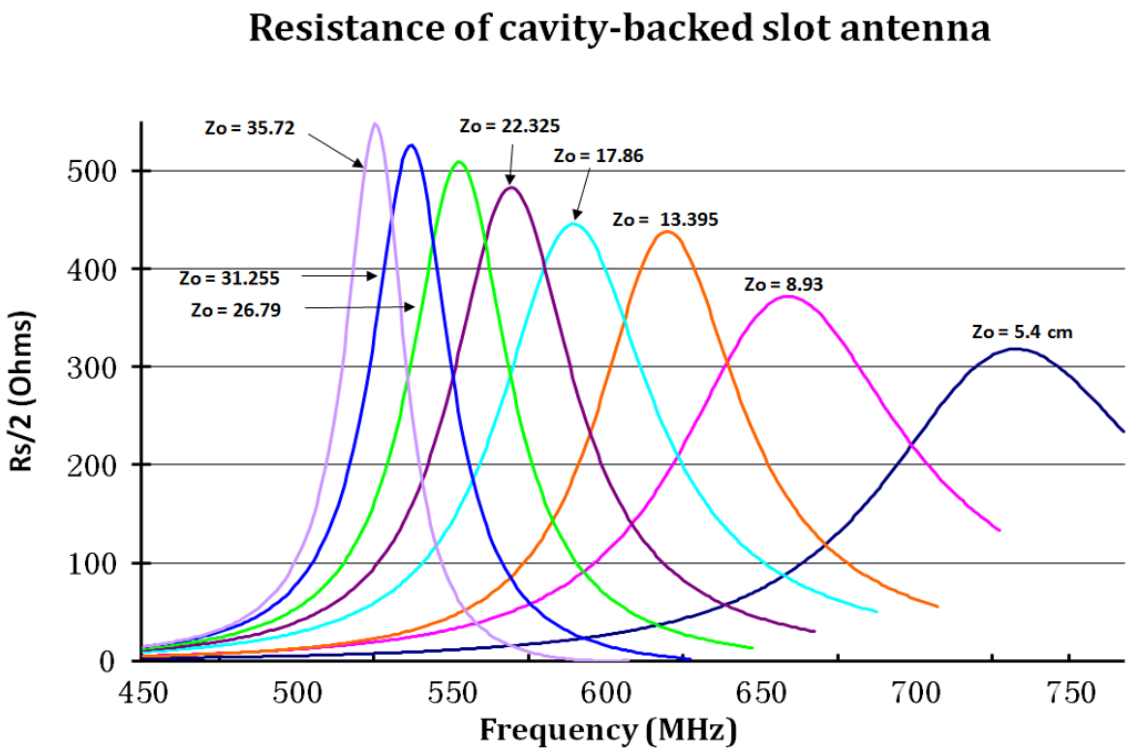

(a) HFSS Model Results

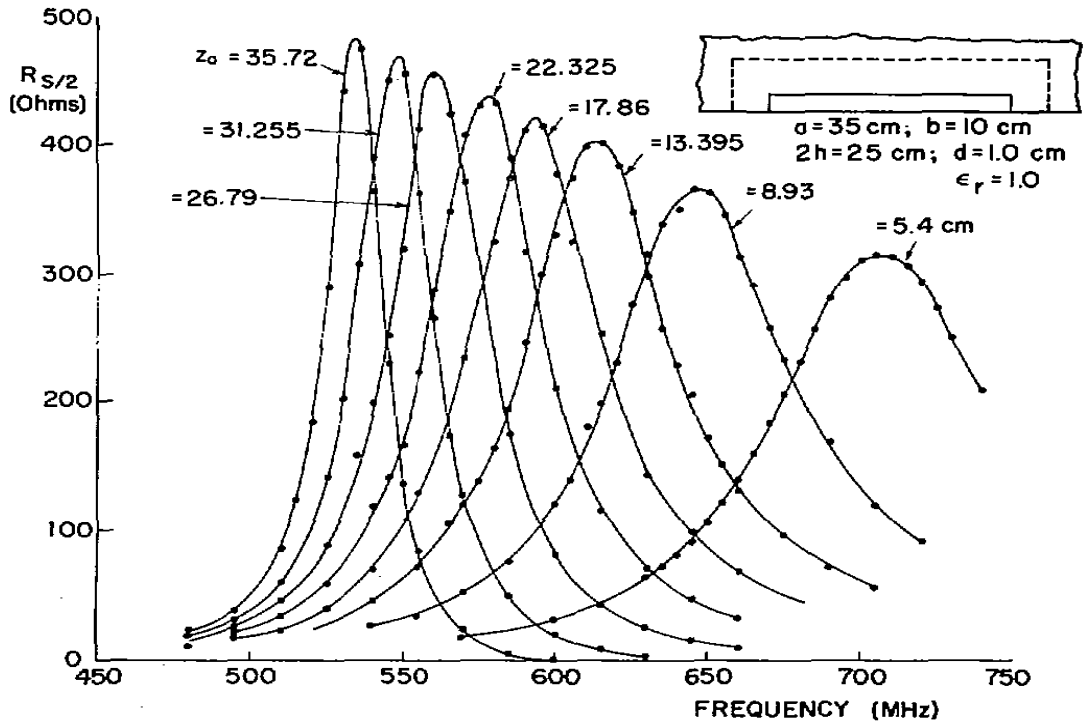

(b) Experimental Results

Figure 4.2 Resistance of cavity-backed slot antenna

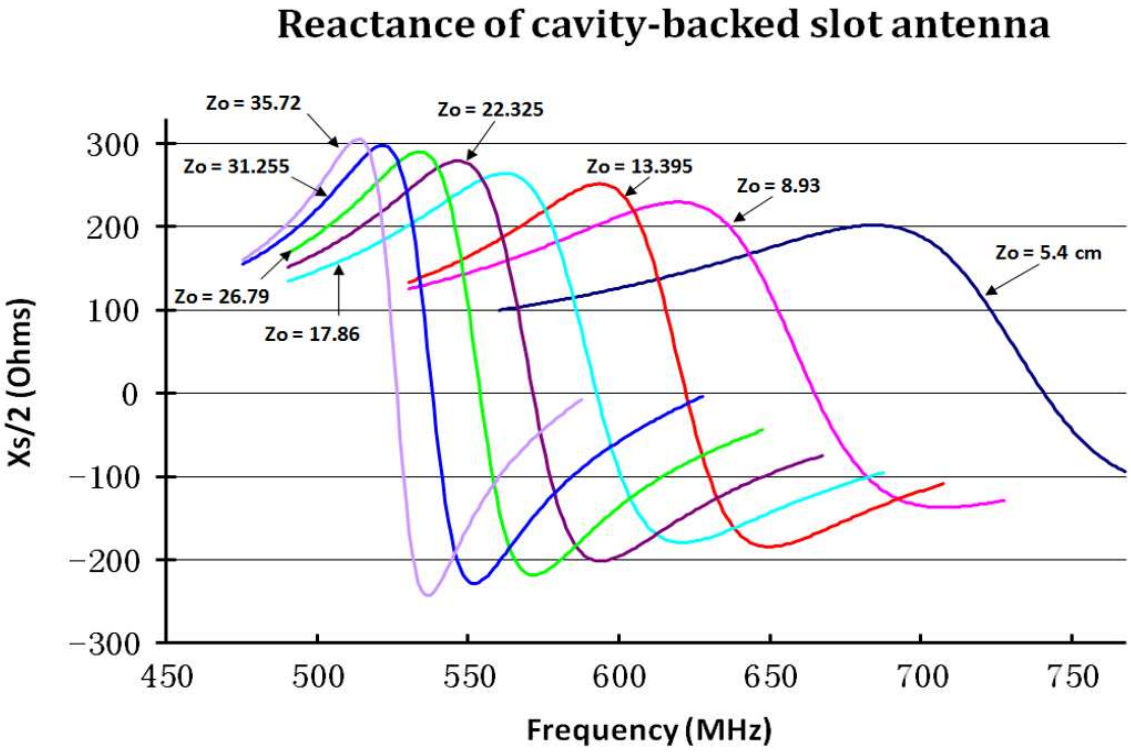

(a) HFSS Model Results

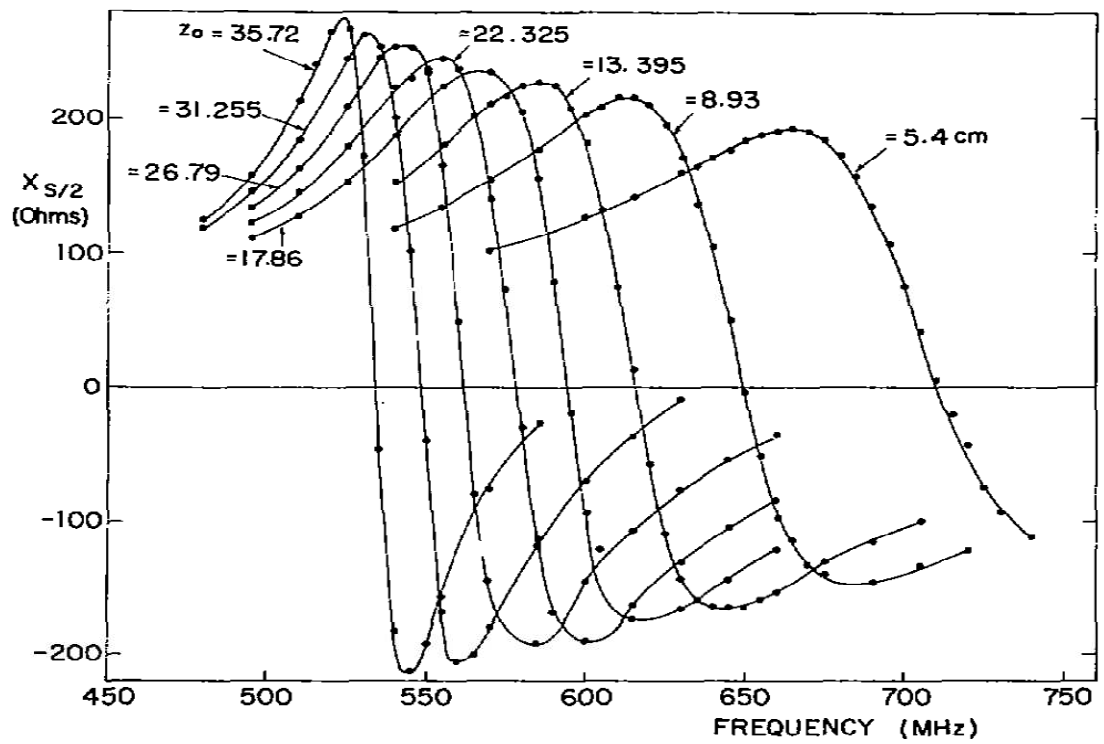

(b) Experimental Results

Figure 4.3 Reactance of cavity-backed slot antenna

The impedances shown in Figure 4.2 and 4.3 have very good agreement to Long's experimental results. With $z_0 = \lambda_g / 4$ in cavity depth, the reactance has its interception at 0 and the resistance at the peak value. This means that we can use the HFSS aperture model to produce the correct measurements for the EPT tool.

Figure 4.4 is the HFSS model simulation result of the impedance of the slot antenna in $z_0 = \lambda_g / 4$ with a resonance frequency of 1 GHz, which has shown the S11 parameter at Figure 3.19.

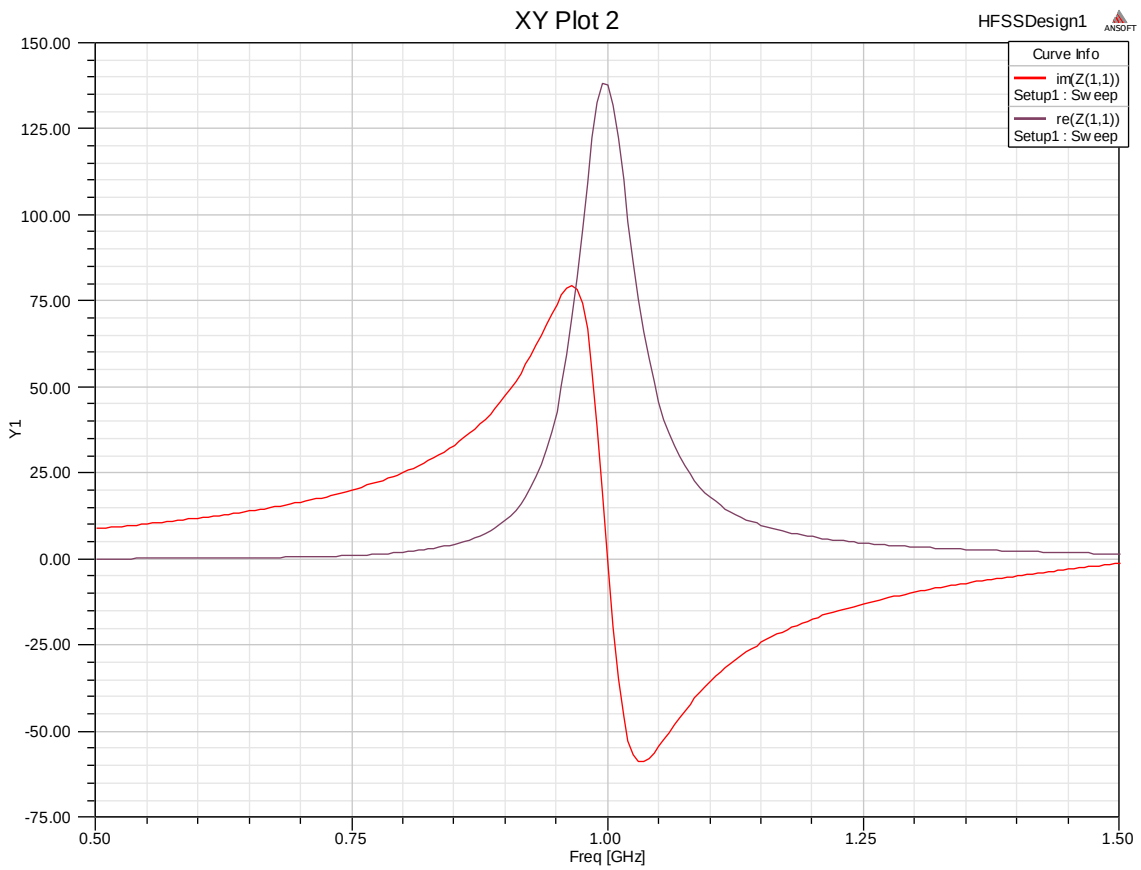

Figure 4.4 The impedance of HFSS model at 1 GHz

Figure 4.5 and 4.6 show the resistance and reactance of the slot antenna at a frequency of 1 GHz. We may also plot the impedance with $\lambda_g/16$ increments for each curve, $\mathrm{Zo} = \lambda_g/8$, $\lambda_g * 3/16$, $\lambda_g/4$, $\lambda_g * 5/16$, and $\lambda_g * 6/16$. The peak value at $Zo = \lambda_g/4$ of resistance in Figure 4.6 has only about Rs = 138 ohms, which is significantly smaller with Figure 4.2 which has a peak value at about Rs = 900 ohms. This is due to the size of the slot of the antenna which is considerably smaller at a high frequency operation with the dielectric constant material added into the cavity. The cavity depth Z_0 at a frequency of 1 GHz is only 1.02 cm and the Z_0 at frequency of 600 MHz is about 17. 86 cm.

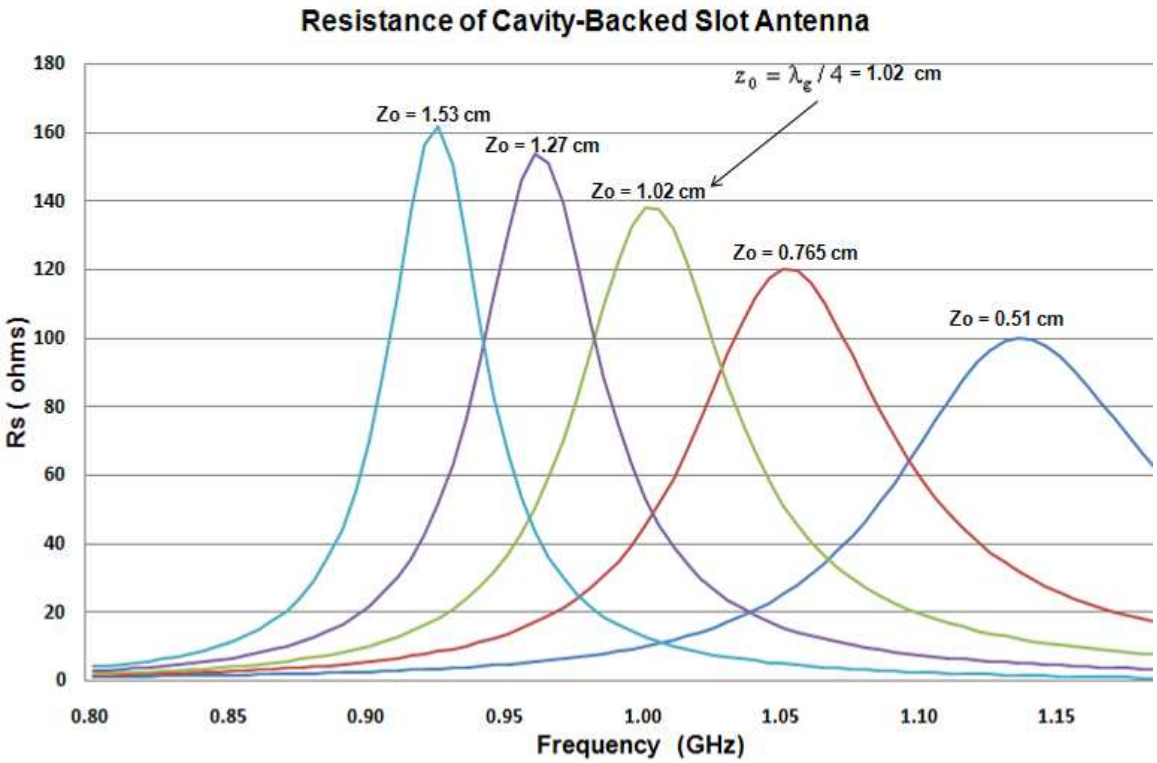

Figure 4.5 The resistance of cavity-backed slot antenna at 1 GHz

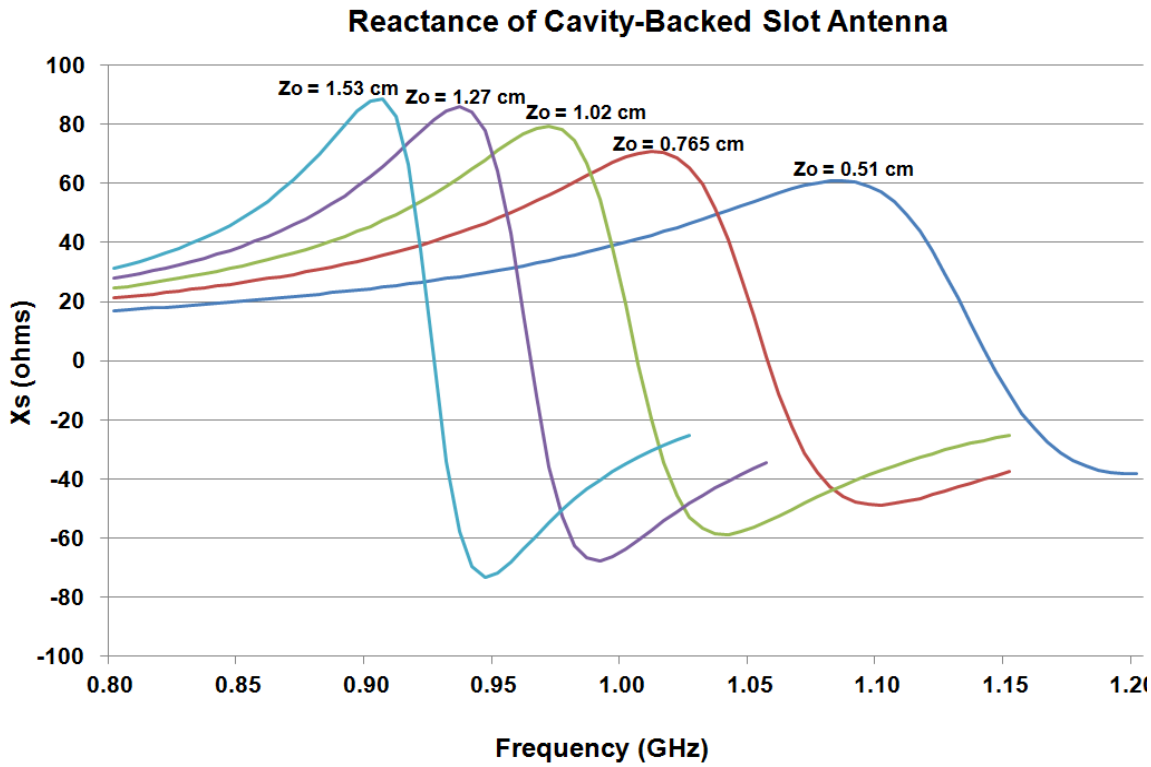

Figure 4.6 The reactance of cavity-backed slot antenna at 1 GHz

4.2. EPT Tool Response

As we know, the electromagnetic wave propagation method of dielectric constant logging attempts to deduce the dielectric properties of earth formation from the phase shift and attenuation measurement of the electromagnetic fields, which have been propagated in the formation. This section will present the amplitude ratio and phase shift measurements of the Electromagnetic Propagation Tool (EPT) in homogeneous and layered formation. The comparison of experimental and theoretical study of the EPT in layered and homogeneous media [23] is also present in this section.

4.2.1. AR and PS in Homogeneous Formation

This section will present the amplitude ratio and phase difference of the Electromagnetic Propagation Tool (EPT) measured in homogeneous formation without mud cake presented using three different methods: the LWD code, the infinitesimal dipole model, and the HFSS simulation model. In this case, we have measured the tool responses with different dielectric permittivity and conductivity in frequency of 1 GHz, 500 MHz, and 100 MHz. In Figure 4.7 and 4.8 are the amplitude ratio and the phase shift at a frequency of 1 GHz where each curve of sigma = 0, 0.01 and 0.1. At the microwave frequency, the measurement was dominated by the dielectric constant of the earth formation. With a small value of

the dielectric constant, we can assume that the conductivity of the earth formation affected the measurement. As the dielectric constant increases, the outcome of the conductivity can be negligence.

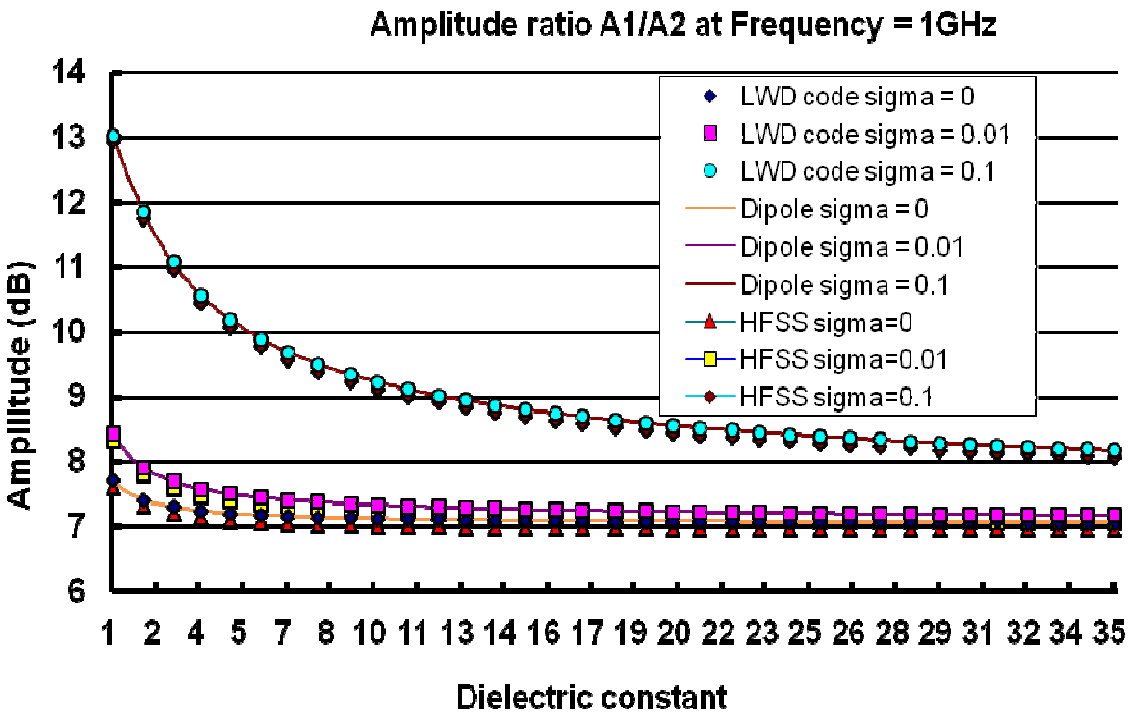

Figure 4.7 Amplitude Ratio at 1 GHz

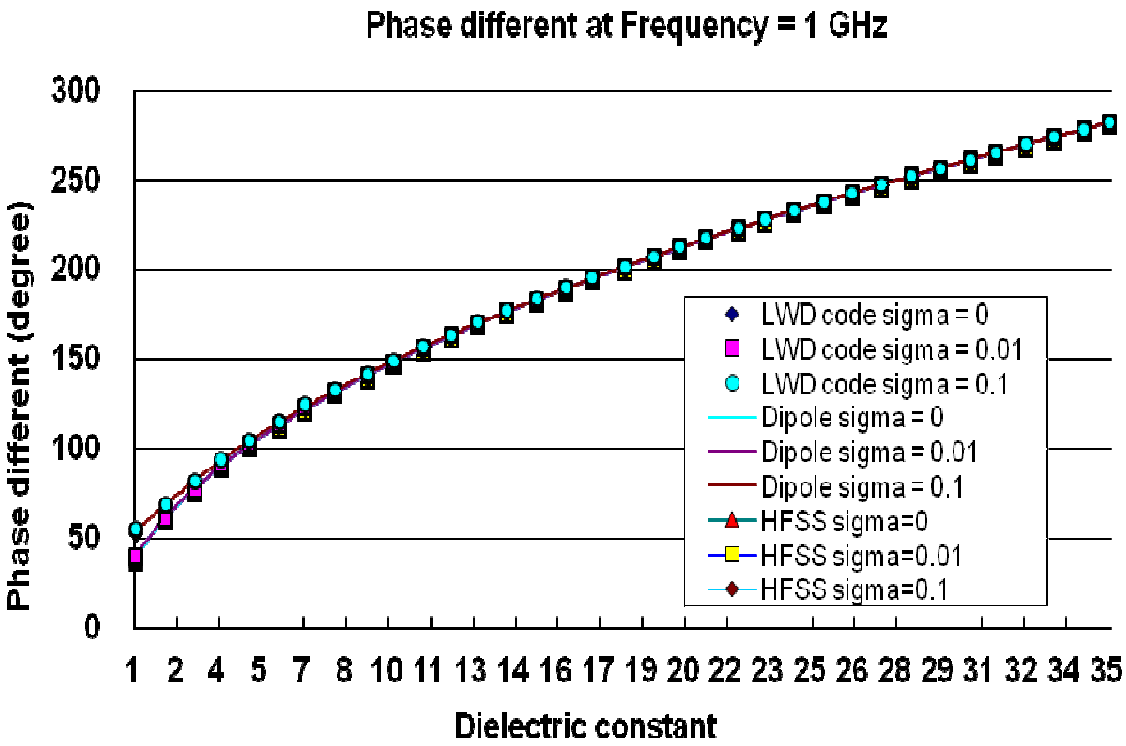

Figure 4.8 Phase Shift at 1 GHz

As we have mentioned that the dielectric constant logging tool at microwave frequency is relatively independnent of water salinity; this can be clearly shown in Figure 4.8 that the phase shift for the difference value of sigma provides the same measurement results. This is true as long as the operation frequency is within the microwave range.

The measurements of the tool responses at a frequency of 500 MHz and 100 MHz are shown in Figure 4.9 to 4.12. The amplitude ratios and phase differences at 500 MHz have almost the same behaviors as the1 GHz because it is within the microwave frequency range. However, when the operation frequency is below the microwave frequency such as 100 MHz, the effects of conductivity appeared soon after. The results also confirm that the amplitude ratios and

phase shifts increased as the conductivity of the earth formation increased. These three methods have made a successful agreement.

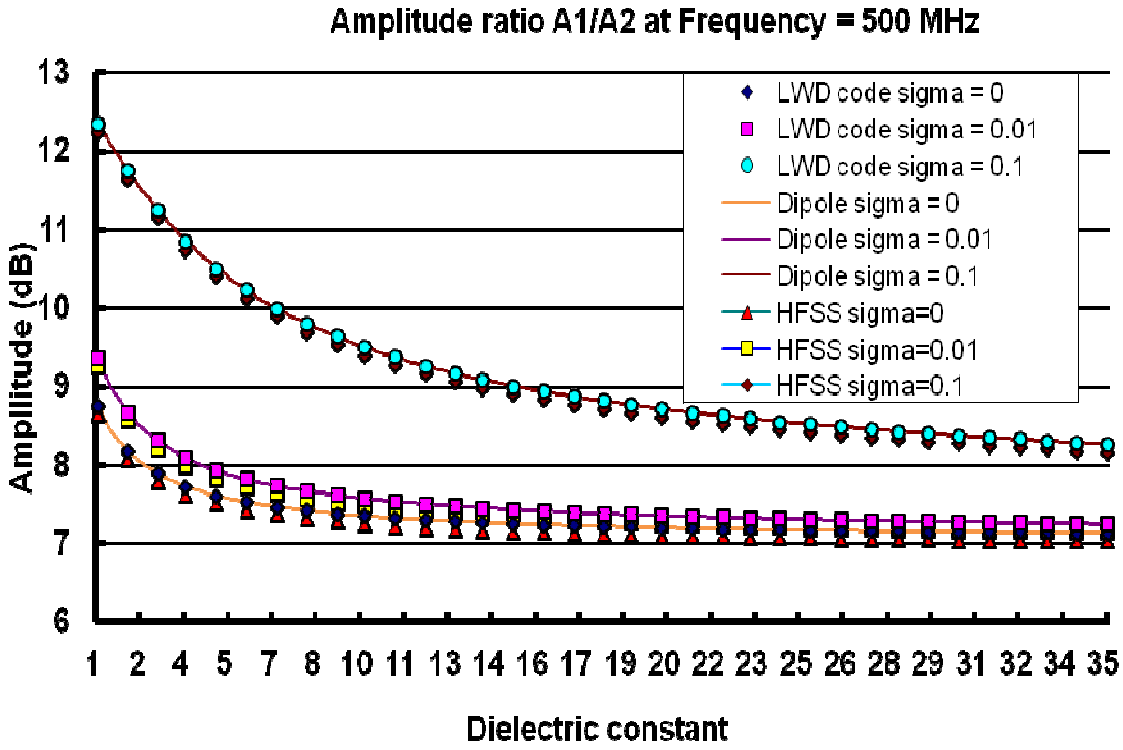

Figure 4.9 Amplitude Ratios at 500 MHz

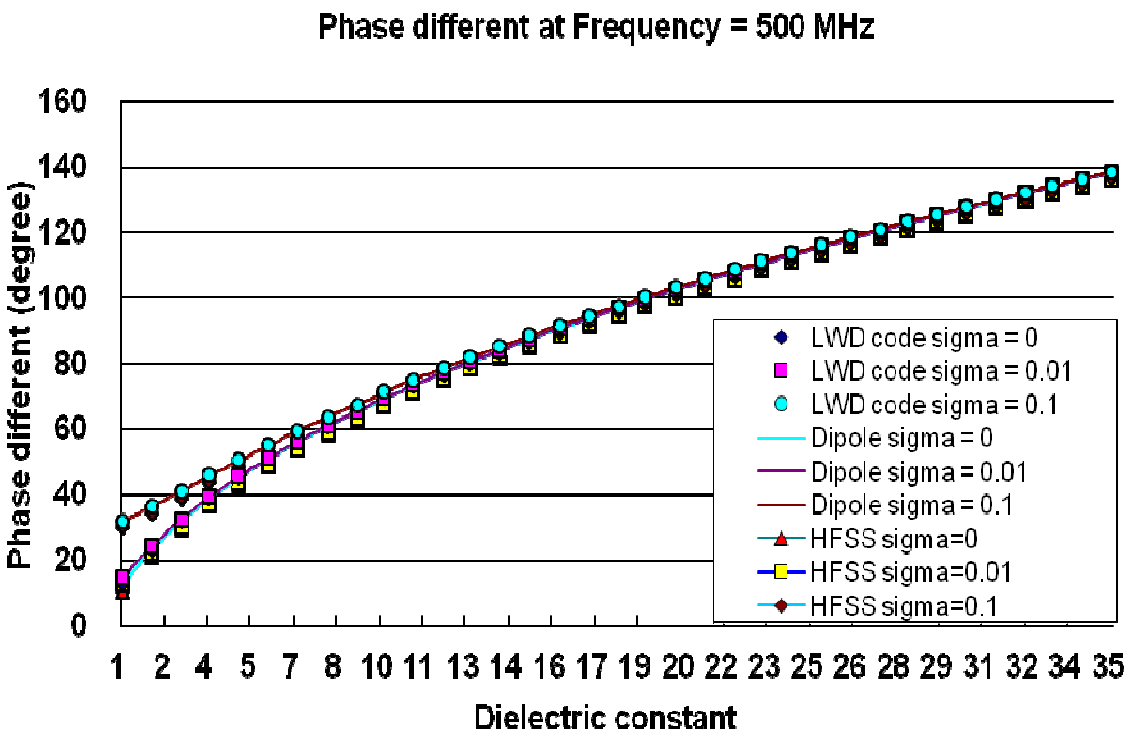

Figure 4.10 Phase Shifts at 500 MHz

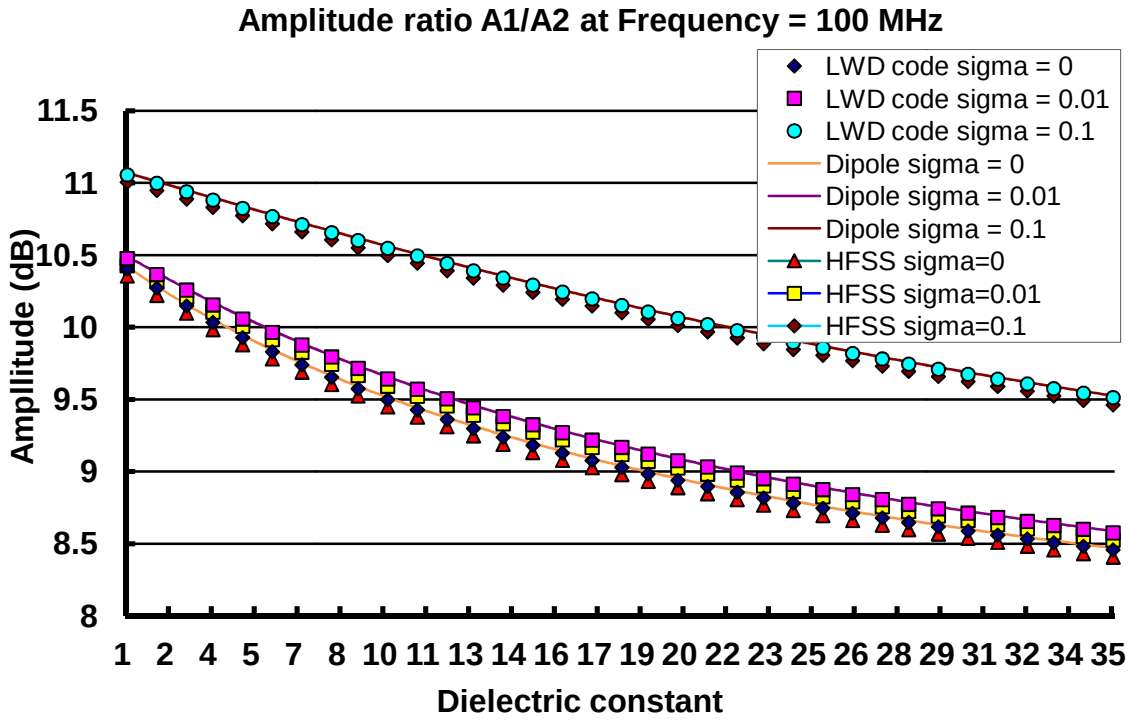

Figure 4.11 Amplitude Ratios at 500 MHz

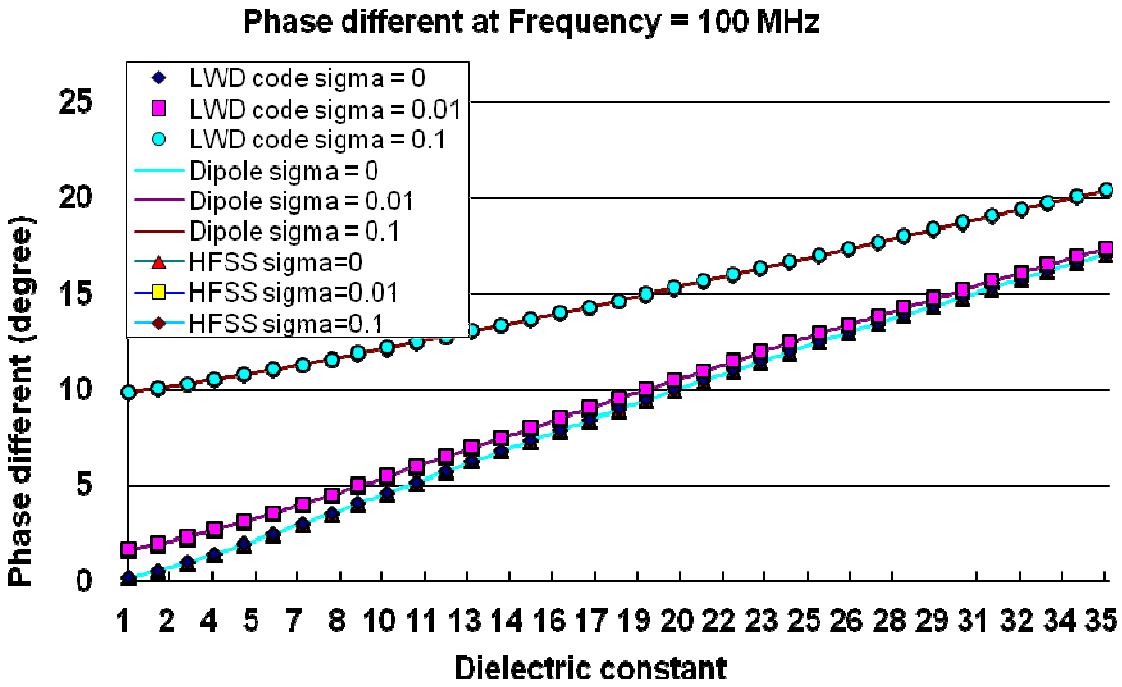

Figure 4.12 Phase Shifts at 500 MHz

4.2.2. Wave Propagation in Homogeneous Media

Table 4.1 shows the experimental and theoretical results pertaining to the various liquids that were used as a homogeneous media. The table lists the true dielectric properties of each medium, the attenuation (α), and the phase shift (S), measured with the EPT as well as the values calculated with the different models. The model with the red line circle is our infinitesimal dipole model that when compared with the other two magnetic-line currents and plane-wave models presented in [23] indicates that the true dielectric constants and the conductivities of the various media are known with an accuracy of around 1%. The uncertainties in the dielectric constants and conductivities bring about errors into the calculated

attenuation of about 1.5% and into the calculated phase shift of about 0.5%. The experimental uncertainty in the measured attenuation is about 0.1 dB, and the experimental uncertainty in the measured phase shift is about 1°.

Table 4.1 Results of Wave Propagation in Homogeneous Media

			Experiment		Dipole Model		Error	
Medium	ε'	σ	α (dB)	S (degree)	α (dB)	S (degree)	α (dB)	S (degree)
Water	75.7	2.78	-28.6	463	-27.2	477	1.4	3.02%
Water	78.1	1.28	-18.4	457	-16.5	470	1.9	2.84%
Water	78.8	0.48	-13.3	459	-10.6	468	2.7	1.96%
Water	79.1	0.32	-12.4	459	-9.4	469	3	2.18%
Ethylene gycol	26.8	0.99	-20.1	279	-19.2	283	0.9	1.43%

Magnetic -Line Current		Error	
α (dB)	S (degree)	α (dB)	S (degree)
-20.8	460	7.8	0.65%
-10.6	450	7.8	1.53%
-5	449	8.3	2.18%
-3.9	449	8.5	2.18%
-13.1	373	7	33.69%

Plane-Wave Model		Error	
α (dB)	S (degree)	α (dB)	S (degree)
-19.2	456	9.4	1.51%
-9	449	9.4	1.75%
-3.4	448	9.9	2.40%
-2.2	448	10.2	2.40%
-11.5	271	8.6	2.87%

Results show that our infinitesimal dipole model gives exceptionally good results for the attenuation, with the discrepancies at about 3 dB or less for the water cases and about 0.9 dB for the ethylene glycol. The magnetic-line current model has discrepancies of about 8.5 dB or less for water cases and 7 dB for ethylene glycol. The plane-wave model, which gives the worst prediction, has discrepancies at about 10.2 dB or less for water cases and around 8.6 dB for

ethylene glycol. The plane-wave model has no geometric spreading, so the predicted attenuation depends only on the medium's properties. Thus, it predicts the least amount of attenuation. The magnetic-wave model allows the wave to spread in two dimensions, therefore, it predicts more attenuation than the plane-wave model. Moreover, our dipole model allows the wave to spread into three dimensions, hence increasing the spreading loss as well as providing a good expectation.

All three models distribute accurate phase shift measurements. Our dipole model has an average difference of about 3.02% or less for water cases and 1.43% for ethylene glycol. The magnetic-line current model has about 2% or less for water cases and 2.51% for ethylene glycol. The plane-wave model gives about 2.4% or less for water cases and 2.87% for ethylene glycol. The overall phase shift predictions were all within expectation.

4.2.3. Numerical results in layered Media

In this section the numerical results in inhomogeneous isotropic layered formation both with and without mud cake presented the use of the infinitesimal dipole model, which has been introduced in section 3.1.7. The calculation results in comparison to the data in [24].

Freedman [24] introduced two travel times t_{pl} and t_{po}, which are defined in terms of α and β from the complex propagation constant k given as

$$k = \alpha + i\beta = \frac{2\pi}{\lambda_0}\sqrt{K_{1,2}\left(1 + i\,tan\,\delta_{1,2}\right)}, \tag{158}$$

where $K_{1,2}$ is the relative permittivity of the mud cake and the formation respectively. The t_{pl} and t_{po} are defined by the equation

$$t_{pl} = \alpha/\omega, \tag{159}$$

and

$$t_{po} = \sqrt{u_0\varepsilon'} = \frac{\sqrt{\alpha^2 - \beta^2}}{\omega}. \tag{160}$$

The t_{pl} and t_{po} are considered to be true values of the EM properties of a medium. The results that are calculated based on our dipole model are considered to be the observed values of t_{plc} and t_{poc}, which are defined as

$$t_{plc} = \alpha_c/\omega \equiv \frac{\Delta\phi}{L\,\omega}, \tag{161}$$

and

$$t_{poc} = \sqrt{\mu_0\varepsilon'_c} \equiv \frac{\sqrt{\alpha_c^2 - \beta_c^2}}{\omega}, \tag{162}$$

where the $\Delta\phi$ is the phase shift in degrees and L is the distance between the receivers. We will compare the observed values from our dipole model to the true values that were calculated from (159) and (160).

From the boundary condition, the only nonvanishing component of the electric field at the receivers is the z-component, which is given by equation [24]

$$E(r) = 2R' \int_0^{\infty} \frac{d\lambda\, \lambda^3\, J_0(\lambda r)\, e^{i r_1 d}\, (\gamma_1 k_2^2 - \gamma_2 k_1^2)}{\gamma_1 \left[\gamma_2 k_1^2 \left(e^{i\gamma_1 d} + e^{-i\gamma_1 d}\right) - \gamma_1 k_2^2 \left(e^{i\gamma_1 d} - e^{i\lambda d} - e^{-i\gamma_1 d}\right)\right]} + \frac{i R' e^{i k_1 r}}{r^3}\left[1 - ik_1 r - (k_1 r)^2\right] \quad (163)$$

The electric fields at the receivers located at $R_{1,2}$ are given at $r = x_{1,2}$ for l = 1, 2. The numerical calculations were performed as values of the formation parameters K_2 = 5.0, 10.0, 15.0, 20.0, and 25.0; and tan δ_2 = 0.10, 0.30, 0.40, and 0.60. The parameters of mud cake are K_1= 25, 35, 40; tan δ_1 = 1.0, 3.0, 5.0; and d = 1.0, 0.5, 0.3, and 0 cm. The Table 4.2 lists the formation parameters and 28 cases of the combination parameters for calculations.

Table 4.2 Formation parameters and 28 cases of mud cake parameters

K_2	$\tan\delta_2$	Sigma
5.0	0.1	0.030556
10.0	0.1	0.061111
15.0	0.1	0.091667
20.0	0.1	0.122222
25.0	0.1	0.152778
5.0	0.3	0.091667
10.0	0.3	0.183333
15.0	0.3	0.275
20.0	0.3	0.366667
25.0	0.3	0.458333
5.0	0.4	0.122222
10.0	0.4	0.244444
15.0	0.4	0.366667
20.0	0.4	0.488889
25.0	0.4	0.611111
5.0	0.6	0.183333
10.0	0.6	0.366667
15.0	0.6	0.55
20.0	0.6	0.733333
25.0	0.6	0.916667

Case	K_1	$\tan\delta_1$	d		Sigma
			(cm)	(feet)	
1	25.0	1.0	0	0	0
2	25.0	1.0	0.3	0.563963	1.527777778
3			0.5	0.939939	1.527777778
4			1	1.879878	1.527777778
5	25.0	3.0	0.3	0.563963	4.583333333
6			0.5	0.939939	4.583333333
7			1	1.879878	4.583333333
8	25.0	5.0	0.3	0.563963	7.638888889
9			0.5	0.939939	7.638888889
10			1	1.879878	7.638888889
11	35.0	1.0	0.3	0.563963	2.138888889
12			0.5	0.939939	2.138888889
13			1	1.879878	2.138888889
14	35.0	3.0	0.3	0.563963	6.416666667
15			0.5	0.939939	6.416666667
16			1	1.879878	6.416666667
17	35.0	5.0	0.3	0.563963	10.69444444
18			0.5	0.939939	10.69444444
19			1	1.879878	10.69444444
20	40.0	1.0	0.3	0.563963	2.444444444
21			0.5	0.939939	2.444444444
22			1	1.879878	2.444444444
23	40.0	3.0	0.3	0.563963	7.333333333
24			0.5	0.939939	7.333333333
25			1	1.879878	7.333333333
26	40.0	5.0	0.3	0.563963	12.22222222
27			0.5	0.939939	12.22222222
28			1	1.879878	12.22222222

The Table 4.3 shows the numerical results of homogeneous formation and the layered formation without mud cake present. The results were similar to one another meaning the measurements were truly represented in the formation properties other than in the borehole drilling mud. The observed values t_{plc} and t_{poc} will then compare to the true value t_{pl} and t_{po}.

Table 4.3 The numerical results without mud cake presented

Case 1 Mud cake thickness d = 0 cm						Special Case for homogeneous formation					
K_2	$\tan\delta_2$	$\Delta\phi$ (degree)	A (dB/m)	t_{plc} (nsec/m)	t_{poc} (nsec/m)	K_2	$\tan\delta_2$	$\Delta\phi$ (degree)	A (dB/m)	t_{plc} (nsec/m)	t_{poc} (nsec/m)
5.0	0.1	113.8	157.9	7.18	7.05	5.0	0.1	113.9	154.1	7.19	7.07
10.0	0.1	165.1	161.7	10.42	10.32	10.0	0.1	164.1	161.5	10.36	10.26
15.0	0.1	202.6	171.2	12.79	12.69	15.0	0.1	202.3	167.9	12.77	12.68
20.0	0.1	235.7	177.9	14.88	14.78	20.0	0.1	234.3	173.6	14.79	14.70
25.0	0.1	263.6	169.0	16.64	16.57	25.0	0.1	262.5	178.6	16.57	16.48
5.0	0.3	115.3	199.4	7.28	6.99	5.0	0.3	115.3	199.3	7.28	6.99
10.0	0.3	165.9	224.8	10.48	10.18	10.0	0.3	165.9	224.7	10.47	10.18
15.0	0.3	204.4	245.1	12.90	12.59	15.0	0.3	204.4	245.0	12.90	12.59
20.0	0.3	236.8	262.7	14.95	14.62	20.0	0.3	236.7	262.3	14.94	14.62
25.0	0.3	265.2	278.1	16.74	16.40	25.0	0.3	265.1	277.7	16.74	16.40
5.0	0.4	116.5	221.2	7.35	6.94	5.0	0.4	116.5	221.2	7.35	6.94
10.0	0.4	167.4	255.4	10.57	10.14	10.0	0.4	167.4	255.4	10.57	10.13
15.0	0.4	206.1	282.5	13.01	12.55	15.0	0.4	206.1	282.4	13.01	12.55
20.0	0.4	238.7	305.7	15.07	14.58	20.0	0.4	238.7	305.5	15.07	14.58
25.0	0.4	267.4	326.3	16.88	16.35	25.0	0.4	267.3	325.9	16.88	16.35
5.0	0.6	119.3	263.1	7.53	6.86	5.0	0.6	119.3	263.0	7.53	6.86
10.0	0.6	171.2	314.2	10.81	10.05	10.0	0.6	171.2	314.2	10.81	10.05
15.0	0.6	210.7	354.3	13.30	12.47	15.0	0.6	210.7	354.2	13.30	12.47
20.0	0.6	243.9	388.4	15.40	14.49	20.0	0.6	243.9	388.2	15.40	14.49
25.0	0.6	273.1	418.7	17.24	16.27	25.0	0.6	273.2	418.3	17.24	16.27

Table 4.4 The numerical results of t_{plc} and t_{poc} compare to t_{pl} and t_{po}

Case 4 Mud cake parameters: K_1 = 25, $\tan\delta_1$= 1.00, and d = 1.0 cm											
		Infinitesimal dipole model				Freeman point transmitter and receivers model					
K_2	$\tan\delta_2$	$\Delta\varphi$ (degree)	A (dB/m)	t_{plc} (nsec/m)	t_{poc} (nsec/m)	$\Delta\varphi$ (degree)	A (dB/m)	t_{pl} (nsec/m)	t_{plc} (nsec/m)	t_{po} (nsec/m)	t_{poc} (nsec/m)
5	0.1	120.9	163.9	7.63	7.49	133.0	159.9	7.46	8.40	7.45	8.28
10	0.1	167.9	182.3	10.60	10.45	189.7	177.1	10.55	11.98	10.54	11.86
15	0.1	204.0	195.8	12.88	12.73	227.6	189.1	12.93	14.37	12.91	14.25
20	0.1	234.4	202.6	14.80	14.65	257.3	200.0	14.93	16.24	14.91	16.11
25	0.1	263.2	211.2	16.61	16.46	282.8	210.9	16.69	17.58	16.67	17.71
5	0.3	121.4	229.4	7.66	7.23	134.3	215.7	7.54	8.48	7.45	8.15
10	0.3	169.9	260.8	10.73	10.28	191.4	243.1	10.66	12.08	10.54	11.76
15	0.3	207.3	275.8	13.09	12.66	229.1	262.1	13.05	14.47	12.91	14.13
20	0.3	239.3	285.6	15.11	14.70	258.3	280.5	15.07	16.31	14.91	15.95
25	0.3	267.4	295.5	16.88	16.48	283.2	300.9	16.85	17.88	16.67	17.48
5	0.4	122.1	251.2	7.71	7.13	135.6	242.7	7.60	8.56	7.45	8.10
10	0.4	171.4	290.4	10.82	10.21	193.1	274.6	10.74	12.19	10.54	11.73
15	0.4	209.5	312.1	13.23	12.63	230.8	296.7	13.16	14.57	12.91	14.10
20	0.4	241.9	327.7	15.27	14.68	259.6	318.7	15.19	16.39	14.91	15.88
25	0.4	270.2	342.5	17.06	16.47	283.9	343.8	16.98	17.92	16.67	17.36
5	0.6	124.3	293.0	7.85	6.96	139.6	293.6	7.76	8.81	7.45	8.03
10	0.6	175.3	348.1	11.07	10.09	197.9	333.1	10.97	12.50	10.54	11.74
15	0.6	215.1	382.0	13.58	12.59	235.3	360.7	13.44	14.86	12.91	14.08
20	0.6	248.2	407.3	15.67	14.66	263.2	389.1	15.51	16.62	14.91	15.78
25	0.6	276.6	432.0	17.46	16.42	285.7	422.7	17.35	18.04	16.67	17.09

The Table 4.4 shows the numerical results of the infinitesimal dipole model and the comparison to the results in [24]. In this typical case, the mud cake parameter K_1 is 25, $\tan\delta_1$ is 1.0, and thickness d is 1.0 cm. The phase shift, for the range of parameters considered in this case, varied from 100 – 300 degrees. For fixed values of the mud cake parameters, the phase shift increased rather rapidly with increasing values of K_2 and increased slowly with increasing values of $\tan\delta_2$. Also the results show that the calculated observed values t_{plc} from our infinitesimal dipole model confirm the true values t_{pl} portrays in the table.

Table 4.5 displays the numerical results of cases 2 to 3, where case 1 is shown in Figure 4.3 and case 4 is shown in Figure 4.4. For this set of mud cake parameters *d* = 0, 0.3, 0.5, and 1 cm, the phase shift also increased rapidly with increasing values of K2 and increased slowly with increasing mud cake thickness *d*. The rest of cases, case 5 - 28, are indicated in Appendix A.

From these calculation results of all 28 cases, we have noted that, firstly, without mud cake presented and for the range of formation parameters considered, the relative errors in t_{plc} varied from 0.2 to 3.7 percent shown in the red mark in Figure 4.13. For the case d = 0 cm, the calculated values t_{plc} are always less than the true values t_{pl}, Figure 4.13 shows the error in the observed

values t_{plc} for K_1 = 25 and tanδ_1= 1.00. The error decreased quickly as increasing formation parameter K_2 and slowly as increasing tanδ_2.

Table 4.5 The numerical results for case 2 and 3

Case 2						Case 3					
Mud cake parameters: K_1 = 25, tan δ = 1.00, and d = 0.3 cm						Mud cake parameters: K_1 = 25, tan δ_1= 1.00, and d = 0.5 cm					
K_2	tan δ_2	Δ ϕ (degree)	A (dB/m)	t_{plc} (nsec/m)	t_{pcc} (nsec/m)	K_2	tan δ_2	Δ ϕ (degree)	A (dB/m)	t_{plc} (nsec/m)	t_{pcc} (nsec/m)
5.0	0.1	114.1	155.5	7.20	7.08	5.0	0.1	117.5	151.6	7.42	7.31
10.0	0.1	167.8	168.8	10.59	10.48	10.0	0.1	170.2	176.5	10.75	10.61
15.0	0.1	205.0	175.2	12.94	12.84	15.0	0.1	207.5	186.3	13.10	12.97
20.0	0.1	236.2	188.8	14.91	14.79	20.0	0.1	236.2	197.1	14.91	14.77
25.0	0.1	267.3	198.8	16.88	16.75	25.0	0.1	265.0	210.8	16.73	16.58
5.0	0.3	117.3	200.8	7.41	7.11	5.0	0.3	119.8	204.6	7.57	7.26
10.0	0.3	169.2	228.5	10.68	10.37	10.0	0.3	171.8	238.1	10.85	10.50
15.0	0.3	207.8	251.5	13.12	12.79	15.0	0.3	209.5	263.2	13.23	12.85
20.0	0.3	239.6	271.3	15.13	14.77	20.0	0.3	240.2	281.0	15.16	14.77
25.0	0.3	267.5	297.8	16.89	16.48	25.0	0.3	267.1	295.3	16.86	16.46
5.0	0.4	118.5	223.3	7.48	7.06	5.0	0.4	120.8	227.7	7.63	7.20
10.0	0.4	170.6	259.7	10.77	10.32	10.0	0.4	173.0	269.2	10.92	10.43
15.0	0.4	209.4	288.9	13.22	12.73	15.0	0.4	211.0	299.5	13.32	12.79
20.0	0.4	241.4	313.6	15.24	14.72	20.0	0.4	242.1	322.1	15.29	14.73
25.0	0.4	269.1	335.0	16.99	16.43	25.0	0.4	269.4	340.7	17.01	16.42
5.0	0.6	121.4	266.4	7.66	6.98	5.0	0.6	123.5	271.6	7.80	7.09
10.0	0.6	174.3	319.3	11.00	10.23	10.0	0.6	176.4	328.6	11.14	10.31
15.0	0.6	213.7	360.3	13.49	12.63	15.0	0.6	215.3	369.1	13.59	12.69
20.0	0.6	246.3	394.5	15.55	14.61	20.0	0.6	247.3	400.8	15.61	14.64
25.0	0.6	274.5	424.7	17.33	16.33	25.0	0.6	275.1	428.6	17.36	16.34

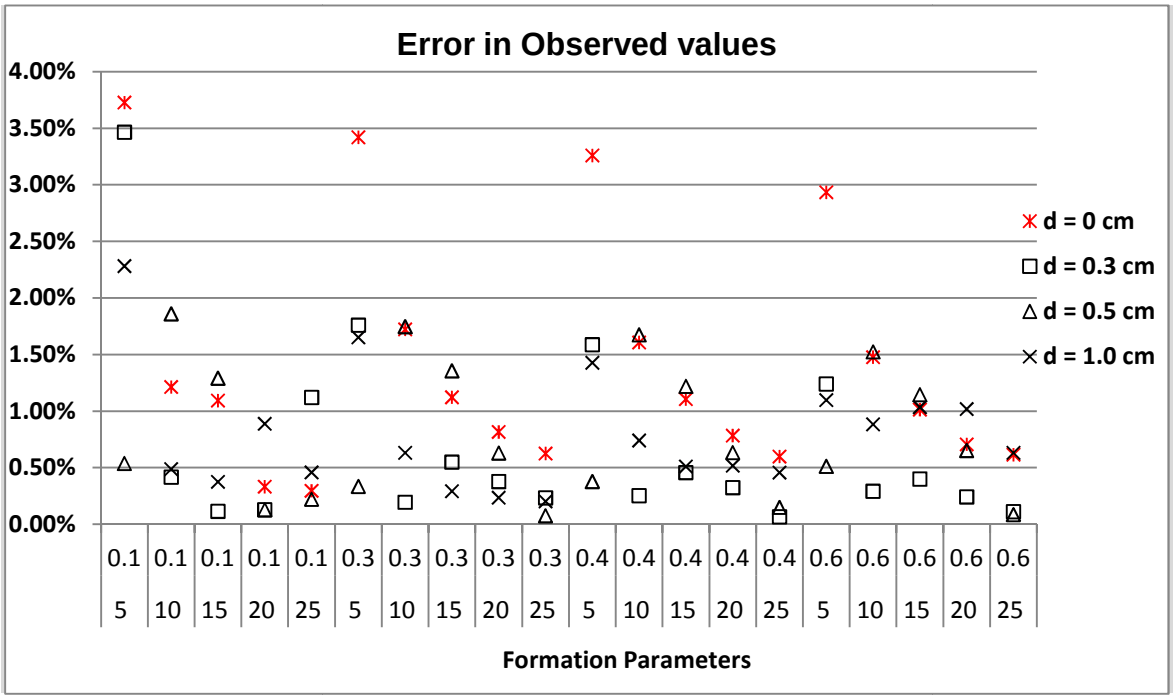

Figure 4.13 Error in t_{plc} for K_1 = 25 and tanδ_1= 1.00

Moreover, for any fixed set of formation and mud cake EM properties, the attenuation $\mathbf{A}$ is a monotonically increasing function of the mud cake thickness. Values of attenuation in excess of 450 dB/m exist for several cases with $\tan\delta_2$ = 0.6. This result is consistent with Schlumberger's field tests of the EPT, which revealed that the measurement of attenuations could approach 500 dB/m for a mud cake thickness of 3/8 inch (1 cm).

4.3. Dielectric Scanner

In this section, the amplitude ratio and phase shift of the dielectric constant both in longitudinal and transverse polarization will be presented. As mentioned previously in the section, the dielectric scanner consists of two transmitting and eight receiving antennas. Each antenna is a cross-dipole offering collocated normal magnetic dipoles shown in Figure 4.14. The blue dipoles define the longitudinal polarization and the red ones, the transverse polarization. The measured results were obtained using our dipole model by rotating the polarization of transmitting and receiving antennas in either longitudinal or transverse direction. In order to study the behaviors of the dielectric scanner, we will analyze the amplitude ratio and the phase shift in a couple of cases: longitudinal transmitter – longitudinal receivers (Hzz), longitudinal transmitter – transverse receivers (Hzx), transverse transmitter – longitudinal receivers (Hxz),

and transverse transmitter – transverse receivers (Hxx), all are measured in homogeneous formation. Also the four different frequencies 1 GHz, 500 MHz, 100 MHz, and 20 MHz will be measured in each case.

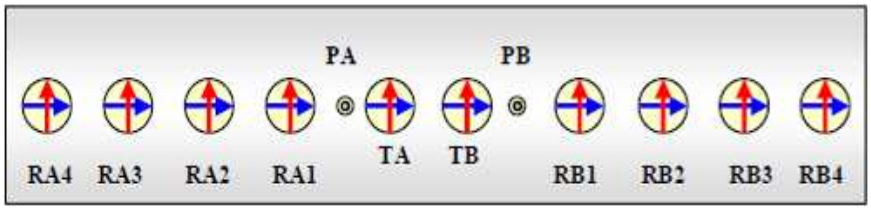

Figure 4.14 Dielectric scanner pad antennas configuration.

4.3.1. LT – LR (Hzz) Polarization

In our infinitesimal dipole model, the longitudinal transmitter – longitudinal receivers will be presented as Hzz, where the first subscript z represents the longitudinal transmitter and the second subscript z represents the longitudinal receiver in that direction. First, Figure 4.15 and 4.16 show the amplitude ratio of RA1 at a frequency of 20 MHz and 1 GHz. In both Figures, for fixed frequency, the amplitude ratios increase as with increasing values of conductivity. As the frequency increased, the amplitude ratio decreased rapidly as increasing values of the dielectric constant.

The phase shift of RA1 at frequency 20 MHz and 1 GHz shown in Figure 4.17 and 4.18. The reason of the phase shift is nearly constant at frequency 20 MHz is

that the wavelength at this frequency is nearly about 15 meters, which seems infinitely long in comparison to the distance between transmitters and receivers.

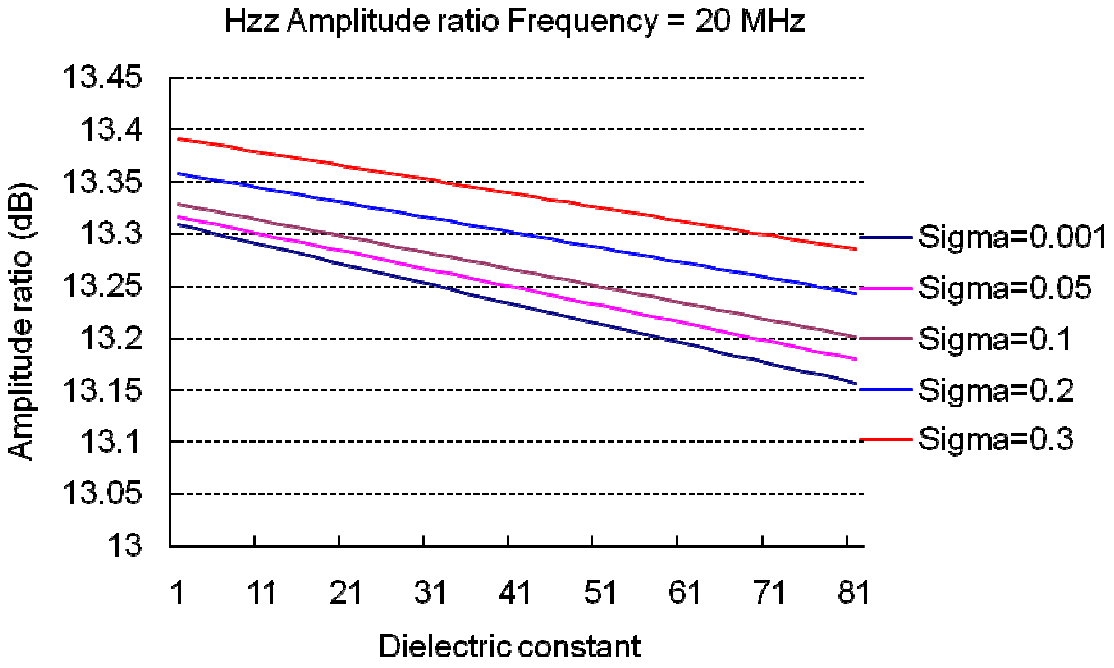

Figure 4.15 The AR of RA1 at f = 20 MHz

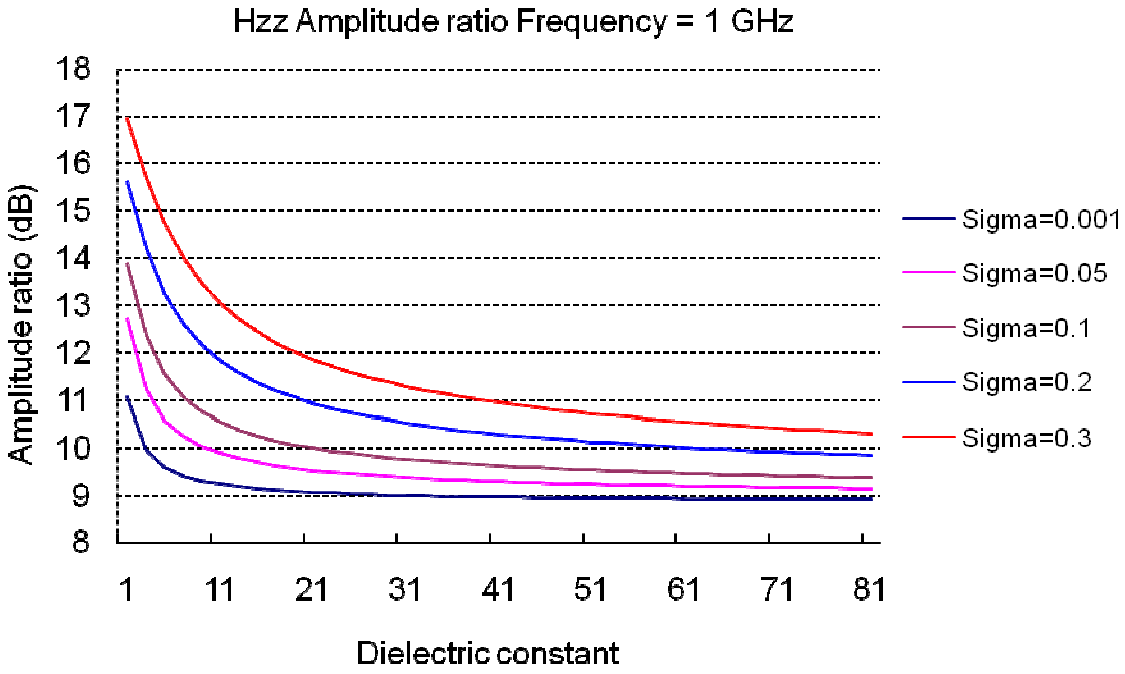

Figure 4.16 The AR of RA1 at f = 1 GHz

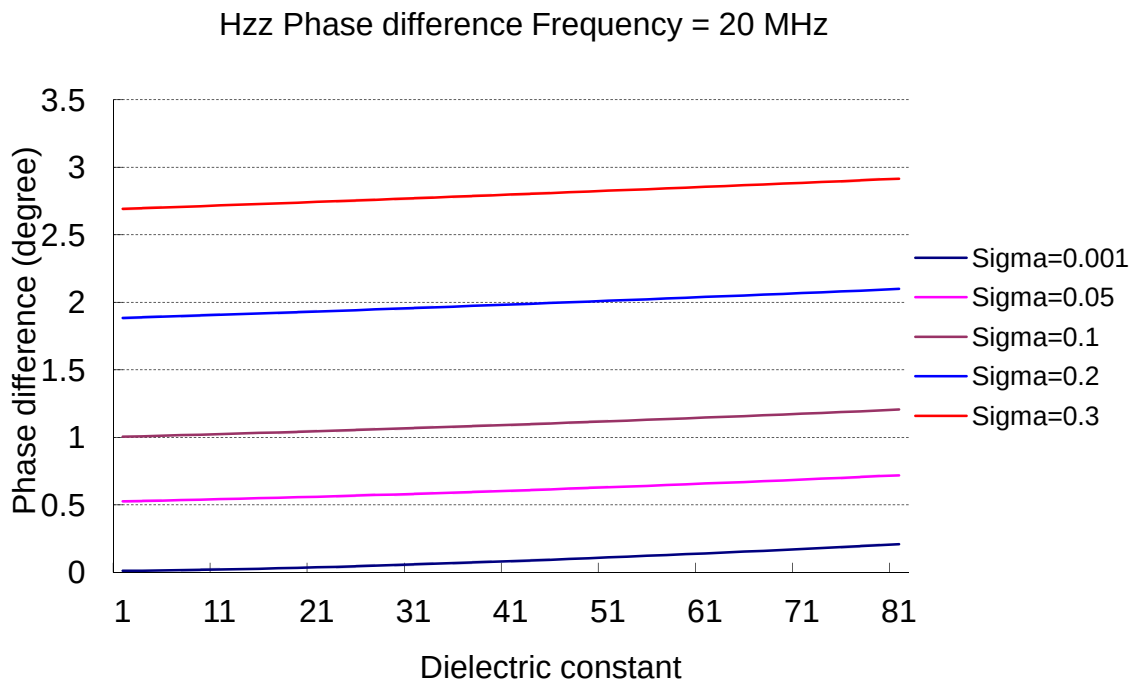

Figure 4.17 The PS of RA1 at f = 20 MHz

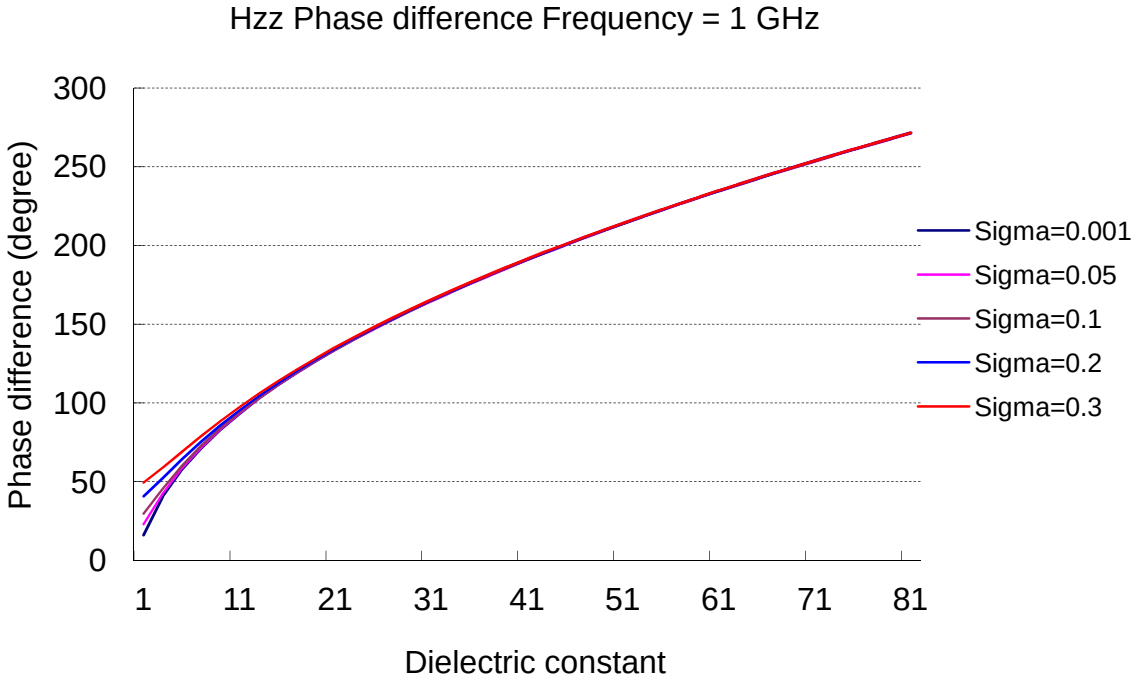

Figure 4.18 The PS of RA1 at f = 1 GHz

As frequency increased, the phase shift increased as well regardless of the change in conductivity. This has been mentioned before as a dielectric constant logging tool that is less dependent on the water salinity.

4.3.2. LT – TR (TT – LR) (Hzx,xz) Polarization

The measurements of the tool responses for the longitudinal transmitter – transverse receivers (Hzx) and transverse transmitter – Longitudinal receivers (Hxz) give the same results. Therefore, we will present the results for both Hzx and Hxz together.

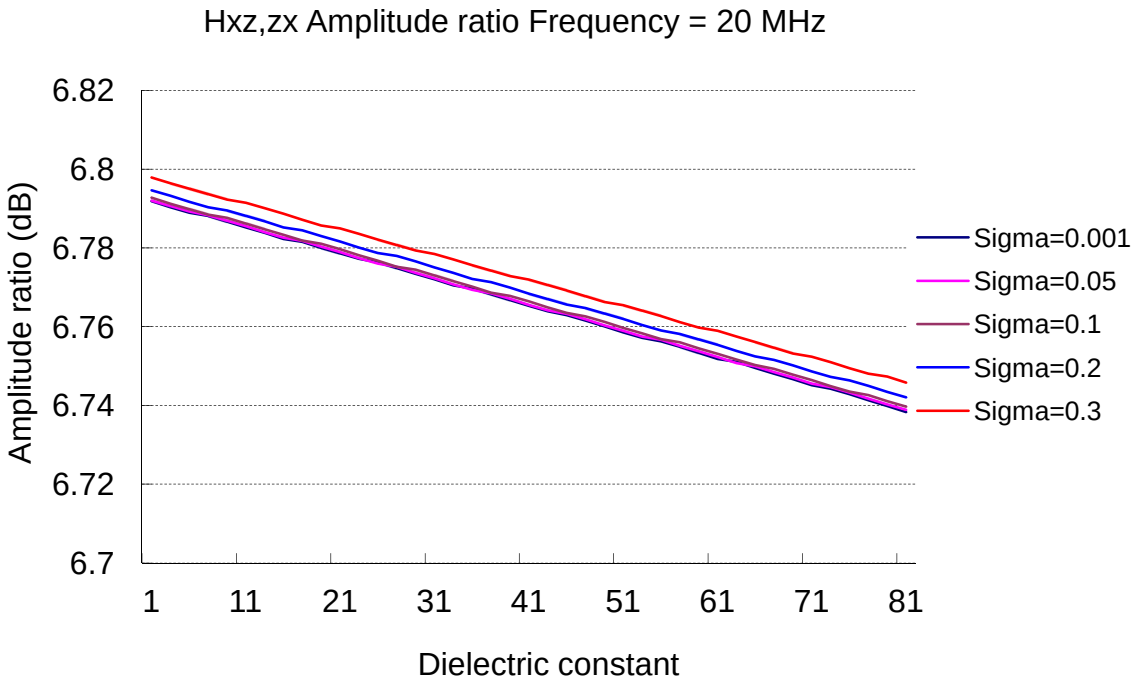

Figure 4.19 The AR of Hxz,zx of RA1 at f = 20 MHz

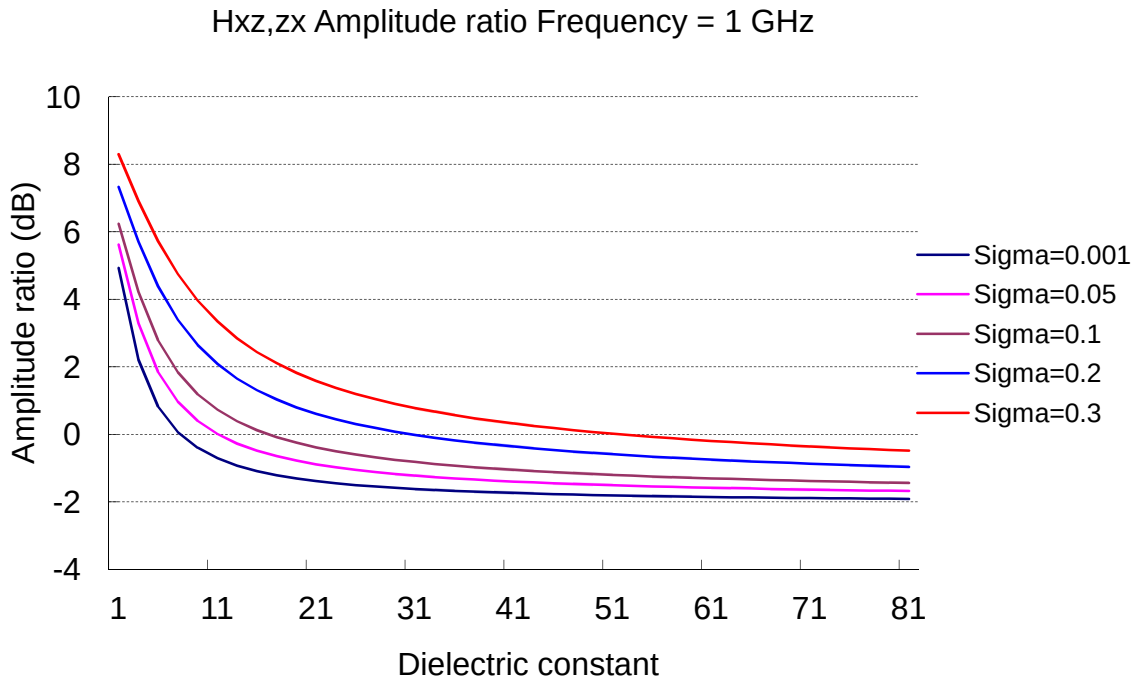

Figure 4.20 The AR of Hxz,zx of RA1 at f = 1 GHz

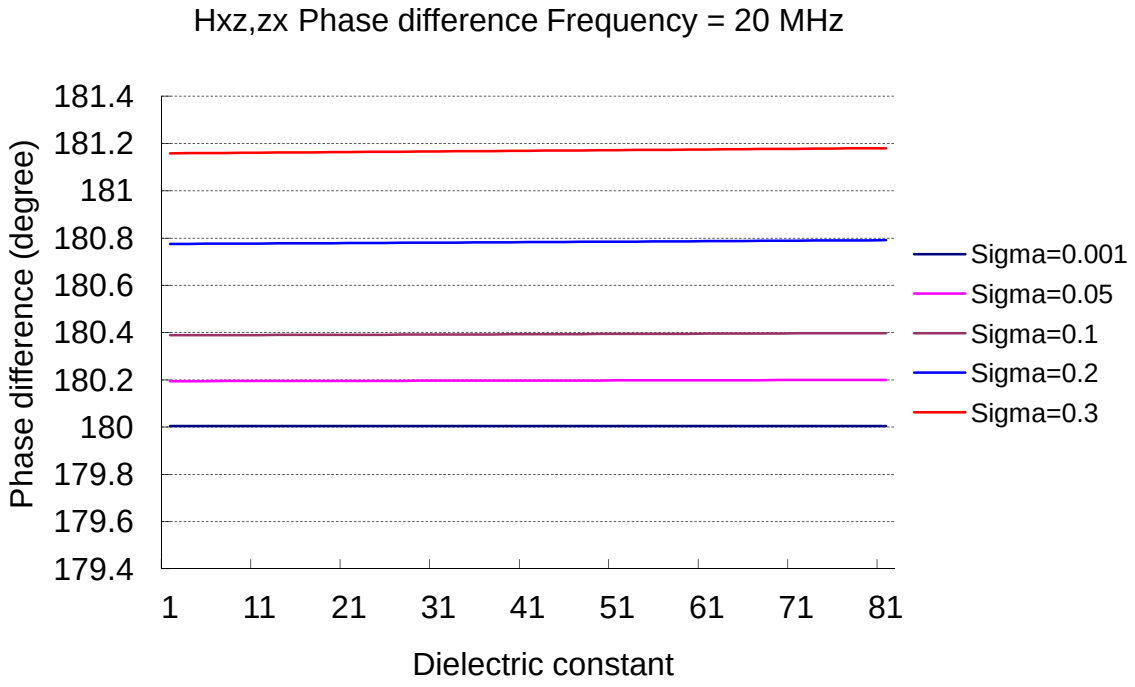

Figure 4.21 The PS of Hxz,zx of RA1 at f = 20 MHz

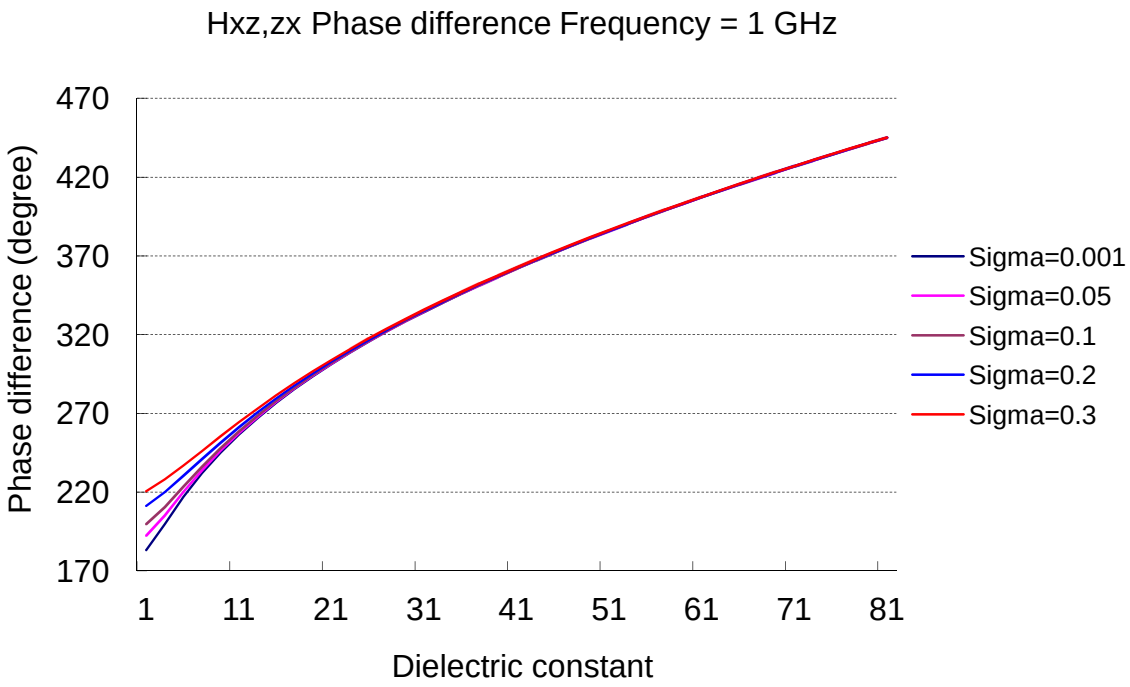

Figure 4.22 The PS of Hxz,zx of RA1 at f = 1 GHz

From Figure 4.19 to 4.22, the amplitude ratios and phase shifts of Hzx,xz reveal the same behaviors as does those represented as Hzz shown in the previous sections. The difference of amplitude ratios between Hzz and Hzx,xz is that the Hzx,xz has lower values of the amplitude ratios than does Hzz. For the phase shift, the Hzx,xz is 180 degrees higher than the Hzz at a given frequency.

4.3.3. TT – TR (Hxx) Polarization

Figures 4.23 to 4.26 represent the amplitude ratios and phase shifts of Hxx of RA1 at a frequency of 20 MHz and 1 GHz. As we can expect, Hxx has the same behaviors as does the other two polarizations in the homogeneous medium.

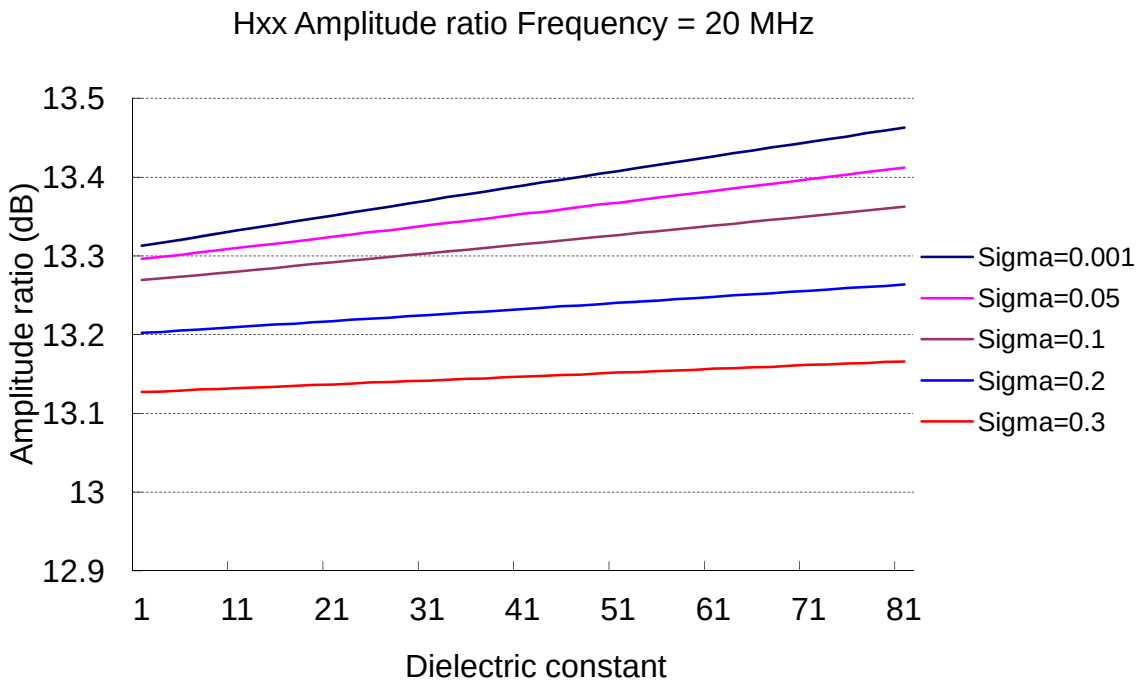

Figure 4.23 The AR of Hxx of RA1 at f = 20 MHz

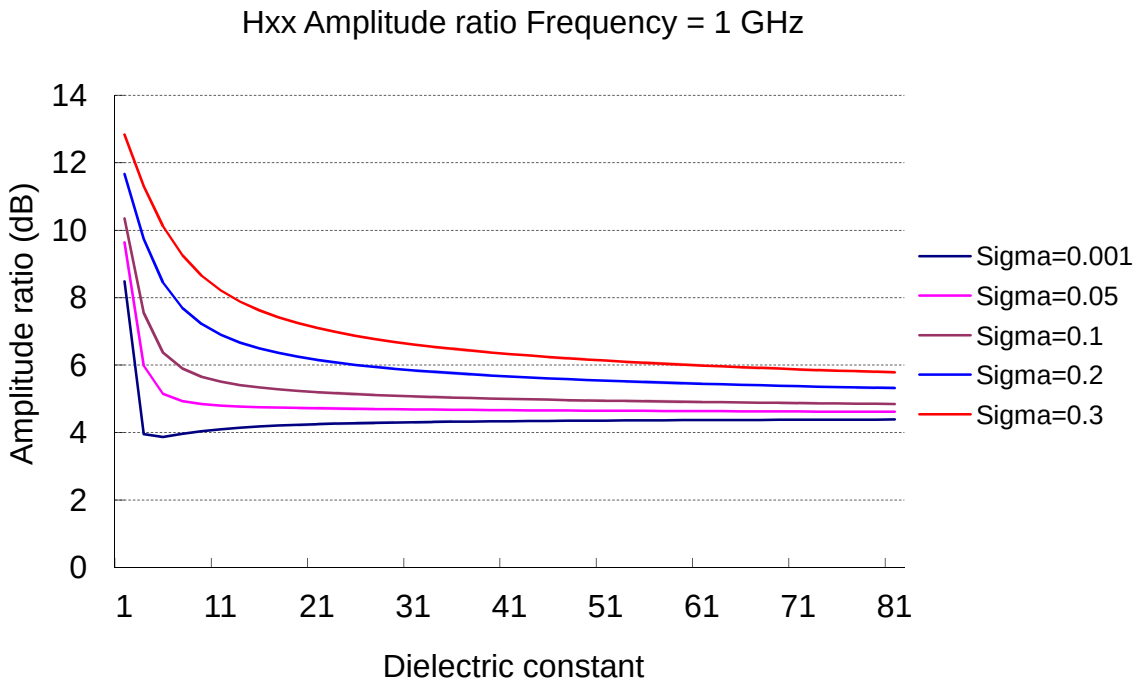

Figure 4.24 The AR of Hxx of RA1 at f = 1 GHz

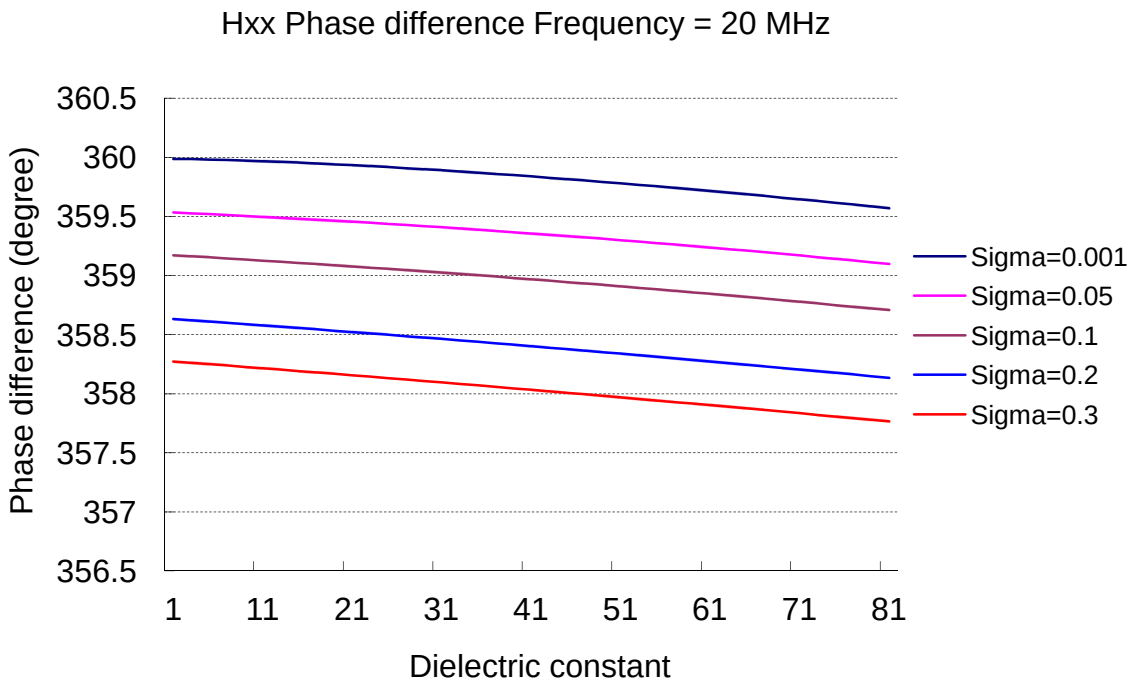

Figure 4.25 The PS of Hxx of RA1 at f = 20 MHz

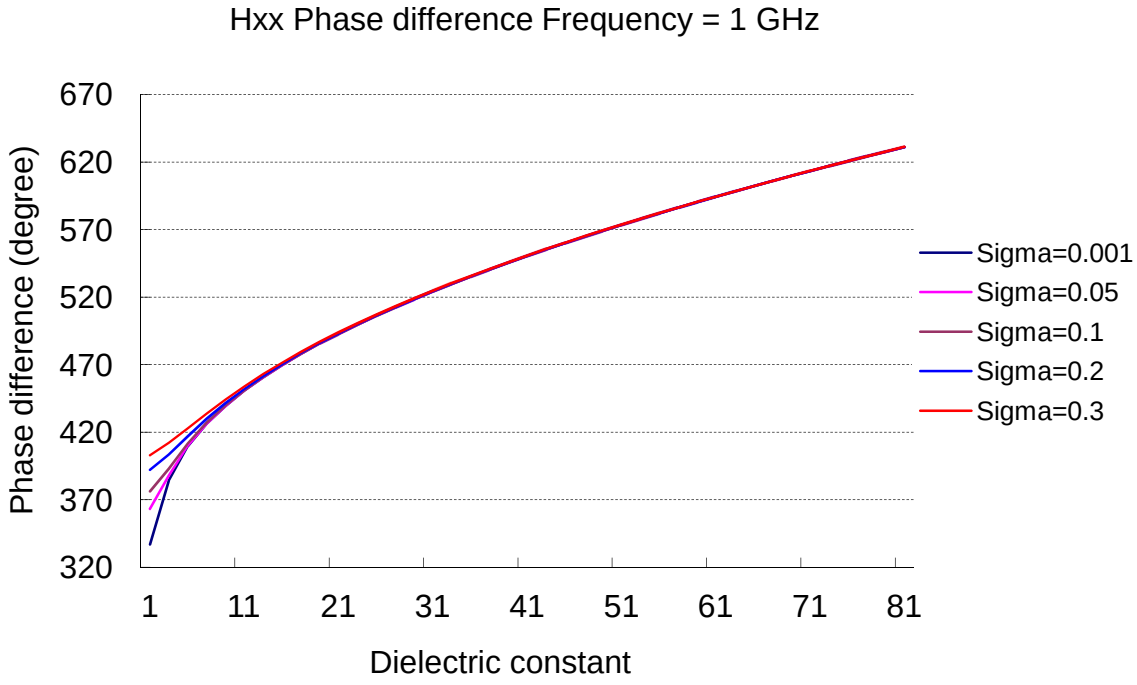

Figure 4.26 The PS of Hxx of RA1 at f = 1 GHz

As shown in Figure 4.25 and 4.26, the phase shifts of Hxx are 180 degrees higher than Hzx,xz shown in Figure 4.23 and 4.24. This concluded that the phase shift of Hxx is 360 degrees above the phase shift in Hzz.

4.3.4. Summary

In the case of the dielectric scanner tool responding in the homogeneous formation that the amplitude ratio increases with increasing values of conductivity, the phase shifts remain the same regardless of the changing of sigma. Due to the symmetrical configuration of antennas, RA1-4 and RB1-4 shown in Figure 4.14, the receiving signals in RA1-4 are the same in RB1-4 in a homogeneous media. Section 4.3.1 to 4.3.3 describes the amplitude ratios and the phase shifts in four different polarizations LT-LR, LT-TR, TT-LR, and TT-TR for RA1. Now we will summarize the behaviors of all four receivers RA1-4.

First, Figure 4.27 and 4.28 show the amplitude ratio of RA1 in all four different polarizations. The Hxz,xz has less values of amplitude ratio among the four directions. This is due to collocated normal receiving dipoles receiving fewer signals from the transmitting dipoles. The amplitude ratios increase with increasing values of sigma. As mentioned, amplitude ratios increase with increasing values of conductivity.

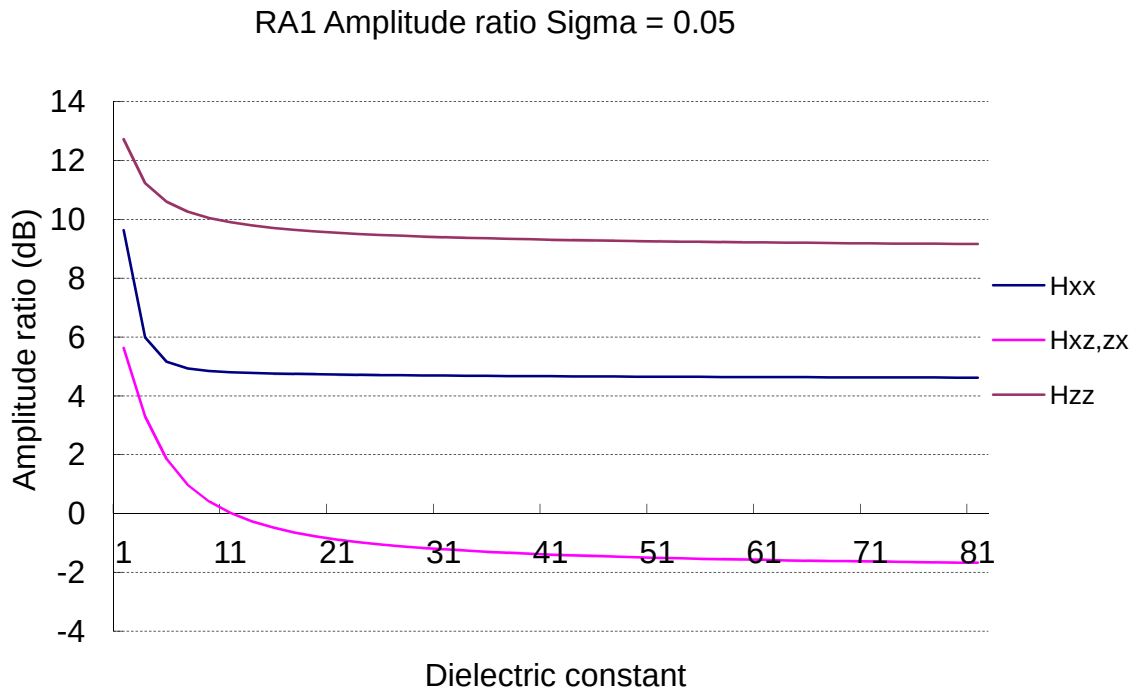

Figure 4.27 The AR of RA1 in sigma = 0.05 and f = 1 GHz

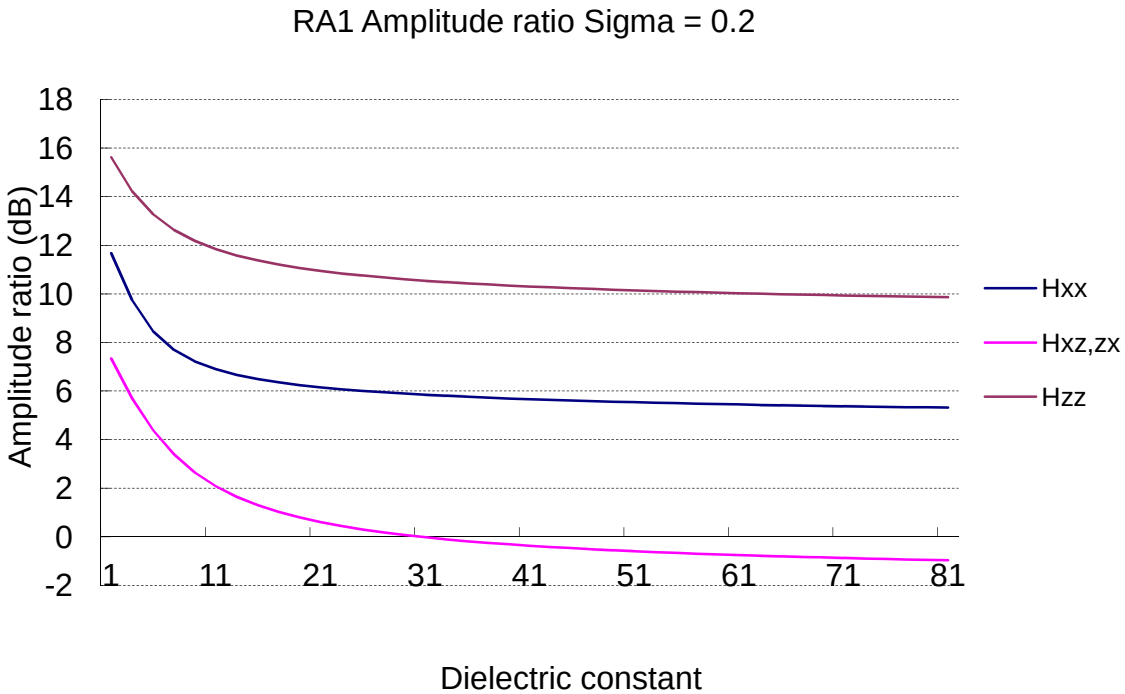

Figure 4.28 The AR of RA1 in sigma = 0.2 and f = 1 GHz

From the previous section, we noted that the phase shifts are 180 degrees higher in Hzx,xz than in Hzz and 180 degrees higher in Hzx,xz than in Hxx. These particular behaviors will be illustrated in the plots listed below. Figure 4.29 and 4.30 show the phase shifts of RA1 in four different polarizations Hxx, Hxz,zx, and Hzz for dielectric constant of 5 and 30 and at frequency of 1 GHz. It is easy to infer that the amplitude ratio in the Hxx polarization is 180 degrees higher than the Hxz,zx polarization, which is180 degrees higher than Hzz. As dielectric constants of media increase, the values of the phase shift increase.

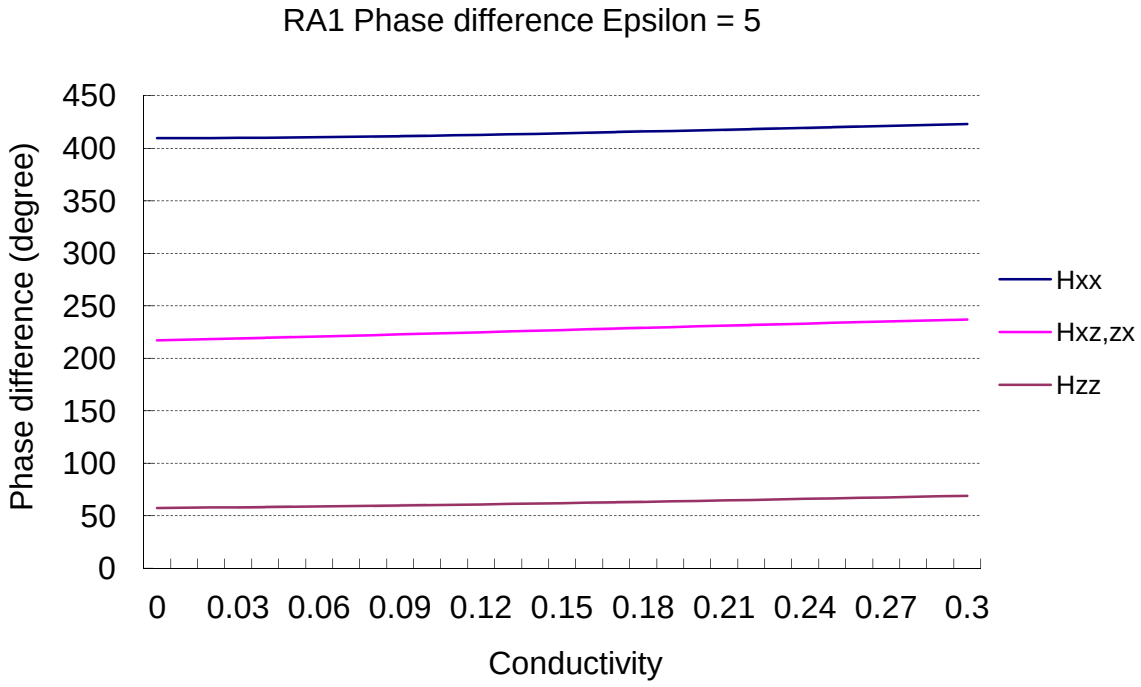

Figure 4.29 The PS of RA1 in epsilon = 5 and f = 1 GHz

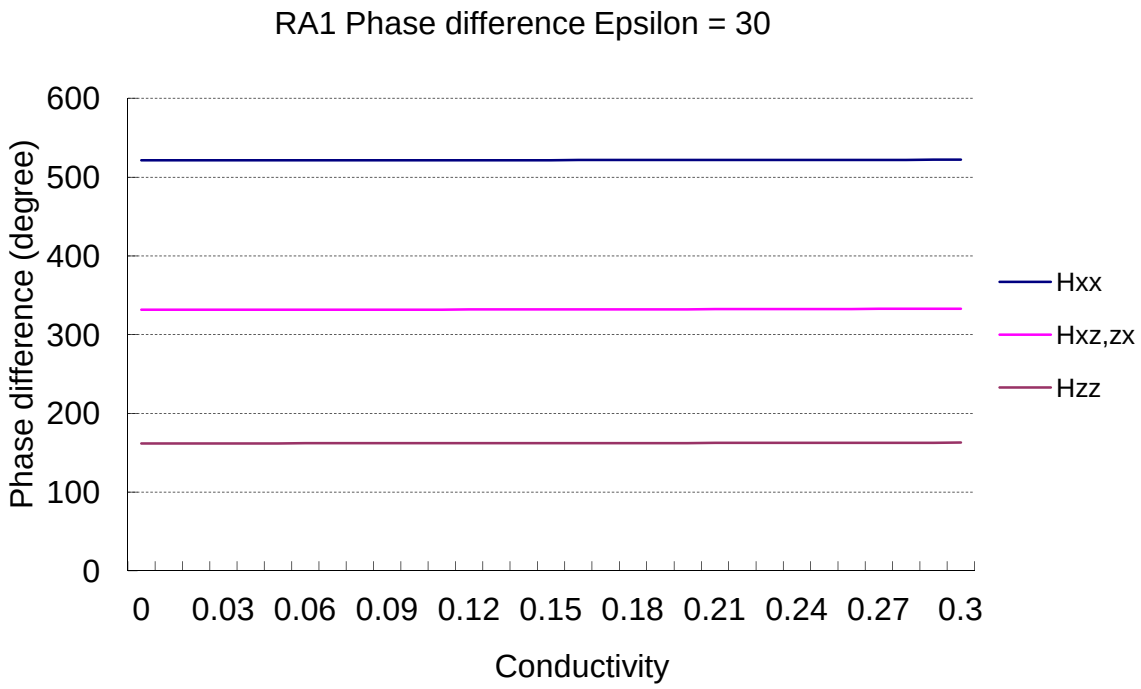

Figure 4.30 The PS of RA1 in epsilon = 30 and f = 1 GHz

The results for those phase differences may also be seen in the Table 4.6, which shows the phase differences of the dielectric scanner for antennas RA1-4 in four different polarizations for the given formation properties. The phase shifts increase slowly as the distance of investigation increases while each polarization is 180 degrees apart. The results were validated for all antennas RA1-4 in different formation properties.

Table 4.6 The PS between Hxx, Hxz,zx, and Hzz at f = 1 GHz

(degree)	Hxx	Hxz,xz	Hzz	(degree)	Hxx	Hxz,xz	Hzz
RA1	417.03	230.31	64.23	RA1	521.45	331.62	162.04
RA2	426.27	240.68	68.20	RA2	524.77	340.38	164.87
RA3	429.01	245.25	69.77	RA3	525.81	343.35	165.85
RA4	430.18	247.56	70.55	RA4	526.28	344.71	166.29
Dielctric constant = 5 Sigma = 0.2				Dielctric constant = 30 Sigma = 0.05			

Chapter 5 Summary and Conclusion

In this thesis, the amplitude ratios and phase shifts of dielectric constant logging tools both in homogeneous and inhomogeneous isotropic formation with different frequencies are presented using the infinitesimal dipole model. Two kinds of high frequency dielectric constant logging tools include the Electromagnetic Propagation Tool (EPT) and the Dielectric Scanner, which have both been studied in this thesis. The purpose of this study is to demonstrate theoretically the feasibility of determining accurate values of the microwave dielectric properties of the earth formation from phase shift and attenuation measurement made in the borehole using the EM wave propagation logging method. The main task of dielectric constant logging tools is to distinguish fresh water from hydrocarbon bearing formation by determining the relative permittivity of the earth formation. This is due to the fact that the dielectric constant of fresh water is relatively high compared with that of hydrocarbons and most minerals. Therefore, the propagation measurement can be used to determine the water-filled porosity independent of water salinity. We find that the infinitesimal dipole model is successful and gives accurate results both in homogeneous and inhomogeneous isotropic formation compared with other models that have been developed in previous studies.

The impedance of an open slot antenna was measured and shown to agree relatively well with that of the experimental study by Long [15] through understanding the admittance of a complementary dipole. The principal area of interest was near the depth correspondent to resonance in the cavity; this was obtained by modeling the cavity size in depth of the quarter guide wavelength $\left(z_0 = \lambda_g / 4\right)$. From the resulting data, we found that the impedance was both a function of the operating frequency as well as the physical parameters of the cavity.

The numerical results suggest that the relative attenuation **A** is proportional to the logarithm of the ratio of the electric field amplitudes at two receivers, decreasing with increasing $\tan\delta_1$ when all other model parameters are held constant. The phase shift, for the range of parameters considered in this study, varied from 100 – 300 degrees. For any fixed values of the mud cake parameters, the phase shifts increased rather rapidly with increasing values of K_2 and increased slowly with the increasing value of $\tan\delta_2$. Moreover, without mud cake present, the relative error in t_{plc} varied from 0.2 to 3.7 percent, and the calculation values of t_{plc} are always less than the true values of t_{pl}.

The dielectric-dispersion measurement of the dielectric scanner provides unique information on rock properties and fluid distribution for advanced petrophysical interpretation through matrix textural determination as well as for

reservoir evaluation and management. Four different polarization cross-dipole measurements introduce better accurate estimations of the formation properties from phase shifts and amplitude ratios.

The dielectric scanner only has a preliminary evaluation in this thesis. In order to continue further improvement of investigation, we will consider how Archie's cementation exponent "m," a critical parameter for accurate saturation determination, may possibly be estimated by measuring the dielectric dispersion.

References

[1] J. Ph. Poley, J. J. Nooteboom and P. J. de Waal, “Use of VHF dielectric measurements for borehole formation analysis,” Log Analyst, vol. 19, no. 3, p. 8–30, 1978.

[2] K. Tam, “Dielectric property measurement of rocks in the VHF-UHF region,” Ph.D. thesis, Texas A&M University, tables 4-6, 1974.

[3] A. R. von Hipple, “Survey in dielectric materials and applications,” Cambridge, M.I.T. Press, p. 365-366, 1954.

[4] T. J. Calvert, “Microwave logging apparatus having dual processing channels,” U.S. patent 3,849,721, Nov. 19, 1974.

[5] R. N. Rau, “Method and apparatus utilizing microwave electromagnetic energy for investigating earth formations,” U.S. patent 3,944,910, Mar. 16, 1976.

[6] R. N. Rau, “Method and apparatus for investigating earth formations utilizing microwave electromagnetic energy,” U.S. patent 4,052,662, Oct. 4, 1977.

[7] R. N. Rau, “Microwave method and apparatus utilizing dielectric loss factor measurements for determination of adsorbed fluid in subsurface formations surrounding a borehole,” U.S. patent 4,077,003, Feb. 28, 1978.

[8] B. Clark, “Electromagnetic logging apparatus using vertical magnetic dipole slot antennas,” U.S. patent 4,704,581, Nov. 3, 1987.

[9] R. Freedman, “Method and apparatus for measuring azimuthal as well as longitudinal waves in a formation traversed by a borehole,” U.S. patent 5,168,234, Dec. 1, 1992.

[10] Asquith, G., and D. Krygowski, “Resistivity Logs,” Resistivity Logs, in G. Asquith and D. Krygowski, Basic Well Log Analysis: AAPG methods in Exploration 16, p. 77-101, 2004.

[11] Von Hipple, “Dielectric Materials and Applications,” A.R. Published jointly by The Technology Press of M.I.T. and John Wiley and Sons Inc., New York, 1954.

[12] W. C. Chew, S. C. Gianzero, “Theoretical investigation of the electromagnetic wave propagation tool,” IEEE Trans. on Geoscience and Remote Sensing, vol. Ge-19, no. 1, p. 1-7, Jan. 1981.

[13] W. C. Chew, “Modeling of the dielectric logging tool at high frequencies: theory,” IEEE Trans. on Geoscience and Remote Sensing, vol. 26, no. 4, p. 382-387, July 1988.

[14] W. C. Chew, “Modeling of the dielectric logging tool at high frequencies: applications and results,” IEEE Trans. on Geoscience and Remote Sensing, vol. 26, no. 4, p. 388-398, July 1988.

[15] S. A. Long, “Experimental study of the impedance of cavity-backed slot antennas,” IEEE Trans. on Antennas and Propagation, vol. AP-23, no. 1, p. 1-7, Jan. 1975.

[16] S. A. Long, “A mathematical model for the impedance of the cavity-backed slot antenna,” IEEE Trans. on Antennas and Propagation, vol. AP-25, no. 6, p. 829-833, Nov. 1977.

[17] J. Mude, S. Arora, T. McDonald, J. Edwards, "Wireline Dielectric Measurements Make a Comeback : Applications in Oman for a New Generation Dielectric Log Measurement," SPWLA 51th Annual Logging Symposium, June 19-23, 2010.

[18] C. A. Balanis, “Antenna Theory Analysis and Design,” Wiley Interscience, 3th edition, p. 133-134, 2005.

[19] C. A. Balanis, “Antenna Theory Analysis and Design,” Wiley Interscience, 3th edition, p. 135-139, 2005.

[20] C. A. Balanis, “Antenna Theory Analysis and Design,” Wiley Interscience, 3th edition, p. 653-659, 2005.

[21] T. J. Calvert, R. N. Rau, and L. E. Wells, “Electromagnetic propagation a new dimension in logging,“ Society of Petroleum Engineers of Aime, p. SPE 6542 1-15., 1977.

[22] S. Ramo, J. R. Whinner, and T. Van Duzer, “Field and Waves in Communication Electronics,” New York: Wiley, p. 422, 1965.

[23] K.A. Safinya, B. Clark, T.M. Habashy, C. Randall, A. Perez-Falcon, “Experimental and Theoretical Study of the Electromagnetic Propagation Tool in Layered and Homogeneous Media,” SPE Formation Evaluation, September 1987.

[24] R. Freedman and John P. Vogiatzis, “Theory of microwave dielectric constant logging using the electromagnetic wave propagation method,” Geophysics, vol. 44, no. 5 (May 1979); p. 969-986, 8 FIGS., 4 Tables.

Appendix A

In this appendix we present numerical results of case 5 - 28 for inhomogeneous isotropic formation with mud cake presented.

Case 5

Mud cake parameters: K_1 = 25, tan δ_1 = 3.00, and d = 0.3 cm

K_2	tan δ_2	$\triangle\varphi$ (degree)	A (dB/m)	t_{plc} (nsec/m)	t_{poc} (nsec/m)
5.0	0.1	112.5	154.7	7.10	6.98
10.0	0.1	166.7	169.3	10.52	10.41
15.0	0.1	205.3	174.5	12.96	12.86
20.0	0.1	236.7	191.5	14.94	14.82
25.0	0.1	269.7	222.0	17.03	16.85
5.0	0.3	115.8	201.3	7.31	7.00
10.0	0.3	168.4	230.4	10.63	10.31
15.0	0.3	208.1	256.5	13.14	12.79
20.0	0.3	240.7	280.5	15.20	14.81
25.0	0.3	268.5	302.8	16.95	16.53
5.0	0.4	116.9	224.1	7.38	6.95
10.0	0.4	169.7	262.4	10.71	10.25
15.0	0.4	209.5	295.3	13.22	12.71
20.0	0.4	242.1	324.3	15.28	14.71
25.0	0.4	270.1	349.7	17.05	16.43
5.0	0.6	119.8	267.5	7.56	6.85
10.0	0.6	173.3	323.5	10.94	10.13
15.0	0.6	213.4	369.0	13.47	12.56
20.0	0.6	246.4	407.6	15.56	14.54
25.0	0.6	274.9	440.5	17.36	16.26

Case 6

Mud cake parameters: K_1 = 25, tan δ_1 = 3.00, and d = 0.5 cm

K_2	tan δ_2	$\triangle\varphi$ (degree)	A (dB/m)	t_{plc} (nsec/m)	t_{poc} (nsec/m)
5.0	0.1	115.8	157.7	7.31	7.18
10.0	0.1	168.7	183.1	10.65	10.50
15.0	0.1	206.8	200.3	13.06	12.89
20.0	0.1	234.9	217.7	14.83	14.64
25.0	0.1	260.6	241.1	16.45	16.22
5.0	0.3	117.6	208.8	7.42	7.08
10.0	0.3	169.6	246.6	10.71	10.32
15.0	0.3	207.3	278.3	13.09	12.64
20.0	0.3	237.4	301.8	14.99	14.51
25.0	0.3	263.3	317.9	16.62	16.12
5.0	0.4	118.5	231.9	7.48	7.01
10.0	0.4	170.5	278.0	10.76	10.22
15.0	0.4	208.3	314.8	13.15	12.53
20.0	0.4	238.9	342.3	15.08	14.41
25.0	0.4	272.1	364.1	17.18	16.49
5.0	0.6	121.0	275.8	7.64	6.88
10.0	0.6	173.3	338.0	10.94	10.03
15.0	0.6	211.7	385.0	13.37	12.33
20.0	0.6	243.4	421.0	15.37	14.25
25.0	0.6	271.4	449.4	17.13	15.96

Case 7

Mud cake parameters: K_1 = 25, tan δ_1 = 3.00, and d = 1 cm

K_2	tan δ_2	$\triangle\varphi$ (degree)	A (dB/m)	t_{plc} (nsec/m)	t_{poc} (nsec/m)
5.0	0.1	114.9	175.7	7.25	7.06
10.0	0.1	165.3	194.6	10.44	10.25
15.0	0.1	202.1	201.8	12.76	12.58
20.0	0.1	231.8	204.5	14.63	14.48
25.0	0.1	259.7	216.3	16.40	16.23
5.0	0.3	116.1	223.1	7.33	6.91
10.0	0.3	166.7	255.7	10.52	10.09
15.0	0.3	204.2	277.7	12.89	12.45
20.0	0.3	235.7	293.0	14.88	14.44
25.0	0.3	263.6	305.3	16.64	16.20
5.0	0.4	117.0	245.6	7.39	6.83
10.0	0.4	167.9	286.2	10.60	10.01
15.0	0.4	205.9	314.2	13.00	12.38
20.0	0.4	237.9	335.2	15.02	14.39
25.0	0.4	266.3	352.4	16.81	16.17
5.0	0.6	119.5	288.7	7.55	6.66
10.0	0.6	171.4	344.7	10.82	9.85
15.0	0.6	210.6	384.7	13.29	12.26
20.0	0.6	243.5	416.4	15.38	14.29
25.0	0.6	272.8	443.6	17.22	16.09

Case 8

Mud cake parameters: K_1 = 25, tan δ_1 = 5.00, and d = 0.3 cm

K_2	tan δ_2	$\triangle\varphi$ (degree)	A (dB/m)	t_{plc} (nsec/m)	t_{poc} (nsec/m)
5.0	0.1	110.8	154.5	6.99	6.87
10.0	0.1	164.9	169.0	10.41	10.29
15.0	0.1	203.7	174.1	12.86	12.75
20.0	0.1	235.4	190.6	14.86	14.74
25.0	0.1	269.0	224.7	16.98	16.80
5.0	0.3	113.9	201.2	7.19	6.88
10.0	0.3	166.5	230.6	10.51	10.19
15.0	0.3	206.5	257.0	13.03	12.68
20.0	0.3	239.4	282.0	15.12	14.72
25.0	0.3	267.7	306.2	16.90	16.46
5.0	0.4	115.0	224.0	7.26	6.83
10.0	0.4	167.8	262.7	10.60	10.13
15.0	0.4	207.8	296.2	13.12	12.59
20.0	0.4	240.8	326.5	15.20	14.61
25.0	0.4	269.0	354.0	16.98	16.34
5.0	0.6	117.8	267.5	7.44	6.72
10.0	0.6	171.4	324.1	10.82	10.00
15.0	0.6	211.6	370.6	13.36	12.43
20.0	0.6	244.8	410.8	15.46	14.41
25.0	0.6	273.4	445.9	17.26	16.12

Case 9

Mud cake parameters: K_1 = 25, tan δ_1 = 5.00, and d = 0.5 cm

K_2	tan δ_2	$\triangle\varphi$ (degree)	A (dB/m)	t_{plc} (nsec/m)	t_{poc} (nsec/m)
5.0	0.1	112.9	160.0	7.13	6.99
10.0	0.1	165.4	181.8	10.44	10.29
15.0	0.1	203.6	196.1	12.85	12.69
20.0	0.1	232.7	212.6	14.69	14.51
25.0	0.1	259.6	238.6	16.39	16.16
5.0	0.3	114.8	209.1	7.25	6.90
10.0	0.3	166.5	244.6	10.51	10.13
15.0	0.3	204.4	274.6	12.91	12.47
20.0	0.3	235.0	298.5	14.84	14.37
25.0	0.3	261.2	316.9	16.49	15.99
5.0	0.4	115.7	231.9	7.31	6.83
10.0	0.4	167.3	264.9	10.56	10.08
15.0	0.4	205.5	311.5	12.97	12.37
20.0	0.4	236.4	339.6	14.93	14.26
25.0	0.4	263.1	361.3	16.61	15.91
5.0	0.6	118.3	275.5	7.47	6.69
10.0	0.6	170.5	335.8	10.76	9.85
15.0	0.6	209.0	382.2	13.20	12.17
20.0	0.6	240.8	418.9	15.20	14.09
25.0	0.6	268.6	448.6	16.96	15.78

Case 10

Mud cake parameters: K_1 = 25, tan δ_1 = 5.00, and d = 1 cm

K_2	tan δ_2	$\triangle\varphi$ (degree)	A (dB/m)	t_{plc} (nsec/m)	t_{poc} (nsec/m)
5.0	0.1	111.7	168.4	7.05	6.88
10.0	0.1	163.3	186.2	10.31	10.14
15.0	0.1	200.9	196.0	12.68	12.53
20.0	0.1	231.2	204.9	14.59	14.44
25.0	0.1	259.5	221.0	16.38	16.20
5.0	0.3	113.3	215.4	7.15	6.76
10.0	0.3	164.5	248.4	10.38	9.98
15.0	0.3	202.7	273.6	12.79	12.36
20.0	0.3	234.4	293.0	14.80	14.35
25.0	0.3	262.1	308.7	16.54	16.08
5.0	0.4	114.2	238.0	7.21	6.69
10.0	0.4	165.6	279.5	10.46	9.89
15.0	0.4	204.1	310.8	12.89	12.28
20.0	0.4	236.2	335.5	14.91	14.27
25.0	0.4	264.3	355.7	16.69	16.02
5.0	0.6	116.8	281.1	7.37	6.53
10.0	0.6	169.0	339.1	10.67	9.73
15.0	0.6	208.3	382.5	13.15	12.12
20.0	0.6	241.3	417.5	15.23	14.13
25.0	0.6	270.3	446.8	17.07	15.91

Case 11

Mud cake parameters: K_1 = 35, tan δ_1 = 1.00, and d = 0.3 cm

K_2	tan δ_2	$\triangle\varphi$ (degree)	A (dB/m)	t_{plc} (nsec/m)	t_{poc} (nsec/m)
5.0	0.1	113.8	156.2	7.18	7.06
10.0	0.1	167.8	169.9	10.60	10.48
15.0	0.1	205.5	174.8	12.97	12.87
20.0	0.1	236.7	190.1	14.94	14.82
25.0	0.1	269.9	205.4	17.04	16.90
5.0	0.3	117.1	202.1	7.40	7.09
10.0	0.3	169.4	229.8	10.70	10.38
15.0	0.3	208.7	253.1	13.17	12.84
20.0	0.3	240.9	273.5	15.21	14.85
25.0	0.3	268.8	291.6	16.97	16.58
5.0	0.4	118.3	224.8	7.47	7.04
10.0	0.4	170.8	261.3	10.78	10.33
15.0	0.4	210.2	291.2	13.27	12.78
20.0	0.4	242.7	316.5	15.32	14.79
25.0	0.4	270.7	338.3	17.09	16.52
5.0	0.6	121.2	268.0	7.65	6.95
10.0	0.6	174.6	321.7	11.02	10.23
15.0	0.6	214.6	363.8	13.55	12.67
20.0	0.6	247.6	398.6	15.63	14.68
25.0	0.6	276.2	428.4	17.44	16.42

Case 12

Mud cake parameters: K_1 = 35, tan δ_1 = 1.00, and d = 0.5 cm

K_2	tan δ_2	$\triangle\varphi$ (degree)	A (dB/m)	t_{plc} (nsec/m)	t_{poc} (nsec/m)
5.0	0.1	118.0	154.1	7.45	7.33
10.0	0.1	171.0	179.9	10.80	10.66
15.0	0.1	209.3	192.4	13.22	13.07
20.0	0.1	237.8	205.7	15.01	14.86
25.0	0.1	266.0	226.6	16.79	16.60
5.0	0.3	119.9	207.7	7.57	7.24
10.0	0.3	172.4	243.7	10.89	10.52
15.0	0.3	210.7	271.9	13.30	12.90
20.0	0.3	241.6	291.9	15.26	14.82
25.0	0.3	268.4	306.5	16.94	16.50
5.0	0.4	120.8	231.0	7.63	7.18
10.0	0.4	173.5	275.3	10.95	10.44
15.0	0.4	212.0	308.9	13.39	12.81
20.0	0.4	243.5	333.3	15.37	14.76
25.0	0.4	270.8	351.6	17.09	16.47
5.0	0.6	123.5	275.4	7.79	7.05
10.0	0.6	176.7	335.9	11.16	10.28
15.0	0.6	216.1	380.0	13.65	12.67
20.0	0.6	248.7	413.0	15.70	14.66
25.0	0.6	277.0	439.2	17.49	16.41

Case 13

Mud cake parameters: K_1 = 35, $\tan\delta_1$ = 1.00, and d = 1 cm

K_2	$\tan\delta_2$	$\triangle\varphi$ (degree)	A (dB/m)	t_{plc} (nsec/m)	t_{poc} (nsec/m)
5.0	0.1	118.7	187.4	7.50	7.26
10.0	0.1	166.1	202.2	10.49	10.27
15.0	0.1	202.6	202.9	12.79	12.61
20.0	0.1	233.2	200.7	14.72	14.57
25.0	0.1	262.0	211.6	16.54	16.38
5.0	0.3	119.7	232.3	7.56	7.09
10.0	0.3	168.0	261.3	10.61	10.15
15.0	0.3	205.4	279.6	12.96	12.51
20.0	0.3	237.7	292.4	15.01	14.57
25.0	0.3	266.4	303.3	16.82	16.39
5.0	0.4	120.6	253.7	7.61	7.01
10.0	0.4	169.3	290.9	10.69	10.07
15.0	0.4	207.3	316.4	13.09	12.46
20.0	0.4	240.2	335.7	15.16	14.53
25.0	0.4	269.3	351.3	17.00	16.37
5.0	0.6	123.0	294.5	7.77	6.86
10.0	0.6	172.9	348.1	10.91	9.93
15.0	0.6	212.2	388.0	13.40	12.35
20.0	0.6	246.4	419.0	15.56	14.47
25.0	0.6	276.6	443.4	17.46	16.35

Case 14

Mud cake parameters: K_1 = 35, $\tan\delta_1$ = 3.00, and d = 0.3 cm

K_2	$\tan\delta_2$	$\triangle\varphi$ (degree)	A (dB/m)	t_{plc} (nsec/m)	t_{poc} (nsec/m)
5.0	0.1	111.5	155.9	7.04	6.91
10.0	0.1	165.6	170.6	10.46	10.34
15.0	0.1	204.4	175.4	12.90	12.80
20.0	0.1	235.9	191.9	14.90	14.77
25.0	0.1	269.6	225.2	17.02	16.84
5.0	0.3	114.6	202.7	7.24	6.92
10.0	0.3	167.3	232.1	10.56	10.24
15.0	0.3	207.3	258.3	13.08	12.73
20.0	0.3	240.2	282.9	15.16	14.77
25.0	0.3	268.4	306.4	16.94	16.50
5.0	0.4	115.8	225.6	7.31	6.87
10.0	0.4	168.6	264.2	10.65	10.17
15.0	0.4	208.6	297.4	13.17	12.64
20.0	0.4	241.5	327.3	15.25	14.66
25.0	0.4	269.8	354.1	17.03	16.39
5.0	0.6	118.6	269.1	7.49	6.76
10.0	0.6	172.2	325.5	10.87	10.04
15.0	0.6	212.5	371.8	13.41	12.48
20.0	0.6	245.7	411.5	15.51	14.47
25.0	0.6	274.3	446.0	17.32	16.18

Case 15

Mud cake parameters: K_1 = 35, $\tan\delta_1$ = 3.00, and d = 0.5 cm

K_2	$\tan\delta_2$	$\triangle\varphi$ (degree)	A (dB/m)	t_{plc} (nsec/m)	t_{poc} (nsec/m)
5.0	0.1	114.2	161.7	7.21	7.06
10.0	0.1	166.6	185.3	10.52	10.36
15.0	0.1	204.6	201.0	12.92	12.75
20.0	0.1	233.2	217.5	14.72	14.53
25.0	0.1	259.5	242.3	16.38	16.15
5.0	0.3	115.9	211.4	7.32	6.96
10.0	0.3	167.5	248.2	10.58	10.18
15.0	0.3	205.3	278.9	12.96	12.51
20.0	0.3	235.6	302.6	14.87	14.39
25.0	0.3	261.6	320.1	16.51	16.00
5.0	0.4	116.8	234.3	7.37	6.89
10.0	0.4	168.5	279.5	10.64	10.08
15.0	0.4	206.3	315.6	13.02	12.39
20.0	0.4	237.0	343.4	14.96	14.28
25.0	0.4	263.6	364.5	16.64	15.93
5.0	0.6	119.3	277.9	7.53	6.74
10.0	0.6	171.4	339.2	10.82	9.89
15.0	0.6	209.8	385.9	13.24	12.19
20.0	0.6	241.4	422.4	15.24	14.10
25.0	0.6	269.2	451.7	17.00	15.80

Case 16

Mud cake parameters: K_1 = 35, $\tan\delta_1$ = 3.00, and d = 1 cm

K_2	$\tan\delta_2$	$\triangle\varphi$ (degree)	A (dB/m)	t_{plc} (nsec/m)	t_{poc} (nsec/m)
5.0	0.1	112.4	172.9	7.10	6.91
10.0	0.1	163.6	190.8	10.33	10.15
15.0	0.1	201.1	199.8	12.70	12.53
20.0	0.1	231.4	206.4	14.61	14.45
25.0	0.1	259.7	220.5	16.39	16.22
5.0	0.3	113.8	219.9	7.19	6.77
10.0	0.3	164.9	252.9	10.41	9.98
15.0	0.3	203.0	277.0	12.82	12.37
20.0	0.3	234.8	295.0	14.82	14.37
25.0	0.3	262.7	309.5	16.58	16.12
5.0	0.4	114.7	242.4	7.24	6.69
10.0	0.4	166.1	283.9	10.48	9.89
15.0	0.4	204.6	314.2	12.92	12.29
20.0	0.4	236.8	337.7	14.95	14.30
25.0	0.4	265.2	356.8	16.74	16.07
5.0	0.6	117.3	285.6	7.40	6.53
10.0	0.6	169.5	343.4	10.70	9.73
15.0	0.6	209.0	385.9	13.19	12.14
20.0	0.6	242.1	419.8	15.29	14.17
25.0	0.6	271.4	448.3	17.13	15.97

Case 17

Mud cake parameters: K_1 = 35, tan δ_1 = 5.00, and d = 0.3 cm

K_2	tan δ_2	$\triangle\varphi$ (degree)	A (dB/m)	t_{plc} (nsec/m)	t_{poc} (nsec/m)
5.0	0.1	109.0	155.6	6.88	6.75
10.0	0.1	162.8	170.1	10.28	10.16
15.0	0.1	201.6	175.7	12.73	12.62
20.0	0.1	233.3	191.6	14.73	14.60
25.0	0.1	267.0	224.5	16.85	16.67
5.0	0.3	111.9	202.3	7.06	6.74
10.0	0.3	164.4	231.9	10.38	10.05
15.0	0.3	204.3	258.3	12.90	12.53
20.0	0.3	237.3	283.2	14.98	14.58
25.0	0.3	265.6	307.5	16.77	16.32
5.0	0.4	113.0	225.0	7.13	6.68
10.0	0.4	165.7	263.9	10.46	9.98
15.0	0.4	205.6	297.4	12.98	12.44
20.0	0.4	238.6	327.8	15.06	14.47
25.0	0.4	266.9	355.6	16.85	16.19
5.0	0.6	115.8	268.5	7.31	6.57
10.0	0.6	169.2	325.2	10.68	9.84
15.0	0.6	209.4	371.8	13.22	12.27
20.0	0.6	242.6	412.3	15.32	14.26
25.0	0.6	271.2	448.0	17.12	15.96

Case 18

Mud cake parameters: K_1 = 35, tan δ_1 = 5.00, and d = 0.5 cm

K_2	tan δ_2	$\triangle\varphi$ (degree)	A (dB/m)	t_{plc} (nsec/m)	t_{poc} (nsec/m)
5.0	0.1	110.2	162.0	6.96	6.81
10.0	0.1	162.4	180.7	10.25	10.10
15.0	0.1	200.4	192.1	12.65	12.50
20.0	0.1	230.2	206.1	14.54	14.37
25.0	0.1	258.5	229.9	16.32	16.12
5.0	0.3	112.1	209.7	7.08	6.72
10.0	0.3	163.6	243.0	10.33	9.94
15.0	0.3	201.8	270.6	12.74	12.32
20.0	0.3	233.0	293.2	14.71	14.25
25.0	0.3	259.7	311.9	16.40	15.92
5.0	0.4	113.1	232.4	7.14	6.65
10.0	0.4	164.7	274.3	10.40	9.86
15.0	0.4	203.0	307.8	12.81	12.22
20.0	0.4	234.4	335.1	14.80	14.16
25.0	0.4	261.6	357.3	16.52	15.84
5.0	0.6	115.7	275.6	7.30	6.50
10.0	0.6	167.9	333.9	10.60	9.69
15.0	0.6	206.8	379.0	13.05	12.04
20.0	0.6	238.9	415.5	15.08	13.98
25.0	0.6	267.0	445.8	16.85	15.69

Case 19

Mud cake parameters: K_1 = 35, tan δ_1 = 5.00, and d = 1 cm

K_2	tan δ_2	$\triangle\varphi$ (degree)	A (dB/m)	t_{plc} (nsec/m)	t_{poc} (nsec/m)
5.0	0.1	109.2	165.9	6.89	6.73
10.0	0.1	161.1	181.7	10.17	10.02
15.0	0.1	199.0	191.1	12.57	12.42
20.0	0.1	229.9	201.6	14.51	14.36
25.0	0.1	259.2	219.0	16.36	16.19
5.0	0.3	110.9	212.3	7.00	6.63
10.0	0.3	162.3	244.0	10.25	9.86
15.0	0.3	200.9	269.3	12.68	12.27
20.0	0.3	232.9	290.0	14.70	14.26
25.0	0.3	260.7	307.7	16.46	16.00
5.0	0.4	111.9	234.8	7.07	6.55
10.0	0.4	163.5	275.3	10.32	9.77
15.0	0.4	202.3	306.9	12.77	12.18
20.0	0.4	234.6	333.0	14.81	14.18
25.0	0.4	262.7	355.0	16.59	15.92
5.0	0.6	114.6	277.9	7.23	6.40
10.0	0.6	166.9	335.1	10.54	9.61
15.0	0.6	206.4	379.2	13.03	12.01
20.0	0.6	239.4	415.5	15.11	14.01
25.0	0.6	268.3	446.6	16.94	15.77

Case 20

Mud cake parameters: K_1 = 40, tan δ_1 = 1.00, and d = 0.3 cm

K_2	tan δ_2	$\triangle\varphi$ (degree)	A (dB/m)	t_{plc} (nsec/m)	t_{poc} (nsec/m)
5.0	0.1	113.6	156.7	7.17	7.04
10.0	0.1	167.8	170.6	10.59	10.47
15.0	0.1	205.6	174.9	12.98	12.87
20.0	0.1	236.9	190.6	14.95	14.83
25.0	0.1	270.8	208.8	17.10	16.95
5.0	0.3	117.0	202.8	7.39	7.08
10.0	0.3	169.4	230.6	10.70	10.38
15.0	0.3	208.9	254.1	13.19	12.85
20.0	0.3	241.3	274.8	15.24	14.87
25.0	0.3	269.4	293.5	17.00	16.61
5.0	0.4	118.2	225.6	7.46	7.03
10.0	0.4	170.8	262.3	10.79	10.33
15.0	0.4	210.5	292.5	13.29	12.79
20.0	0.4	243.1	318.2	15.35	14.81
25.0	0.4	271.3	340.4	17.13	16.55
5.0	0.6	121.1	268.9	7.65	6.94
10.0	0.6	174.6	322.9	11.02	10.22
15.0	0.6	214.8	365.5	13.56	12.67
20.0	0.6	248.0	400.9	15.66	14.69
25.0	0.6	276.8	431.0	17.48	16.44

Case 21

Mud cake parameters: K_1 = 40, tan δ_1 = 1.00, and d = 0.5 cm

K_2	tan δ_2	$\triangle\varphi$ (degree)	A (dB/m)	t_{plc} (nsec/m)	t_{poc} (nsec/m)
5.0	0.1	118.1	155.9	7.45	7.33
10.0	0.1	171.2	182.2	10.81	10.66
15.0	0.1	209.9	196.3	13.25	13.10
20.0	0.1	238.4	210.5	15.05	14.88
25.0	0.1	266.0	233.8	16.79	16.58
5.0	0.3	119.8	209.3	7.56	7.23
10.0	0.3	172.5	246.6	10.89	10.51
15.0	0.3	210.9	276.4	13.31	12.89
20.0	0.3	241.8	297.6	15.27	14.81
25.0	0.3	268.6	312.9	16.96	16.49
5.0	0.4	120.7	232.7	7.62	7.16
10.0	0.4	173.5	278.4	10.95	10.42
15.0	0.4	212.1	313.6	13.39	12.79
20.0	0.4	243.6	339.2	15.38	14.74
25.0	0.4	270.9	358.1	17.11	16.45
5.0	0.6	123.3	277.2	7.79	7.03
10.0	0.6	176.5	339.3	11.14	10.24
15.0	0.6	176.5	339.3	33.87	10.24
20.0	0.6	248.7	419.5	15.70	14.62
25.0	0.6	277.2	446.2	17.50	16.38

Case 22

Mud cake parameters: K_1 = 40, tan δ_1 = 1.00, and d = 1 cm

K_2	tan δ_2	$\triangle\varphi$ (degree)	A (dB/m)	t_{plc} (nsec/m)	t_{poc} (nsec/m)
5.0	0.1	117.9	188.7	7.45	7.21
10.0	0.1	165.9	200.9	10.47	10.26
15.0	0.1	202.4	202.1	12.78	12.61
20.0	0.1	232.9	201.0	14.71	14.56
25.0	0.1	264.5	215.0	16.70	16.54
5.0	0.3	120.7	236.9	7.62	7.13
10.0	0.3	167.8	260.2	10.59	10.14
15.0	0.3	205.0	278.5	12.94	12.49
20.0	0.3	237.1	292.5	14.97	14.53
25.0	0.3	265.8	304.8	16.78	16.34
5.0	0.4	120.2	255.3	7.59	6.97
10.0	0.4	169.2	289.6	10.68	10.07
15.0	0.4	206.8	315.1	13.06	12.44
20.0	0.4	239.4	335.8	15.11	14.48
25.0	0.4	268.5	353.1	16.95	16.31
5.0	0.6	122.9	296.2	7.76	6.83
10.0	0.6	172.8	346.3	10.91	9.94
15.0	0.6	211.5	386.0	13.35	12.31
20.0	0.6	245.2	419.3	15.48	14.38
25.0	0.6	275.5	446.7	17.39	16.26

Case 23

Mud cake parameters: K_1 = 40, tan δ_1 = 3.00, and d = 0.3 cm

K_2	tan δ_2	$\triangle\varphi$ (degree)	A (dB/m)	t_{plc} (nsec/m)	t_{poc} (nsec/m)
5.0	0.1	110.9	156.5	7.00	6.87
10.0	0.1	165.0	171.3	10.42	10.30
15.0	0.1	203.9	176.2	12.87	12.76
20.0	0.1	235.5	192.6	14.87	14.74
25.0	0.1	269.2	226.5	17.00	16.81
5.0	0.3	114.0	203.5	7.20	6.88
10.0	0.3	166.7	232.9	10.53	10.20
15.0	0.3	206.7	259.3	13.05	12.69
20.0	0.3	239.7	284.1	15.13	14.73
25.0	0.3	268.0	308.0	16.92	16.47
5.0	0.4	115.2	226.3	7.27	6.82
10.0	0.4	168.1	265.0	10.61	10.13
15.0	0.4	208.0	298.5	13.13	12.60
20.0	0.4	241.0	328.6	15.22	14.62
25.0	0.4	269.3	355.8	17.00	16.35
5.0	0.6	118.0	269.8	7.45	6.71
10.0	0.6	171.6	326.4	10.83	10.00
15.0	0.6	211.9	372.9	13.38	12.43
20.0	0.6	245.1	413.1	15.48	14.42
25.0	0.6	273.8	448.0	17.28	16.13

Case 24

Mud cake parameters: K_1 = 40, tan δ_1 = 3.00, and d = 0.5 cm

K_2	tan δ_2	$\triangle\varphi$ (degree)	A (dB/m)	t_{plc} (nsec/m)	t_{poc} (nsec/m)
5.0	0.1	113.3	163.3	7.15	7.00
10.0	0.1	165.5	185.7	10.45	10.29
15.0	0.1	203.4	200.4	12.84	12.67
20.0	0.1	232.2	216.0	14.66	14.47
25.0	0.1	259.0	240.4	16.35	16.12
5.0	0.3	115.0	212.4	7.26	6.90
10.0	0.3	166.5	248.4	10.51	10.11
15.0	0.3	204.2	278.2	12.89	12.44
20.0	0.3	234.7	301.5	14.82	14.33
25.0	0.3	260.9	319.2	16.47	15.96
5.0	0.4	115.9	235.2	7.32	6.82
10.0	0.4	167.5	279.6	10.57	10.01
15.0	0.4	205.3	314.9	12.96	12.33
20.0	0.4	236.1	342.5	14.91	14.23
25.0	0.4	262.9	363.7	16.60	15.89
5.0	0.6	118.5	278.6	7.48	6.67
10.0	0.6	170.5	339.1	10.76	9.83
15.0	0.6	208.9	385.3	13.19	12.14
20.0	0.6	240.6	421.6	15.19	14.05
25.0	0.6	268.4	451.2	16.95	15.75

Case 25

Mud cake parameters: K_1 = 40, $\tan\delta_1$ = 3.00, and d = 1 cm

K_2	$\tan\delta_2$	$\triangle\varphi$ (degree)	A (dB/m)	t_{plc} (nsec/m)	t_{poc} (nsec/m)
5.0	0.1	111.5	171.8	7.04	6.85
10.0	0.1	162.8	189.0	10.28	10.11
15.0	0.1	200.5	198.3	12.66	12.49
20.0	0.1	231.0	206.2	14.59	14.42
25.0	0.1	259.6	221.2	16.39	16.21
5.0	0.3	113.0	218.5	7.13	6.73
10.0	0.3	164.1	251.3	10.36	9.94
15.0	0.3	202.4	275.9	12.78	12.33
20.0	0.3	234.3	294.9	14.79	14.33
25.0	0.3	262.2	310.5	16.55	16.08
5.0	0.4	113.9	241.0	7.19	6.65
10.0	0.4	165.3	282.3	10.43	9.85
15.0	0.4	203.9	313.3	12.87	12.25
20.0	0.4	236.1	337.7	14.91	14.26
25.0	0.4	264.5	357.8	16.70	16.02
5.0	0.6	116.5	284.0	7.35	6.48
10.0	0.6	168.6	341.9	10.65	9.68
15.0	0.6	208.1	385.3	13.14	12.09
20.0	0.6	241.3	420.2	15.23	14.11
25.0	0.6	270.6	449.6	17.08	15.91

Case 26

Mud cake parameters: K_1 = 40, $\tan\delta_1$ = 5.00, and d = 0.3 cm

K_2	$\tan\delta_2$	$\triangle\varphi$ (degree)	A (dB/m)	t_{plc} (nsec/m)	t_{poc} (nsec/m)
5.0	0.1	108.0	156.0	6.82	6.69
10.0	0.1	161.7	170.4	10.21	10.09
15.0	0.1	200.5	176.4	12.66	12.55
20.0	0.1	232.2	192.1	14.66	14.53
25.0	0.1	265.7	223.9	16.77	16.59
5.0	0.3	110.8	202.6	7.00	6.67
10.0	0.3	163.3	232.3	10.31	9.97
15.0	0.3	203.1	258.7	12.82	12.45
20.0	0.3	236.1	283.4	14.90	14.50
25.0	0.3	264.4	307.5	16.69	16.24
5.0	0.4	111.9	225.3	7.07	6.61
10.0	0.4	164.6	264.3	10.39	9.91
15.0	0.4	204.4	297.7	12.91	12.37
20.0	0.4	237.4	327.9	14.99	14.39
25.0	0.4	265.7	355.6	16.77	16.11
5.0	0.6	114.8	268.7	7.25	6.49
10.0	0.6	168.1	325.5	10.61	9.76
15.0	0.6	208.3	372.0	13.15	12.19
20.0	0.6	241.4	412.4	15.24	14.17
25.0	0.6	270.0	448.0	17.04	15.88

Case 27

Mud cake parameters: K_1 = 40, $\tan\delta_1$ = 5.00, and d = 0.5 cm

K_2	$\tan\delta_2$	$\triangle\varphi$ (degree)	A (dB/m)	t_{plc} (nsec/m)	t_{poc} (nsec/m)
5.0	0.1	108.9	162.4	6.88	6.72
10.0	0.1	161.0	179.8	10.16	10.02
15.0	0.1	199.0	190.3	12.56	12.41
20.0	0.1	229.2	203.3	14.47	14.31
25.0	0.1	258.0	225.8	16.29	16.09
5.0	0.3	110.8	209.5	7.00	6.63
10.0	0.3	162.2	242.0	10.24	9.86
15.0	0.3	200.5	268.7	12.66	12.25
20.0	0.3	232.0	290.8	14.65	14.20
25.0	0.3	259.1	309.5	16.35	15.88
5.0	0.4	111.8	232.1	7.06	6.56
10.0	0.4	163.4	273.2	10.31	9.78
15.0	0.4	201.8	306.0	12.74	12.15
20.0	0.4	233.5	333.0	14.74	14.11
25.0	0.4	260.9	355.4	16.47	15.80
5.0	0.6	114.4	275.2	7.22	6.42
10.0	0.6	166.7	332.9	10.52	9.61
15.0	0.6	205.7	377.5	12.99	11.98
20.0	0.6	238.1	413.9	15.03	13.93
25.0	0.6	266.3	444.5	16.81	15.65

Case 28

Mud cake parameters: K_1 = 40, $\tan\delta_1$ = 5.00, and d = 1 cm

K_2	$\tan\delta_2$	$\triangle\varphi$ (degree)	A (dB/m)	t_{plc} (nsec/m)	t_{poc} (nsec/m)
5.0	0.1	108.0	165.1	6.82	6.66
10.0	0.1	160.1	180.1	10.10	9.95
15.0	0.1	198.1	189.2	12.50	12.36
20.0	0.1	229.1	200.0	14.47	14.32
25.0	0.1	258.8	217.4	16.34	16.17
5.0	0.3	109.9	211.2	6.94	6.56
10.0	0.3	161.3	242.4	10.18	9.80
15.0	0.3	200.0	267.5	12.62	12.21
20.0	0.3	232.1	288.4	14.65	14.22
25.0	0.3	260.0	306.6	16.42	15.96
5.0	0.4	110.9	233.7	7.00	6.49
10.0	0.4	162.5	273.7	10.26	9.72
15.0	0.4	201.4	305.3	12.72	12.13
20.0	0.4	233.8	331.6	14.76	14.13
25.0	0.4	262.0	354.0	16.54	15.88
5.0	0.6	113.5	276.7	7.17	6.34
10.0	0.6	166.0	333.6	10.48	9.56
15.0	0.6	205.5	377.7	12.97	11.96
20.0	0.6	238.5	414.3	15.06	13.96
25.0	0.6	267.5	445.7	16.89	15.72